Incorporating Advanced Surface and Subsurface Processes in Mesoscale Climate Models

by

Jason Davison

A thesis
presented to the University of Waterloo
in fulfillment of the
thesis requirement for the degree of
Doctor of Philosophy
in
Earth Sciences

Waterloo, Ontario, Canada, 2016

Abstract

Regional anthropogenic climate change poses significant risks to the security of water resources for communities throughout the world. Current climate simulations seek to predict the risks to water resources by employing land surface models (LSMs). While LSMs incorporate biogeophysics, heat, albedo, surface water, and shallow subsurface water, they do not include lateral surface/subsurface flow, groundwater storage, or critical feedbacks between surface and subsurface hydrology. Consequently, the shortfalls of current models severely limit our abilities to predict and understand risks to water resources.

Therefore, this study investigates the development of coupling HydroGeoSphere (HGS), an advanced 3D control-volume finite element surface and variably-saturated subsurface model, to two separate atmospheric models to capture the interactions between the deep subsurface, surface, and atmosphere. Initially, HGS was coupled to a simple 0D atmospheric boundary layer (ABL) model, hereafter referred to as the HGS-ABL model. The coupled HGS-ABL model physically resolves boundary layer dynamics, precipitation, evapotranspiration, energy balance, surface water, and groundwater flow. The experimental simulations showed that current LSMs are too shallow for handling deep root-zones and do not provide an adequate representation of subsurface heat storage. Furthermore, the HGS-ABL simulations showed a positive correlation between the soil moisture and the energy feedbacks.

To transition from a 0D to a 3D atmosphere, this study then coupled HGS to the Weather Research and Forecasting (WRF) Model, a 3-dimensonal mesoscale nonhydrostatic atmospheric model, hereafter referred to as the HGS-WRF model. HGS replaces the land surface components of WRF by providing the actual evapotranspiration (AET) and soil saturation from the porous media to the atmosphere. In exchange, WRF provides HGS with the potential evapotranspiration (PET) and precipitation fluxes. The flexible coupling technique uniquely accepts independent model meshing and projections and links domains based on their geographic coordinates (i.e., latitude and longitude).

The newly coupled HGS-WRF model was then implemented over the entire California Basin. This 3D California Basin Model is 14-layers thick with over 400,000 nodes. The geological model was based on the STATSGO2 soil data, USGS HYDRO1K topographic data, and USGS water use data. Initially, the HGS model was spun-up with historic precipitation and PET data (provided by CMIP5). Once the model reached steady state, groundwater pumping was turned on, and the HGS model was run to present-day conditions. The HGS California Basin Model simulated similar drawdown rates to the Gravity Recovery and Climate Experiment (GRACE), a 21st century remote sensing satellite. Finally, the HGS-WRF model simulated the California Basin for a 200 day period and successfully replicated the Klamath river, Sacramento river, precipitation, and evapotranspiration fluxes.

Acknowledgements

I first must thank my two advisors Dr. Edward A. Sudicky and Dr. John C. Lin. Working under your guidance has truly been an honor. I will always value all of the time and resources that both of you have spent helping me build my career as a researcher and scientist. I also would like to thank my PhD committee members Dr. David L. Rudolph and Dr. Young-Jin Park. Dave, it has been an absolute pleasure to learn the ins and outs of teaching physical hydrogeology under your leadership. Young-Jin, thank you for your words of wisdom, humor, daily advice, and friendship.

I would like to especially thank my primary research group at Aquanty including Steven Berg, Steven Frey, Killian Miller, and Michael Callaghan. I deeply appreciate Hyoun-Tae Hwang for helping me learn HGS and FORTRAN, collaborating with me on all of my research projects, and for being a truly good friend. I am extremely thankful for my atmospheric research groups at the University of Waterloo and University of Utah, including Kristina Luus, Joshua Benmergui, Mostafa Kamal, Myung-Gwan Kim, Lacey Holland, and Logan Mitchell. I am very thankful for the help that Derek Mallia provided creating the WRF simulations. I also must thank all of my friends at the University of Waterloo, including Cameron Toy, Cassia Johnson, Cailin Hillier, Will Lotosky, Jen Hansen, Ulanna Wityk, and Lori Labelle. Each of you mean so much to me and have made my time at Waterloo so enjoyable.

Most importantly I would like to thank my family. Thank you Mom and Dad; the amount of support that you have provided me is unquantifiable. To Jacqueline Lopour, from the late nights to the numerous edits, corrections and rereads that you endured, I

can't express how much I appreciate you. Thank you Jacque.

Finally, I would like to thank the financial support from the University of Waterloo and from the Canadian government. My research would not have been possible without the gracious funds from Dr. John C. Lin's Ontario Early Researcher Award and Dr. Edward A. Sudicky's Discovery Grant from the Natural Sciences and Engineering Research Council of Canada (NSERC). I also appreciate the support provided by the Canada Research Chair held by Edward A. Sudicky.

Table of Contents

List of Tables ix

List of Figures x

1 Introduction 1

1.1 Thesis Organization . . . 4
1.2 Contributions to Science . . . 6
1.3 Definition of Variables . . . 7

2 HydroGeoSphere Atmospheric Boundary Layer Model 11

2.1 Integrated Hydrologic-Climate Model . . . 12
2.1.1 Land Surface Scheme . . . 13
2.1.2 Atmospheric Boundary Layer . . . 18
2.1.3 Model Coupling . . . 21
2.2 HGS-ABL Pseudocode . . . 23
2.3 Noah LSM Comparison . . . 25
2.4 Illustrative Example . . . 28
2.5 Subsurface Temperature . . . 35
2.6 Root Zone Depth . . . 40
2.6.1 Water-Level Fluctuation . . . 45

3 HydroGeoSphere Weather Research and Forecasting Model 48
3.1 HydroGeoSphere . . . 49
3.2 Weather Research and Forecasting . . . 51
3.3 Coupling Method . . . 52
3.3.1 Spatial Coupling . . . 52
3.3.2 Temporal Coupling . . . 56
3.4 Parallelization . . . 59
3.5 Advantages over previous models . . . 61
3.6 Example Simulation . . . 63

4 California Model 64
4.1 Introduction . . . 65
4.1.1 Previous California Models . . . 66
4.2 California Basin Model . . . 70
4.2.1 Geological Model . . . 70
4.2.2 Boundary Conditions . . . 73
4.3 Atmospheric Model . . . 85
4.4 Results . . . 87
4.4.1 Model Spin-up . . . 87
4.4.2 Coupled Simulation . . . 93

5 Conclusion 124
5.1 Future Work . . . 127

References 129

List of Tables

1.1 Global variables. 8
1.2 Variables used in the HGS model. 9
1.3 Variables used in the atmospheric models. 10

2.1 White analysis of fluctuating head data for Well #1, at 20 days. 47
2.2 White analysis of fluctuating head data for Well #2, at 20 days. 47

4.1 Albers Projection for HGS model. 78
4.2 Soil texture hydraulic properties with van Genuchten parameters. 79
4.3 California 2010 water use by county (*U.S. Geological Survey*, 2015a). . . . 80
4.4 California 2010 water use by county (*U.S. Geological Survey*, 2015a). . . . 81
4.5 California 2010 water use by county (*U.S. Geological Survey*, 2015a). . . . 82
4.6 California Basin 10 day averaged volumetric fluxes. 98
4.7 California Basin Mean Absolute Error. 114

List of Figures

2.1 Coupled atmosphere, surface and subsurface conceptual model. The dark lines show a 3-D finite element mesh for the surface/subsurface discretization. The 0-D atmospheric domain is represented as a single averaged element above the surface. 14

2.2 Coupling flow chart. HydroGeoSphere represents the surface/subsurface component while the ABL Model with a sub-time loop handles the atmospheric domain. 15

2.3 HGS-ABL model's pseudocode for a single time step. 24

2.4 Noah LSM comparison: Surface temperature, sensible heat flux, latent heat flux, and net energy flux for a 10 day comparison of the HGS model (solid red line) to the Noah LSM (dash black line). 27

2.5 Illustrative Example: Vertical section showing the discretization for the V-catchment domain, which is 1 km long and 10 m wide. The domain ranges between 8 m and 10 m in thickness. 31

2.6 Illustrative Example: Hydraulic head response for Wells #1 to #5. 32

2.7 Iluustrative Example: Daily averaged latent and sensible heat fluxes for the coupled model system. 33

2.8 Illustrative Example: Daily averaged atmospheric and land surface temperatures for the 100 day HGS-ABL simulation. 34

2.9 Subsurface Temperature: The 2.0 m case shown on top and 8.0 m case shown on bottom, both at 100 days. 37

2.10 Subsurface Temperature: The 25, 50, 75, and 100 day subsurface temperature profile for the 2.0 m model (shown in red) and 8.0 m model (shown in black) at x = 500 m. 38

2.11 Subsurface Temperature: Comparison of the daily averaged atmospheric and land surface temperatures for the 2.0 m (shown in red) and 8.0 m models (shown in black). . . . 39

2.12 Effect of Root-Zone Depth: Initial subsurface saturations in the model domain. 41

2.13 Effect of Root-Zone Depth on latent and sensible heat fluxes, atmospheric temperature, and land surface temperature. . . . 42

2.14 Effect of Root-Zone Depth on hydraulic head for well #1. . . . 43

2.15 Effect of Root-Zone Depth on hydraulic head for well #2. . . . 44

3.1 Coupled linking between the HGS and WRF models. . . . 53

3.2 HGS-WRF coupling schematic. HGS passes the saturation and actual evapotranspiration to WRF. WRF passes the precipitation and potential evapotranspiration fluxes to HGS. . . . 58

3.3 Modified HGS-WRF model coupling. WRF outputs net precipitation to HGS and HGS outputs saturation to WRF. . . . 60

4.1 The California Basin Characterization Model (CA-BCM) schematic of water processes (*Flint et al.*, 2013). . . . 68

4.2 Previous physics-based California models (*Faunt*, 2009; *Bolger et al.*, 2011; *Gilbert and Maxwell*, 2014). . . . 69

4.3 USGS Hydrologic Unit Code (HUC) map for the United States. The California Basin region 18 is shown in red. Figure modified from *Long* (2016). . 72

4.4 Topographic relief map for the California Basin Model. . . . 74

4.5 Three-dimensional California geological model. . . . 75

4.6 California Basin Model 4 km resolution discretization. . . . 76

4.7 California 30 year average (1980-2010) precipitation data shown in meters per year. . . . 83

4.8 California 30 year average (1980-2010) potential evapotranspiration data shown in meters per year. . . . 84

4.9 The WRF domain is the entire rectangular box, inside of the atmospheric model the land surface is prescribed by HGS for the California Basin and the Noah LSM for the rest of the domain. . . . 86

4.10 The California Basin offline simulation plotting depth to groundwater table for 1915. 89

4.11 The California Basin offline simulation plotting depth to groundwater table for 1965. 90

4.12 The California Basin offline simulation plotting depth to groundwater table for 2015. 91

4.13 A comparison of simulated groundwater loss per year with estimated GRACE groundwater loss over the entire California Basin. 92

4.14 HGS-WRF simulation for the first 0.6 days. 94

4.15 HGS-WRF simulation for day 0.9 to 1.5. 95

4.16 HGS-WRF California Basin mass balance for the 200-day simulation . . . 99

4.17 HGS-WRF California Basin mass balance for the 200-day simulation . . . 100

4.18 HGS-WRF California Basin cumulative mass balance for the 200-day simulation 101

4.19 Coupled HGS-WRF simulation displaying averaged log depth, precipitation, evapotranspiration, and change in saturation for 1 to 20 days (January 1 to January 20). 104

4.20 Coupled HGS-WRF simulation displaying averaged log depth, precipitation, evapotranspiration, and change in saturation for 21 to 40 days (January 21 to February 9). 105

4.21 Coupled HGS-WRF simulation displaying averaged log depth, precipitation, evapotranspiration, and change in saturation for 41 to 60 days (February 10 to March 1). 106

4.22 Coupled HGS-WRF simulation displaying averaged log depth, precipitation, evapotranspiration, and change in saturation for 61 to 80 days (March 2 to March 21). 107

4.23 Coupled HGS-WRF simulation displaying averaged log depth, precipitation, evapotranspiration, and change in saturation for 81 to 100 days (March 22 to April 10). 108

4.24 Coupled HGS-WRF simulation displaying averaged log depth, precipitation, evapotranspiration, and change in saturation for 101 to 120 days (April 11 to April 30). 109

4.25 Coupled HGS-WRF simulation displaying averaged log depth, precipitation, evapotranspiration, and change in saturation for 121 to 141 days (May 1 to May 20). 110

4.26 Coupled HGS-WRF simulation displaying averaged log depth, precipitation, evapotranspiration, and change in saturation for 141 to 160 days (May 21 to June 9). 111

4.27 Coupled HGS-WRF simulation displaying averaged log depth, precipitation, evapotranspiration, and change in saturation for 161 to 180 days (June 10 to June 29). 112

4.28 Coupled HGS-WRF simulation displaying averaged log depth, precipitation, evapotranspiration, and change in saturation for 181 to 200 days (June 30 to July 20). 113

4.29 20-day mean precipitation for three MET stations in the California Basin. 116

4.30 20-day mean evapotranspiration for three MET stations in the California Basin. 117

4.31 Simulated vs. Observed precipitation for three MET stations in the California Basin. 118

4.32 Simulated vs. Observed evapotranspiration for three MET stations in the California Basin. 119

4.33 Sacrameto river gauging station comparison between observed and simulated data for USGS 11447650 SACRAMENTO R A FREEPORT CA 122

4.34 Klamath river gauging station comparison between observed and simulated data for USGS 11530500 KLAMATH R NR KLAMATH CA. 123

Chapter 1

Introduction

Regional climate change will pose significant risks to the security of water resources that support human activities throughout the world (*Bartholomeus et al.*, 2011; *Karl et al.*, 1995; *Easterling et al.*, 2000; *Kundzewicz et al.*, 2007; *Sebestyen et al.*, 2009; *Skoulikaris and Ganoulis*, 2011). Projected global warming will cause an increase in evapotranspiration and a decrease in available water in arid climates (*Oki and Kanae*, 2006). For example, streamflow in the Colorado River Basin may decrease by up to 35% from just a 2.5°C temperature increase (*Vano et al.*, 2014). Human activities already have played a negative role on water resources, as seen in California's Central Valley's unsustainable loss of water storage, which loses 31 mm of stored water per year (*Famiglietti et al.*, 2011). *Scanlon et al.* (2012) predict that under current pumping conditions, the water reserves of the Central Valley will last for only another 370 years while portions of the High Plains aquifer may only have enough water for an additional 81 years.

Climate simulations seek to predict these current and future risks to water resources by employing land surface models (LSMs). The first generation of LSMs were elementary bucket models that approximated the subsurface as a single soil layer (*Manabe et al.*, 1965; *Noilhan and Planton*, 1989). As models grew in sophistication with the availability of computer power, land surface modelers employed 1-D vertical soil columns based on vadose-zone hydrology, biogeophysics, and heat transport; the most prominent of these is the Noah LSM (*McCumber and Pielke*, 1981; *Gusev and Nasonova*, 1998; *Mengelkamp et al.*, 1999; *Chen and Dudhia*, 2001).

The Noah LSM was originally developed by Oregon State University as a two layer soil model for calculations of the sensible and latent heat fluxes. It was later extended by the National Center for Atmospheric Research (NCAR) as a robust 1-D land surface scheme with vertical unsaturated flow, heat transport, and evapotranspiration solved by the moisture based Richards' Equation, diffusion equation, and the Penman Equation. Although the Noah LSM was an advancement over previous land surface models, it lacks horizontal subsurface flow processes and assumes that the soil column remains unsaturated and never reaches a fully-saturated case at any of the node layers. Once water exceeds saturation, the Noah LSM removes the excess water as runoff, interflow, or drainage (*Chen and Dudhia*, 2001). While these assumptions may be reasonable for deep groundwater tables, the Noah LSM will underestimate soil moisture under heavy rain events or shallow groundwater tables.

Due to the limitations of the Noah LSM, NCAR advanced their first generation model to include horizontal two dimensional groundwater flow. This second generation model, named Noah Distributed, adds in many hydraulic features that were commonly seen in hydrologic models, including surface water flow and subsurface percolation (*Gochis et al.*, 2013). The interflow between columns is achieved utilizing the steady-state Dupuit-Forchheimer approximation, an analytical equation describing horizontal 1-D flow in an unconfined aquifer (*Gochis and Chen*, 2003; *Gochis et al.*, 2013). The Dupuit-Forchheimer assumption breaks down when groundwater tables are steep - e.g., near pumping wells or around mountainous topography.

Only recently has ParFlow, a finite difference 3-D groundwater and 2-D surface water model, been incorporated into Weather Research and Forecasting (WRF) Model, a 3-D mesoscale atmospheric model, replacing the hydrologic portion of the Noah LSM (*Maxwell et al.*, 2011). ParFlow strengthens land surface modeling by implementing physics-based hydrology equations; however, it relies on the 1-D Noah LSM for land surface energy and moisture balance. Similarly, CATHY, a 3-D variably saturated subsurface model with surface water routing, was coupled to the Noah-MP (Noah LSM with multi-physics options) (*Niu et al.*, 2014). There are benefits of continuing to adopt the Noah LSM for the near surface, including a large user base familiar with the model, its low numerical cost, and its well-established soil/vegetation data sets. However, evapotranspiration processes are only solved in the near surface, usually the top two meters, by the 1-D Noah LSM (*Maxwell et al.*, 2011). Even though the work achieved by coupling an integrated hydrologic model to the Noah LSM was a drastic improvement for land surface schemes, the current generation of coupled models are still constrained to the 1-D LSM framework.

In order to extend LSMs beyond the 1-D formation, this study will demonstrate a novel method of applying an integrated surface/subsurface flow, heat and solute transport model, HydroGeoSphere (HGS) (*Aquanty, Inc.*, 2015; *Therrien and Sudicky*, 1996), as a third generation land surface model coupled to atmospheric models. The method discussed in this work is currently the most complete LSM approach because of the incorporation of 2-D surface and 3-D subsurface water flow with evapotranspiration processes into one global domain, rather than the previous methods of relying on two separate hydrology and land surface models.

1.1 Thesis Organization

This thesis is organized into 5 chapters and the contents are shown below.

Chapter 2 describes the coupling of HGS to a simple 0D atmospheric boundary layer

(ABL) model. The coupled model physically resolves boundary layer dynamics, precipitation, evapotranspiration, surface energy balance, surface water, and groundwater flow. Chapter 2 was published in the December 2015 issue of Advances in Water Resources and titled *Coupled atmospheric, land surface, and subsurface modeling: Exploring water and energy feedbacks in three-dimensions* (*Davison et al.*, 2015).

Chapter 3 explains the iterative coupling of Weather Research and Forecasting (WRF), a 3-dimensonal mesoscale nonhydrostatic atmospheric model, to HydroGeoSphere. The 3D HGS model replaces the land surface components of WRF by providing the actual evapotranspiration and soil saturation from the porous media to the atmosphere. In exchange, WRF provides HGS with the potential evapotranspiration and precipitation fluxes.

Chapter 4 discusses the development of the HGS California Basin Model. Initially, the HGS model was spun-up with historic precipitation and PET data (provided by CMIP5). Once the model reached steady state, groundwater pumping was turned on, and the HGS model run to present-day conditions. Finally, this chapter implements the HGS-WRF model over California.

Chapter 5 analyses the results from coupling HGS to atmospheric models, and discusses the future and limitations of coupled models.

1.2 Contributions to Science

The interactions between the subsurface, surface, and atmosphere are poorly understood. Currently, there are only a few tools that incorporate the physics of all three domains into one numerical package. These previous coupled numerical models have significant limitations, including a shallow groundwater assumption, maximum vegetation root depths of 2 meters (due to the Noah LSM formulation), and coarse model resolutions to match atmospheric domains.

These above problems are solved by first coupling the HydroGeoSphere (HGS) model to a simple 0D Atmospheric Boundary Layer (ABL) model. This straightforward model, referred to as the HGS-ABL model, highlighted the importance of moving land surface models from a 1-D to a 3-D framework that implicitly includes groundwater, surface water, and evapotranspiration processes into a single global domain. It is shown that the subsurface–specifically groundwater flow–critically alters the atmosphere. It is also demonstrated that deeper roots buffer the atmosphere during drought conditions by maintaining higher evapotranspiration rates than shallow roots.

By understanding the fundamental interactions between the subsurface, surface, and atmosphere from the HGS-ABL model, HGS was coupled to the three-dimensional Weather Research and Forecasting (WRF) Model. The HGS-WRF model is currently the most complete water resource model available today, because the deep subsurface, surface, and atmosphere are included into one simulation. The HGS-WRF model was then applied to the California Basin for a 200 day simulation period. To the best of my knowledge, the coupled model simulation of the California Basin is the first of its kind to:

- Include deep groundwater flow within a coupled subsurface, surface, and atmospheric model.
- Include root depths that extend past the 2 meter near surface.
- Implement different spatial and temporal resolutions for the coupled atmospheric and hydrological models.
- Create the first three-dimensional geological model for the entire California Basin.
- Simulate a fully-integrated surface and subsurface model for the California Basin.
- Simulate the largest application of a coupled three-dimensional subsurface, surface, and atmospheric model.

1.3 Definition of Variables

Throughout this thesis we implement several variables and constants that appear in empirical and partial differential equations. The following three tables (Tables 1.1, 1.2, and 1.3) define the variables used within this thesis.

Table 1.1: Global variables.

Variable	Name	Dimension
t	Time	T
T	Temperature	Θ
ρ_w	Density of water	ML^{-3}
c_w	Specific heat of water	$\mathrm{L}^2\mathrm{T}^{-2}\ \Theta^{-1}$
G	Ground heat flux	MT^{-3}
PET	Potential evapotranspiration	LT^{-1}
ET	Actual evapotranspiration	LT^{-1}
i	Precipitation	LT^{-1}
A	Overlapping elemental area	L^2
wrf_i	WRF index	(-)
hgs_j	HGS index	(-)

Table 1.2: Variables used in the HGS model.

Variable	Name	Dimension
θ_s	Saturated water content	(-)
S_w	Water saturation	(-)
Γ_{ex}	Volumetric fluid exchange between domains	$\mathrm{L}^3\mathrm{L}^{-3}\mathrm{T}^{-1}$
Q	Volumetric exchange outside the domain	$\mathrm{L}^3\mathrm{L}^{-3}\mathrm{T}^{-1}$
$\mathbf{q}$	Darcy flux	LT^{-1}
$\mathbf{K}$	Hydraulic conductivity	LT^{-1}
ψ	Pressure head	L
z	Elevation head	L
k_r	Relative permeability	(-)
S_s	Specific storage	L^{-1}
K_{ox}, K_{oy}	Manning equation conductances	LT^{-1}
ϕ_o	Surface domain porosity	(-)
h_o	Water surface elevation	L
d_o	Depth of surface water	L
n_x, n_y	Manning roughness coefficients	$\mathrm{TL}^{-1/3}$
s	Direction of the maximum surface slope	L
k_b	Thermal conductivity of soil	L
D	Thermal diffusivity	$\mathrm{L}^2\mathrm{T}^{-1}$
Q_T	Thermal source or sink	$\mathrm{M}^2\mathrm{L}^{-1}\mathrm{T}^{-3}$
Ω_0	Thermal interaction between the surface/subsurface	$\mathrm{M}^2\mathrm{L}^{-1}\mathrm{T}^{-3}$
ρ_b	Density of soil	ML^{-3}
c_b	Specific heat of soil	$\mathrm{L}^2\mathrm{T}^{-2}\ \Theta^{-1}$
E_{can}	Canopy evaporation rate	LT^{-1}
T_p	Transpiration rate	LT^{-1}
E_s	Evaporation rate	LT^{-1}
f_1, f_2, α^*	Fitting functions	(-)
RDF	Root density function	(-)
EDF	Energy density function	(-)

Table 1.3: Variables used in the atmospheric models.

Variable	Name	Dimension
$\mathrm{R}_{\mathrm{net}}$	Net Energy Flux	$\mathrm{ML}^{-1}\mathrm{T}^{-3}$
α	Albedo	(-)
SW_{dn}	Shortwave solar radiation flux	$\mathrm{ML}^{-1}\mathrm{T}^{-3}$
T_a	Atmospheric temperature	Θ
ϵ_a	Atmospheric emissivity	(-)
ϵ_s	Surface emissivity	(-)
σ	Stefan-Boltzmann constant	$\mathrm{MT}^{-3}\Theta^{-4}$
LE	Latent heat flux	MT^{-3}
H	Sensible heat flux	MT^{-3}
ρ_a	Density of air	ML^{-3}
c_p	Specific heat of air	$\mathrm{L}^{2}\mathrm{T}^{-2}\ \Theta^{-1}$
G_a	Atmospheric conductance	LT^{-1}
q_f	Specific humidity in free atmosphere	(-)
q_a	Specific humidity in the ABL	(-)
E	Surface moisture flux	$\mathrm{MT}^{-1}\mathrm{L}^{-2}$
W	ABL subsidence rate	LT^{-1}
h_a	Height of the ABL	L
r_a	Atmospheric resistance	TL^{-1}
r_v	Vegetative resistance	TL^{-1}
q^*	Saturation specific humidity	(-)
RH	Relative humidity	(-)
f_{100}	Cloud cover at 100% RH	(-)
RH_e	e-folding relative humidity	(-)

Chapter 2

HydroGeoSphere
Atmospheric Boundary Layer Model

2.1 Integrated Hydrologic-Climate Model

Advanced earth system modeling requires a comprehensive understanding of the major physical processes in the environment, including atmospheric dynamics, precipitation, evapotranspiration, surface energy balance, surface water, and variably-saturated subsurface flow. The goal is to combine the above phenomena into one numerical model, referred to as HydroGeoSphere-Atmospheric Boundary Layered model (HGS-ABL), conceptually shown in Figure 2.1, that incorporates the surface, subsurface and simple atmospheric dynamics. HGS, a 3-D control-volume finite element surface/subsurface model, handles the bottom portion of the domain whereas the ABL model, a single 0-D element atmospheric code, addresses the top portion.

Between the two coupled models, a direct spatially-weighted grid-averaging scheme manages the energy and water interactions. The HGS-ABL model implements an explicit sub-time stepping scheme allowing the atmospheric domain to perform multiple smaller time steps for every larger and more expensive time step that HGS performs. The time looping procedure, shown in Figure 2.2, illustrates the principal components between the two models. The ABL model calculates the time-dependent values for potential evapotranspiration, atmospheric temperature, ground heat flux, and precipitation. In contrast, HGS supplies the atmosphere with the actual evapotranspiration (ET) and ground level temperature.

A simple 0-D ABL model was chosen as a starting point because it minimizes the number of independent variables, which simplifies the analysis of the various interactions between the atmosphere, surface, and subsurface domains. The HGS-ABL model is only forced by solar radiation, and it does not require any additional input parameters. The model has an additional benefit in that it can be readily used for probabilistic simulations for future climate changes.

Using the coupled model, the results of a simplified vertical column test case are compared with the 1-D Noah-LSM. After the comparison, it is demonstrated that the depth of the water table plays a pivotal role in determining the temperature and energy balance. The importance of modeling an adequately thick domain for extended simulations is also discussed. Finally, this chapter investigates the atmospheric buffering capacity during drought conditions for a broad range of root-zone depths.

2.1.1 Land Surface Scheme

HGS, originally developed (for subsurface flow) by *Therrien and Sudicky* (1996), is a three-dimensional control-volume finite element model. HGS is a physically-based model with global implicit coupling of the surface and subsurface domains using the common node or dual-node approach. HGS' surface domain solves two-dimensional surface flow and water storage by utilizing the diffusion-wave equation, while the subsurface implements the Richards' equation for three-dimensional flow. Solute and energy transport processes are solved in both domains with the advection-dispersion equation (*Graf and Therrien*, 2007). *Brookfield et al.* (2009) successfully verified the HGS land surface processes by comparing results of test problems to those obtained from the Canadian Land Surface Scheme (CLASS) (*Verseghy*, 2000).

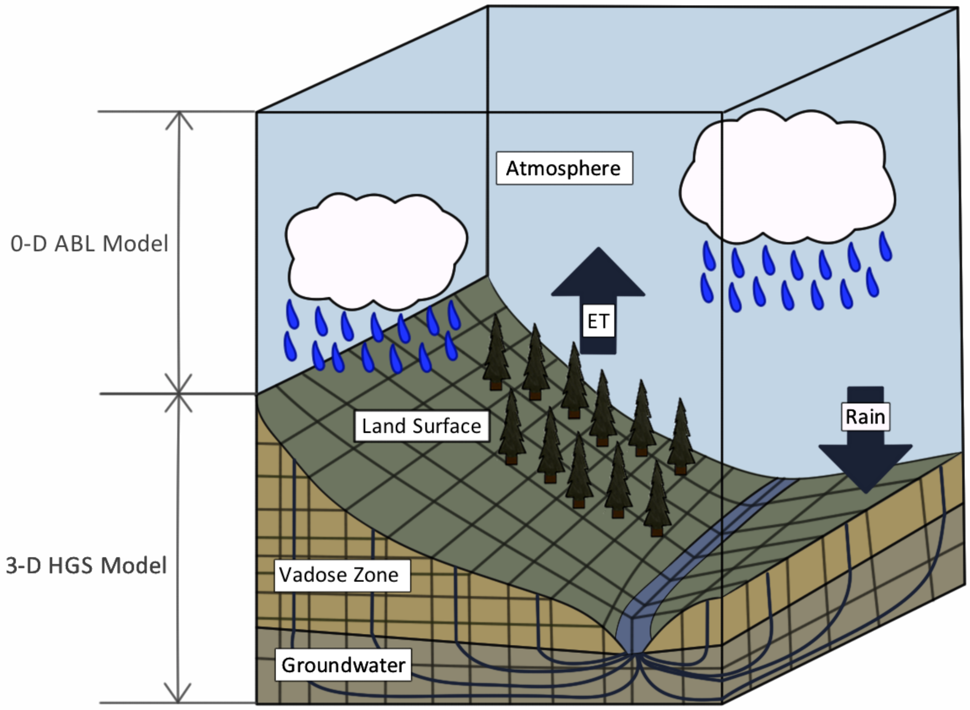

Figure 2.1: Coupled atmosphere, surface and subsurface conceptual model. The dark lines show a 3-D finite element mesh for the surface/subsurface discretization. The 0-D atmospheric domain is represented as a single averaged element above the surface.

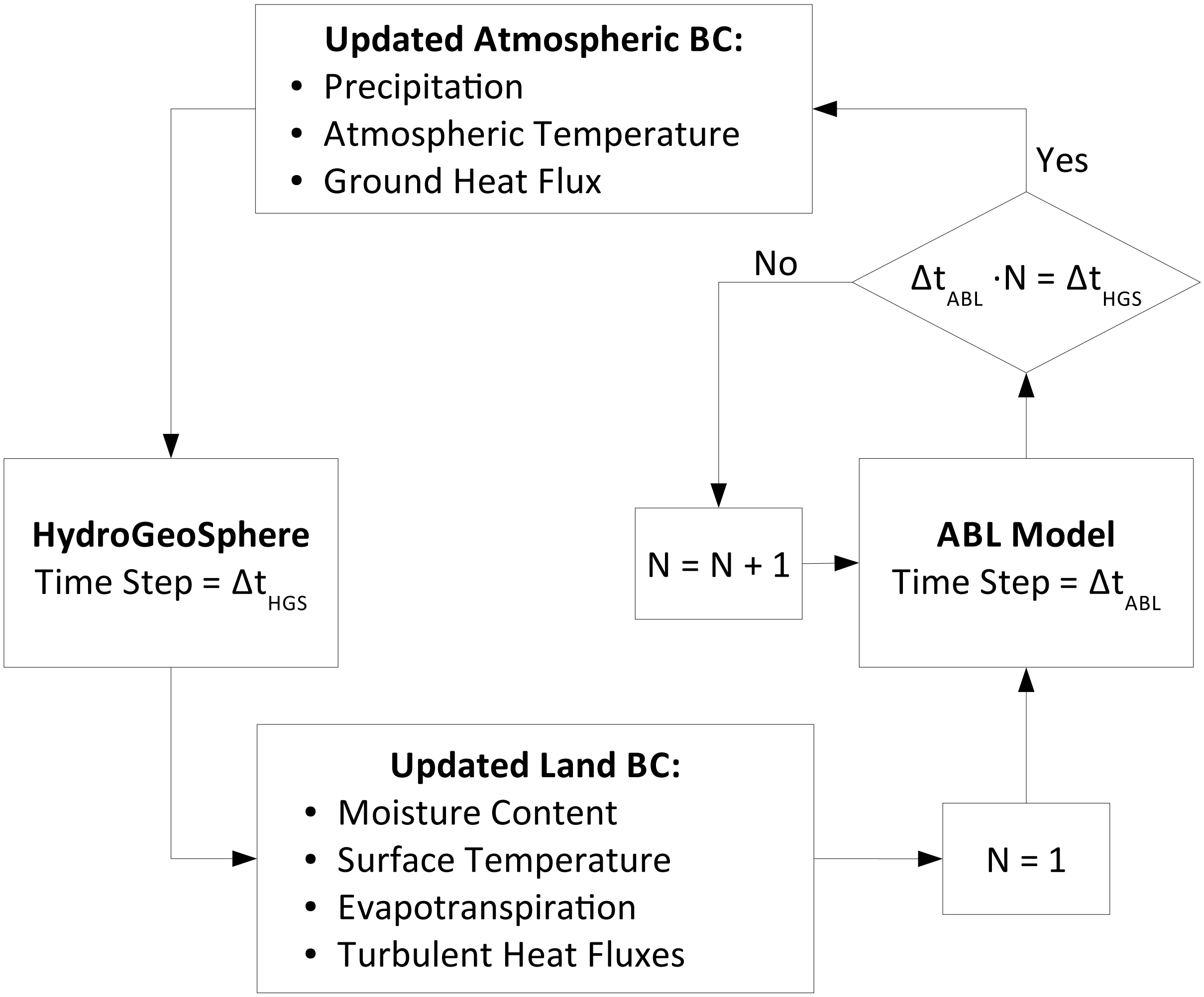

Figure 2.2: Coupling flow chart. HydroGeoSphere represents the surface/subsurface component while the ABL Model with a sub-time loop handles the atmospheric domain.

Subsurface

The Richards' equation for variably-saturated conditions governs the subsurface flow in HGS. The general form implemented by HGS is:

$$S_w S_s \frac{\partial \psi}{\partial t} + \theta_s \frac{\partial S_w}{\partial t} \quad = \quad \nabla \cdot \left(\mathbf{K} \cdot k_r \nabla \left(\psi + z \right) \right) + \sum \Gamma_{ex} + Q \tag{2.1}$$

where S_w is the water saturation, S_s is the specific storage for the porous media, ψ is the pressure head, t is the time, θ_s is the saturated water content, $\mathbf{K}$ is the hydraulic conductivity tensor, z is the elevation head, Γ_{ex} is the volumetric fluid exchange rate between coupled domains, and Q represents external volumetric fluid sources and sinks. The relative permeability, k_r, is calculated as a function of the water saturation (e.g., (*Brooks and Corey*, 1964; *Van Genuchten*, 1980)). Evapotranspiration is internally calculated based on the *Kristensen and Jensen* (1975) method, which takes into account the availability of water versus the potential evapotranspiration. HGS' vegetation parameters include root zone depth and distribution (constant distribution, quadratic decay distribution, or cubic decay distribution), leaf area index, and soil saturation control.

Surface Water

Surface water flow, an implicitly integrated component of HGS, is solved at every time step using the common or dual-node approach. In HGS, overland flow is solved for over a two-dimensional mesh draped over the subsurface, and employs the diffusion wave approximation:

$$\frac{\partial \phi_o h_o}{\partial t} = \frac{\partial}{\partial x}\left(d_o K_{ox}\frac{\partial h_o}{\partial x}\right) + \frac{\partial}{\partial y}\left(d_o K_{oy}\frac{\partial h_o}{\partial y}\right) - d_o \Gamma_{ex} + Q \tag{2.2}$$

The Manning equation conductances, K_{ox} and K_{oy}, for the x and y directions are represented as:

$$K_{ox} = \frac{d_o^{2/3}}{n_x}\frac{1}{[\partial h_o/\partial s]^{1/2}} \tag{2.3}$$

$$K_{oy} = \frac{d_o^{2/3}}{n_y}\frac{1}{[\partial h_o/\partial s]^{1/2}} \tag{2.4}$$

where ϕ_o is the surface domain porosity, h_o is the water surface elevation, d_o is the depth of surface water, n_x and n_y are the Manning roughness coefficients, and s is the direction of the maximum surface slope.

Heat Transport

Heat convection and conduction on the land surface and in the subsurface employ the heat transport equation:

$$\frac{\partial \rho_b c_b T}{\partial t} = -\nabla \cdot (\mathbf{q}\rho_w c_w T - (k_b + c_b \rho_b \mathbf{D}) \cdot \nabla T) + G + Q_T + \Omega_0 \tag{2.5}$$

where T is the temperature, k_b is the thermal conductivity of soil, $\mathbf{q}$ is Darcy flux, $\mathbf{D}$ is the thermal diffusivity tensor, Q_T is a thermal source or sink, and Ω_0 is the thermal interaction between the surface/subsurface. The density and specific heat of water are ρ_w and c_w, respectively. Similarly, the density and specific heat of soil are ρ_b and c_b. The ground heat flux, G, is calculated by the ABL model (see Eq. 2.7) and only interacts with HGS' top surface layer. A two dimensional form of Equation 2.5 is used on the surface domain, whereas the three-dimensional form is used in the subsurface. As with the solution of the surface and subsurface water flow equations (Sections 2.1.1 and 2.1.1), the heat flow equations are solved simultaneously using a globally-implicit control volume finite element method. A complete description of the theoretical basis and the numerical solution procedures used in HGS can be found in *Aquanty, Inc.* (2015).

2.1.2 Atmospheric Boundary Layer

The ABL is the lowest layer in the troposphere and connects the earth's surface to the free atmosphere (*Stull*, 1988). During the day, the ABL is unstable and turbulent because the surface, heated by solar radiation, is warmer than the atmosphere. At night, however, the surface is cooler than the atmosphere, resulting in a stable boundary layer (*Wallace and Hobbs*, 2006). As an approximation of the rapid mixing within the ABL, the zero-dimensional ABL model is adapted from *Garratt* (1994) which simplifies the atmosphere's interactions to a homogenous, well-mixed layer with energy and water balance calculations.

The ABL model's single averaged element, shown in Figure 2.1, is directly attached to the top of HGS' surface domain and is primarily driven by the external input of solar shortwave radiation, while the rest of the energy and mass calculation (i.e. longwave radiation, sensible heat, latent heat, and precipitation) are internally calculated by the ABL model. The ABL model does not include the lateral transport of mass and energy, consequently limiting our solution domain to site and small catchment scales.

Energy Balance

Solar energy warms the earth's surface by shortwave radiation heating up the ground. After the surface is warmed by the sun, the ground emits longwave radiation back to the atmosphere. The atmosphere also emits longwave radiation back to the ground. The net energy to the ground surface from both shortwave and longwave radiation is shown as:

$$\mathrm{R}_{\mathrm{net}} = (1-\alpha)\mathrm{SW}_{\mathrm{dn}} + \sigma\epsilon_a T_a^4 - \sigma\epsilon_s T^4 \tag{2.6}$$

where α is the albedo, $\mathrm{SW}_{\mathrm{dn}}$ is the shortwave solar radiation, T_a and T are the atmospheric and surface temperatures, ϵ_a and ϵ_s are the atmospheric and surface emissivity, and σ is the Stefan–Boltzmann constant. The combination or sum of the long and shortwave energy fluxes is the net energy flux, $\mathrm{R}_{\mathrm{net}}$.

Equation 2.7, as shown below, combines into the energy balance all of the thermal exchanges between the atmosphere and surface, including the turbulent heat fluxes. The total combination of the net energy flux, latent heat flux, and sensible heat flux is:

$$\mathrm{R}_{\mathrm{net}} = LE + H + G \tag{2.7}$$

where LE is the latent heat flux and G is the ground heat flux. The sensible heat flux $H = \rho_a c_p G_a (T - T_a)$ is calculated as the difference between temperatures of the surface and atmosphere multiplied by the density of air ρ_a and the specific heat of air c_p. The atmospheric conductance, G_a, is the inverse of the atmospheric resistance and is calculated as a function of wind velocity (*Liu et al.*, 2007).

Water Balance

Above the ABL, the free atmosphere typically remains drier than the ABL and can reduce the averaged ABL humidity through entrainment. The time discretized moisture content water balance equation for the ABL model is described as:

$$\frac{\partial q_a}{\partial t} = \begin{cases} \frac{E}{\rho_a h_a} + \frac{\left(q_f - q_a\right)\left(\frac{\partial h_a}{\partial t} - W\right)}{h_a} & \text{if } \frac{\partial h_a}{\partial t} \geq 0 \\ \\ \frac{E}{\rho_a h_a} & \text{if } \frac{\partial h_a}{\partial t} < 0 \end{cases} \tag{2.8}$$

where q_f is the specific humidity in the free atmosphere, q_a is the specific humidity inside of the ABL, E is the surface moisture flux, W is the ABL subsidence rate, and h_a is the height of the ABL. Entrainment only occurs when the ABL is growing.

The theoretical rate that water can move from the earth's surface into the atmosphere is the potential evapotranspiration (PET) and is calculated within HGS-ABL using a Jarvis-type model (*Jarvis*, 1976), shown as:

$$PET = \begin{cases} \frac{\rho_a}{\rho_w (r_a + r_v)} \left(q^* - q_a\right) & \text{if } q^* \geq q_a \\ \\ 0 & \text{otherwise} \end{cases} \tag{2.9}$$

where r_a is the atmospheric resistance, r_v is the vegetative resistance function, and q^* is the saturation specific humidity. Equation 2.9 describes the PET as a proportion of the dryness of the air divided by the resistance of the air and vegetation. HGS calculates the actual ET from the updated atmospheric PET. Then, the ABL model uses the actual ET to find the latent heat flux as required by the atmospheric model:

$$\mathrm{LE} = \mathrm{ET} \cdot \lambda \cdot \rho_w \tag{2.10}$$

where λ is the latent heat of vaporization. As water accumulates in the ABL, the relative humidity, RH, increases and clouds form based on a parameterized exponential function (*Walcek*, 1994) and is shown as:

$$f(\%) = \min\left[f_{100}\exp\left(\frac{RH - 100\%}{100\% - RH_e}\right), 100\%\right] \tag{2.11}$$

where f_{100} is the precent cloud cover extrapolated at 100% relative humidity and RH_e is the e-folding relative humidity.

Excess water in the atmosphere is removed as precipitation once the humidity exceeds saturation. Next, the precipitation is applied to the surface domain of the hydrological model, and the specific humidity is set to saturation. The precipitation rate i is calculated as:

$$i = (q^* - q_a)\left(\frac{\rho_a}{\rho_w}\right)\left(\frac{h_a}{\Delta t}\right) \tag{2.12}$$

where h_a is the height of the atmospheric boundary layer, and Δt is the model's time step.

2.1.3 Model Coupling

A combined surface, subsurface, and atmospheric model is achieved by an explicit coupling technique between the surface/subsurface and the atmosphere. The first task is to calculate the surface/subsurface flow using Newton iterations until convergence is achieved for the coupled nonlinear surface and subsurface flow equations. Once the flow is solved, HGS saves and passes the actual evapotranspiration on to the ABL model as shown in step two.

The atmospheric model updates the cloud cover using Equation 2.11 in order to calculate the new energy balance with Equations 2.6, 2.7, and 2.10. The atmospheric water balance, Equations 2.9 and 2.12, calculates the new precipitation and potential evapotranspiration for the next surface/subsurface flow solver time step. From the energy balance equations, the calculated ground heat flux is updated for the current heat transport solver in HGS. The last atmospheric step is to update the required parameterized variables, including the moisture flux, boundary layer height, and atmospheric temperature.

The last step in the coupled simulation is to perform HGS' heat transport calculations. The atmospheric energy calculated by the energy balance Equation 2.7 is updated and the heat transport equation, Equation 2.5 is solved. The final coupled process is to update the grid-averaged surface temperature for the next atmospheric computational time step. The pseudocode, shown in 2.2, runs through a single coupled model time step.

The sub-time stepping routine shown in Figure 2.2 drastically decreases the total simulation time in the coupled HGS-ABL model. Solving the implicit global matrix in HGS is the most numerically costly part of each time step, because the ABL model simulation is a simple set of scalar-vector operations. By increasing the number of independent sub-time steps, N, the atmospheric model runs at a much smaller time step, Δt_{ABL}, while HGS continues to run at a longer time step value, Δt_{HGS}. By increasing the time step ratio, the coupled simulation speed drastically increases. Our computational approach implements a time-weighted arithmetic mean to average the atmospheric components over the multiple smaller time steps.

2.2 HGS-ABL Pseudocode

The HGS pseudocode, shown in Figure 2.3, is for a single time step of the coupled HGS-ABL model. The bold items represent the information passed from HGS to the ABL model and the italics represent the information passed from the ABL model to HGS. HydroGeoSphere initiates the time step with the surface/subsurface flow solved by the Newton-Raphson solver. After calculating the land surface water balance, the ABL model computes the energy and water balance equations. Finally, HGS executes its heat transport solver and updates the land surface temperature.

```
Begin time step
    1. Surface/subsurface flow solver (HGS) - Implicit
        a. Newton-Raphson iterative solver
        b. Update actual evapotransipiration
    2. Atmospheric computation loop (ABL) - Explicit
        a. Cloud cover
        b. Energy balance: SW, LW, H, and LE
        c. Update precipitation and PET
        d. Update ground heat flux
        e. Atmospheric parameterization:
           Moisture entrainment flux
           Boundary layer height
           Atmospheric temperature
    3. Heat transport solver (HGS) - Implicit
        a. Newton-Raphson iterative solver
        b. Update surface temperature
End time step
```

Figure 2.3: HGS-ABL model's pseudocode for a single time step.

2.3 Noah LSM Comparison

Numerical models are generally validated against simple analytical solutions. However, because no known analytical solution exists due to the complex nature of the environmental interactions, HGS was compared against the Noah LSM for a simple test case of a two-meter vertical 1-D column. Two simulations were implemented with the same model conditions including a steady-state fully-saturated subsurface, similar vegetation (grass) and soil types (sand) parameters, with the same subsurface domain discretization ($dz = 0.2$ m). Groundwater flow was turned off for the comparison between the two models because the Noah LSM does not properly handle the Richards' equation and subsurface saturated-zone flow. For both cases, we fixed the atmosphere to a constant temperature (10°C), humidity (20%), and downward long-wave radiation (350 W/m^2), but used a diurnal solar radiation cycle with a peak radiation of 850 W/m^2.

The two models correspond well over the 10 day simulation period (Figure 2.4). In order to achieve this fit, the Noah LSM was set to have a vegetative resistance of 40 s/m while the HGS model used an effective vegetative resistance of 50 s/m. Prior to the adjustment of the vegetative resistance, HGS yielded a slightly larger evapotranspiration rate and latent heat flux than the Noah LSM because of the different numerical implementations between each of the two models. After the adjustment, the latent heat flux responded nearly the same in both numerical models, with a root-mean-square deviation (RMSD) of 26.6 W/m^2. The Noah LSM exhibited sharp surface temperature and sensible heat flux peaks during the night when the surface temperature dipped below the constant 10°C atmosphere. Even though HGS did not show the same strong peak behavior, the overall temperature and sensible heat flux showed a satisfactory correlation between the two models with an RMSD of 0.9°C and 30.2 W/m^2, respectively.

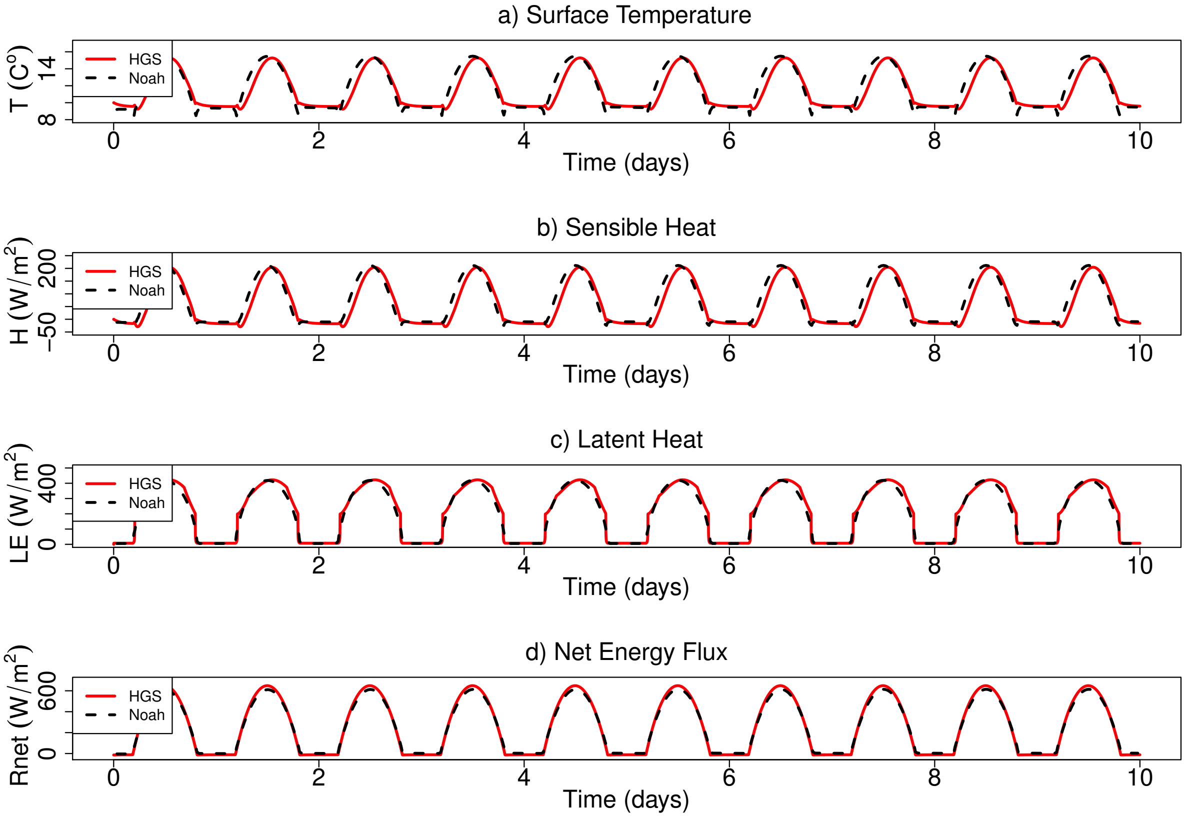

Figure 2.4: Noah LSM comparison: Surface temperature, sensible heat flux, latent heat flux, and net energy flux for a 10 day comparison of the HGS model (solid red line) to the Noah LSM (dash black line).

2.4 Illustrative Example

To display the abilities of the coupled HGS-ABL model, an elementary example was used to simulate prolonged drought conditions. The surface/subsurface model domain, a 2-D V-shaped catchment shown in Figure 2.5, is 1 km long, 10 m wide, and has a thickness ranging between 8 m and 10 m. The numerical mesh was resolved to a 10 m horizontal discretization with 40 subsurface layers. The grass vegetation was approximated with a cubically distributed shallow root zone of 1 m and a leaf area index of 2.5. Five wells were monitored (labeled Well #1 to #5), and they are located at 100 m intervals at a vertical elevation of five meters, as shown in Figure 2.5.

The solar forcing for the ABL model was a diurnally varying downward shortwave input with a maximum amplitude of 850 W/m^2. In order to spin-up the ABL model, HGS' subsurface domain initially ran (0-20 days) with a constant head boundary condition of 8 m. After running for 20 days, the fixed head condition was removed and a no flow boundary was added around the domain perimeter to prevent any additional water from entering or leaving the model. Additionally, HGS' heat transport component implemented a no flux boundary around the subsurface perimeter.

Extended drought conditions decreased the subsurface head after the first 20 days as seen in Figure 2.6. Until day 30, the available water sufficiently maintains an average daily latent heat flux above 50 W/m^2 and a sensible heat flux below 60 W/m^2 as shown in Figure 2.7. With a decreasing near-surface soil moisture content, the quantity of available water for evapotranspiration decreases, producing lower latent and higher sensible heat fluxes. By the end of the 100 day simulation, the daily average latent and sensible heat fluxes changed to 2.7 W/m^2 and 68.2 W/m^2, respectively. Overall, the low latent heat fluxes are due to the low initial groundwater levels. Additionally, the daily averaged sensible heat fluxes are smaller than expected because the nightly fluxes were negative. Averaging the negative nightly sensible heat with the daily positive sensible heat results in lower than expected values.

Correspondingly, the atmospheric and surface temperatures increased in response to the overall decrease in available soil moisture as seen in Figure 2.8. Because of the decrease in actual ET and latent heat, the temperatures began to increase after 30 days. The mean atmospheric and surface temperature for the first 30 days was 20.0 and 24.5 °C, and by the end of the 100 day simulation the average daily temperatures warmed to 29.9 and 35.7 °C, respectively.

The time series of hydraulic head, Figure 2.6, clearly depicts why the atmosphere has a 10 day lag period after the first 20 days of simulation. For the first 20 days, the subsurface head does not change because the external boundary condition forces all of the subsurface nodes to remain at a constant value equal to 8 m. From 20 to 30 days, the hydraulic head rapidly decreases, especially in Wells #4 and #5. The principal reason for this decrease is because Wells #4 and #5 are located near the ground surface, allowing the shallow grass root zone to transpire the most water. Wells #1, #2, and #3 are located deeper below the ground surface and exhibit less drawdown because they are less affected by transpiration.

After 55 days, the rate of drawdown in the wells drastically decreases because the water table has been sufficiently lowered such that all of the available soil moisture is below the root zone. At this point, the higher heads in Wells #1, #2, and #3 reflect the influence of regional groundwater flow and are providing water for evapotranspiration in the bottom of the V-notch. As the simulation continues, less water is available for evapotranspiration resulting in a decrease in latent heat flux. Furthermore, a decrease in the latent heat flux corresponds with an increase in atmospheric and surface temperatures and an increase in PET. Even though the PET continues to increase, the actual evapotranspiration decreases because of the lack of available water in the near surface.

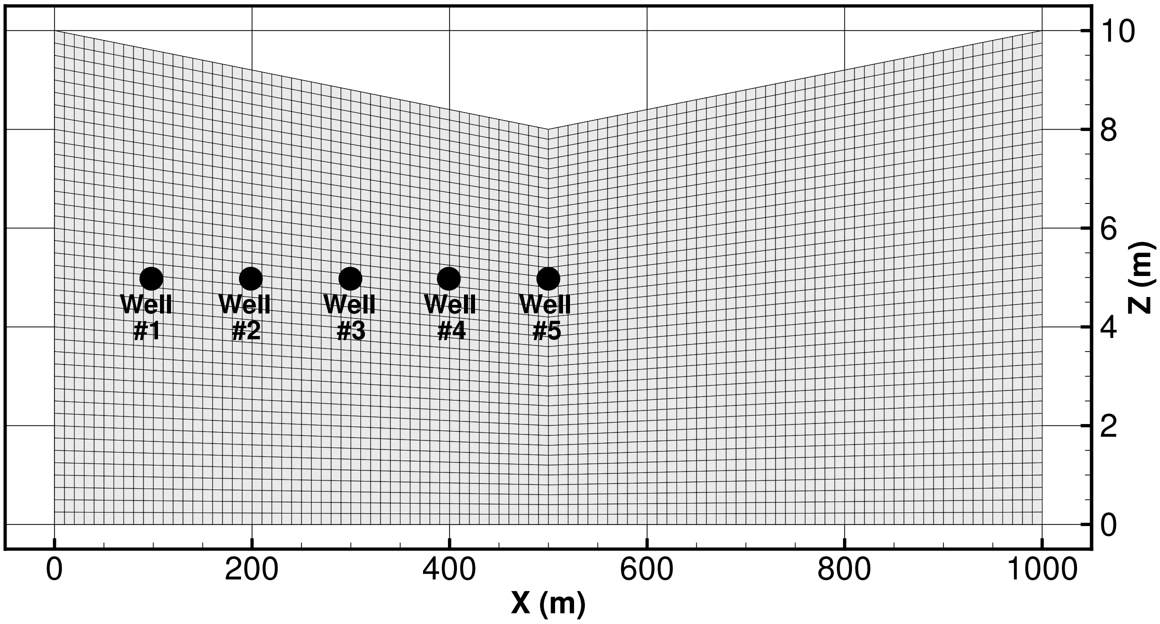

Figure 2.5: Illustrative Example: Vertical section showing the discretization for the V-catchment domain, which is 1 km long and 10 m wide. The domain ranges between 8 m and 10 m in thickness.

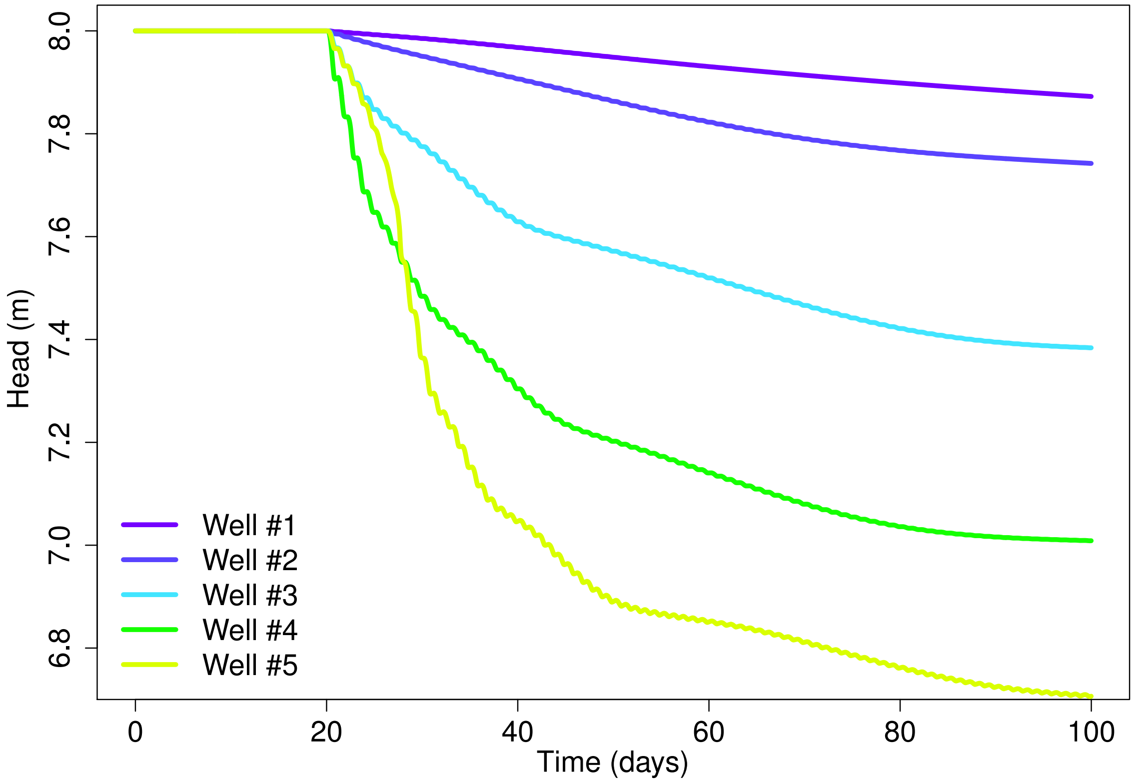

Figure 2.6: Illustrative Example: Hydraulic head response for Wells #1 to #5.

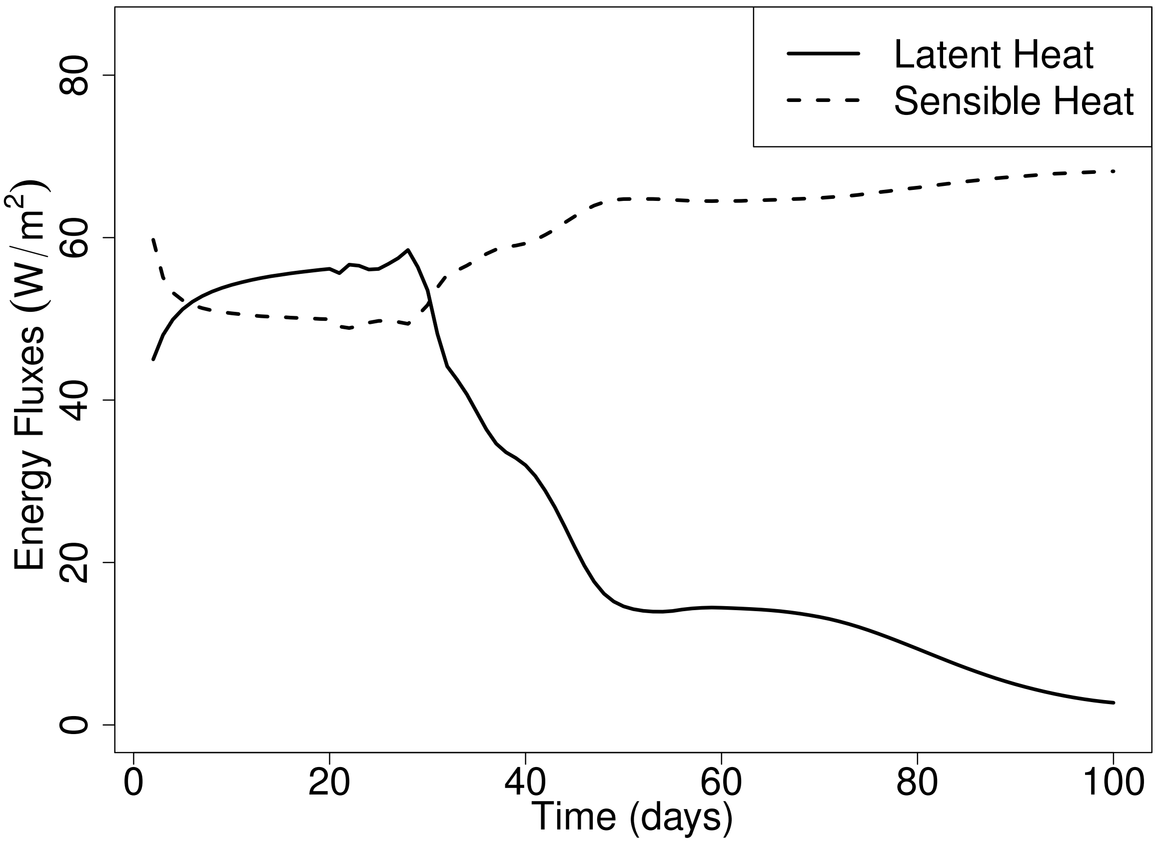

Figure 2.7: Iluustrative Example: Daily averaged latent and sensible heat fluxes for the coupled model system.

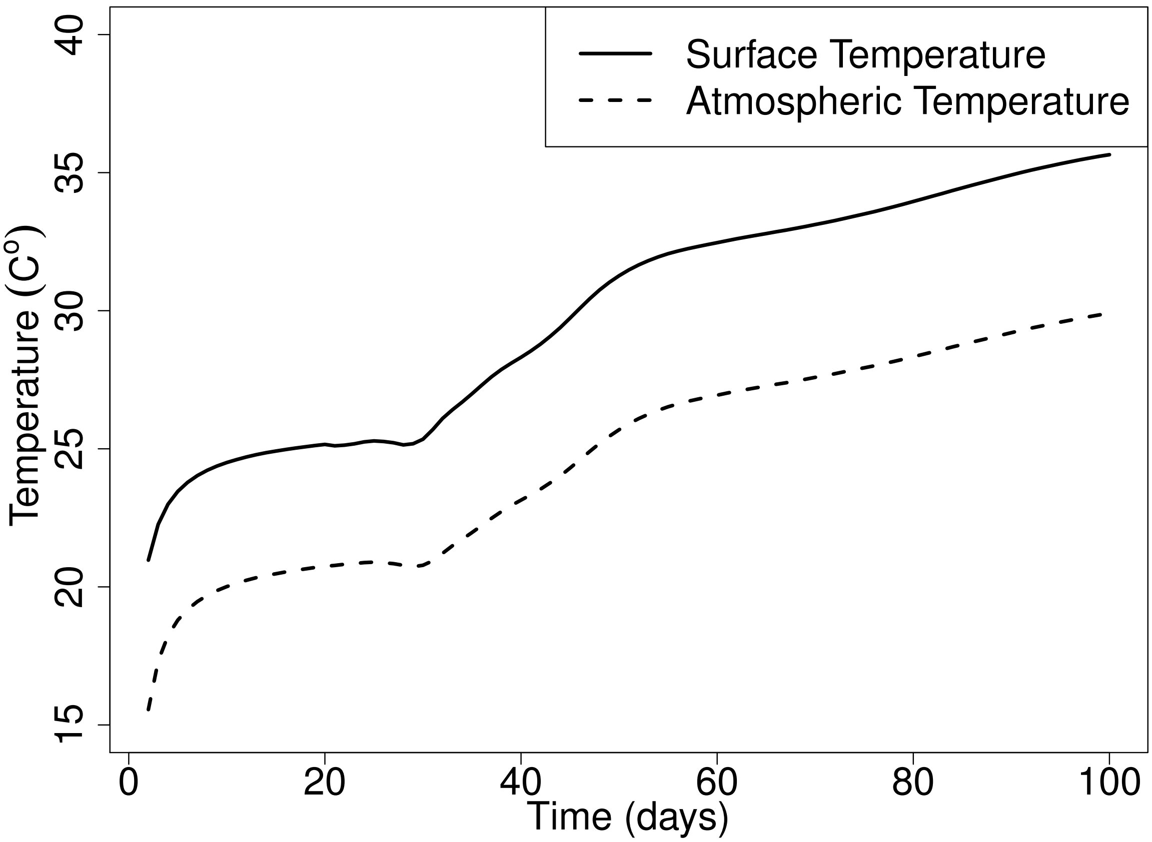

Figure 2.8: Illustrative Example: Daily averaged atmospheric and land surface temperatures for the 100 day HGS-ABL simulation.

2.5 Subsurface Temperature

Land surface models use a shallow near-surface domain to model the moisture and heat transport within the subsurface. The heat stored in the subsurface buffers the daily temperature variations by emitting sensible heat and longwave energy. For extended simulations, the thickness of the subsurface becomes an important factor, requiring a thicker subsurface that properly regulates the atmospheric dynamics. Two similar 2-D V-shaped catchments are analyzed, both solved with the HGS-ABL model. The first model is 2.0 m thick, which is the same thickness of the land surface used in the Noah LSM. The second model has an 8.0 m thick land surface and illustrates the advantage of using a fully coupled 3-D hydrology/heat transport model. Both of the domains have a vertical discretization of 0.2 m with the same hydrological and atmospheric parameters as described in Section 2.4. The model simulations were initialized with a 20 day spin up and then monitored for an additional 80 days.

The final 100-day subsurface temperatures, shown in Figure 2.9, qualitatively describe a warmer subsurface for the smaller 2.0 m domain while the larger 8.0 m domain remained cooler. The 8.0 m domain is cooler because it has four times the thermal heat capacitance resulting in a subdued heating profile. Additionally, Figure 2.10 displays the subsurface temperature along a profile ($x = 500$ m, $y = 5$ m) for both of the domains over the 100 day period. For first 25 days, the 2.0 m model has virtually no temperature difference in the first meter below ground surface compared to the 8.0 m model (8.0 m to 7.0 m), but for the second meter (7.0 m to 6.0 m), the two temperature profiles deviate to a maximum of 1.04°C. For the next 75 days, the 2.0 m domain continues to increase in temperature at a faster rate than the 8.0 m domain. By the 100th day, the spatially averaged 2.0 m subsurface domain temperature increased by 5.19°C over the 8.0 m domain.

As a result of the increased subsurface temperatures, the 2.0 m domain had a corresponding increase in mean daily atmospheric and surface temperatures shown in Figure 2.11. The final atmospheric and surface daily averaged temperatures for the 2.0 m domain were 32.3°C and 38.0°C, while the 8.0 m domain maintained cooler temperatures of just 29.6°C and 35.3°C for the atmosphere and surface. Overall, by reducing the thickness of the LSM by six meters, the model produced a 100-day bias that increased the mean daily atmospheric and surface temperatures by 2.7°C.

A thicker domain increases the subsurface-atmospheric memory. The influence of model depth becomes quite important for extended simulations with extreme radiative forcings. The required minimum depth of the subsurface model is case specific and thus requires attention in its selection.

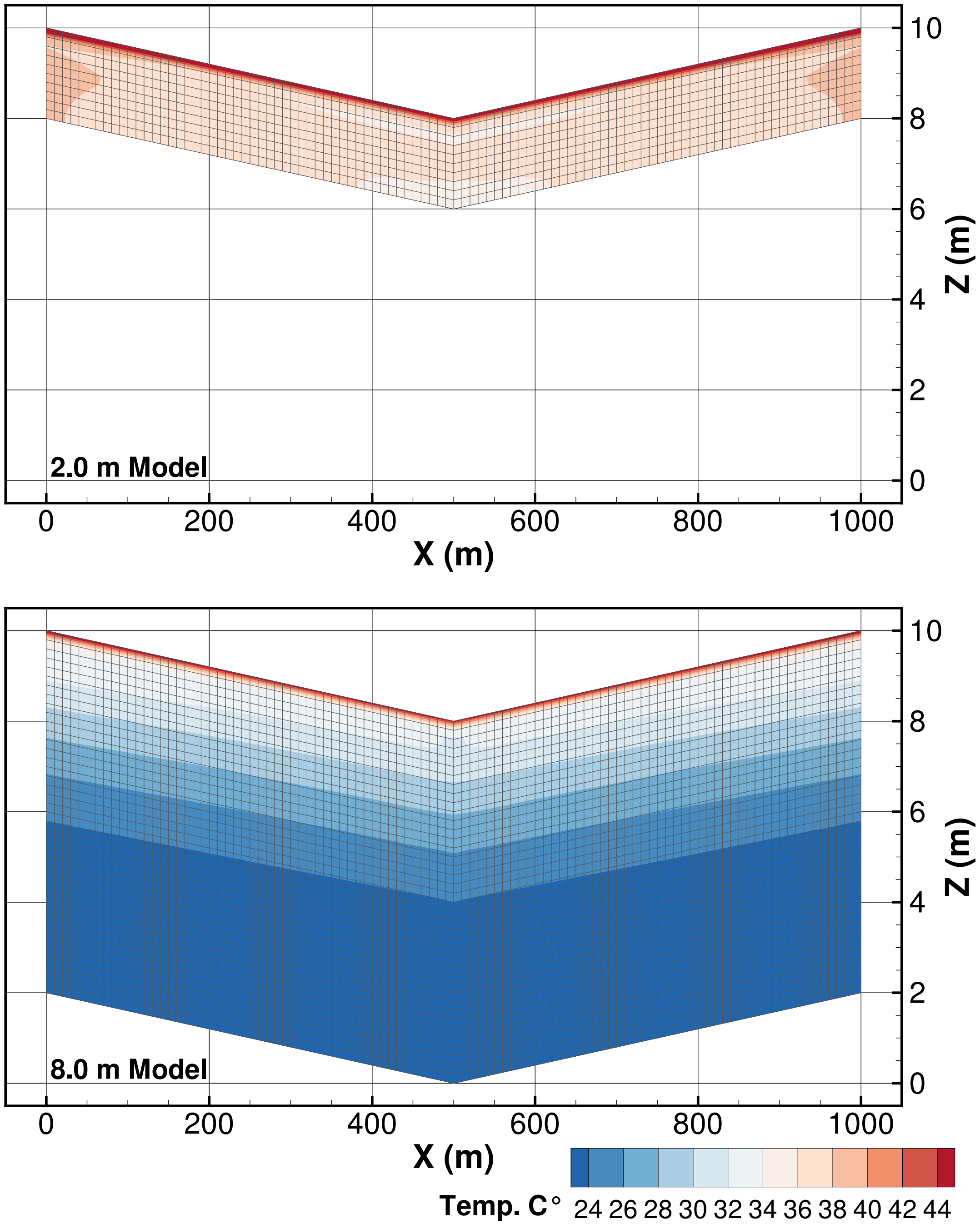

Figure 2.9: Subsurface Temperature: The 2.0 m case shown on top and 8.0 m case shown on bottom, both at 100 days.

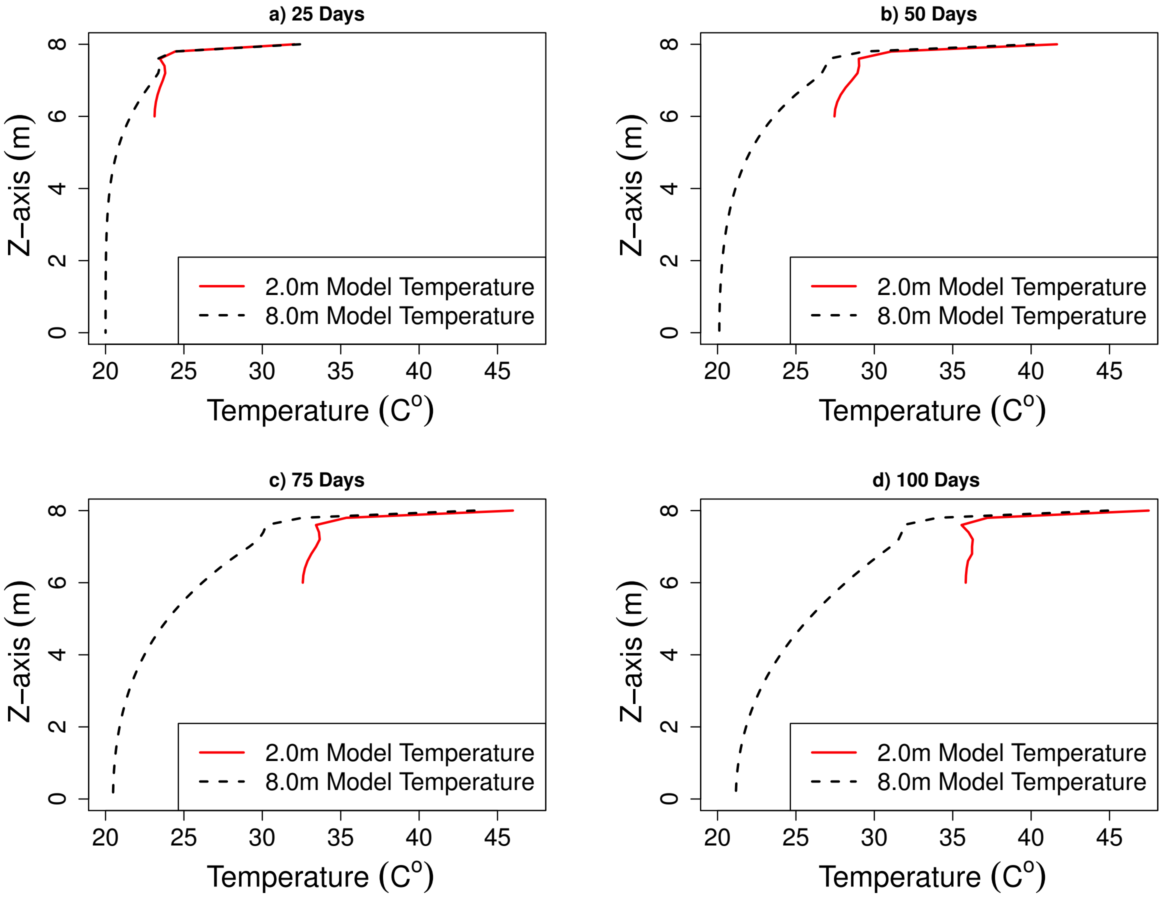

Figure 2.10: Subsurface Temperature: The 25, 50, 75, and 100 day subsurface temperature profile for the 2.0 m model (shown in red) and 8.0 m model (shown in black) at x = 500 m.

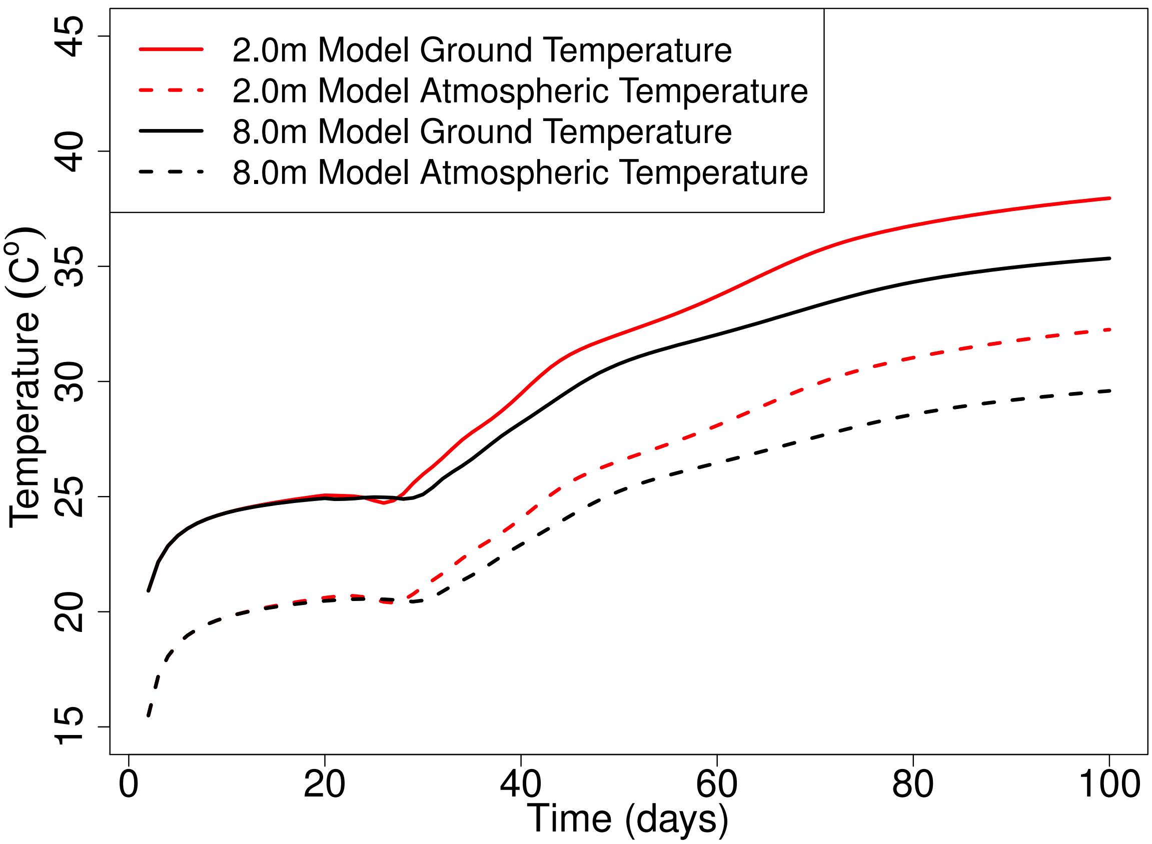

Figure 2.11: Subsurface Temperature: Comparison of the daily averaged atmospheric and land surface temperatures for the 2.0 m (shown in red) and 8.0 m models (shown in black).

2.6 Root Zone Depth

Previous coupled LSM efforts cannot simulate a deep root-zone depth because of the inherent limitations of the Noah LSM. One of the benefits of using HGS is that it is not constrained to a prescribed subsurface thickness while maintaining the appropriate energy and water balance calculations. Eight numerical simulations were performed using the HGS-ABL model, with root depths of 0.1, 0.5, 1.0, 2.0, 3.0, 4.0, 5.0, and 6.0 m, to test the impact of root-zone depth on the atmosphere. The simulation domain used the same parameters as provided in Section 2.4 and this example was simulated in three dimensions. The domain is 100 m in the x and y-directions with a 10 m grid size, a thickness of 6 m along the z-axis with a 0.15 m vertical discretization, and it also has a gentle 2.0% slope along the z-axis. The initial condition for the moisture is shown in Figure 2.12.

The simulation was run for 10 days to spin up the atmospheric model, and then it was run for an additional 90 days. The atmospheric results, including temperature and turbulent heat fluxes, are shown in Figure 2.13. The corresponding head results are shown for well #1 (x = 50 m, y = 65 m) and well # 2 (x = 50 m, y = 25 m) in Figures 2.14 and 2.15.

The shallower rooting depth result in a smaller latent heat flux, producing higher temperatures than the deeper root cases. The shallow root-zone models quickly produced a drop in latent heat flux; the latent heat flux for the 0.1 m root depth case quickly decreases after just 25 days. The cause of the decrease in latent heat is clearly evident in the results for well #1; at day 25 the rate of decline of head for the 0.1 m root zone case drastically slows indicating that the evapotranspiration has decreased. Furthermore, a similar behav-

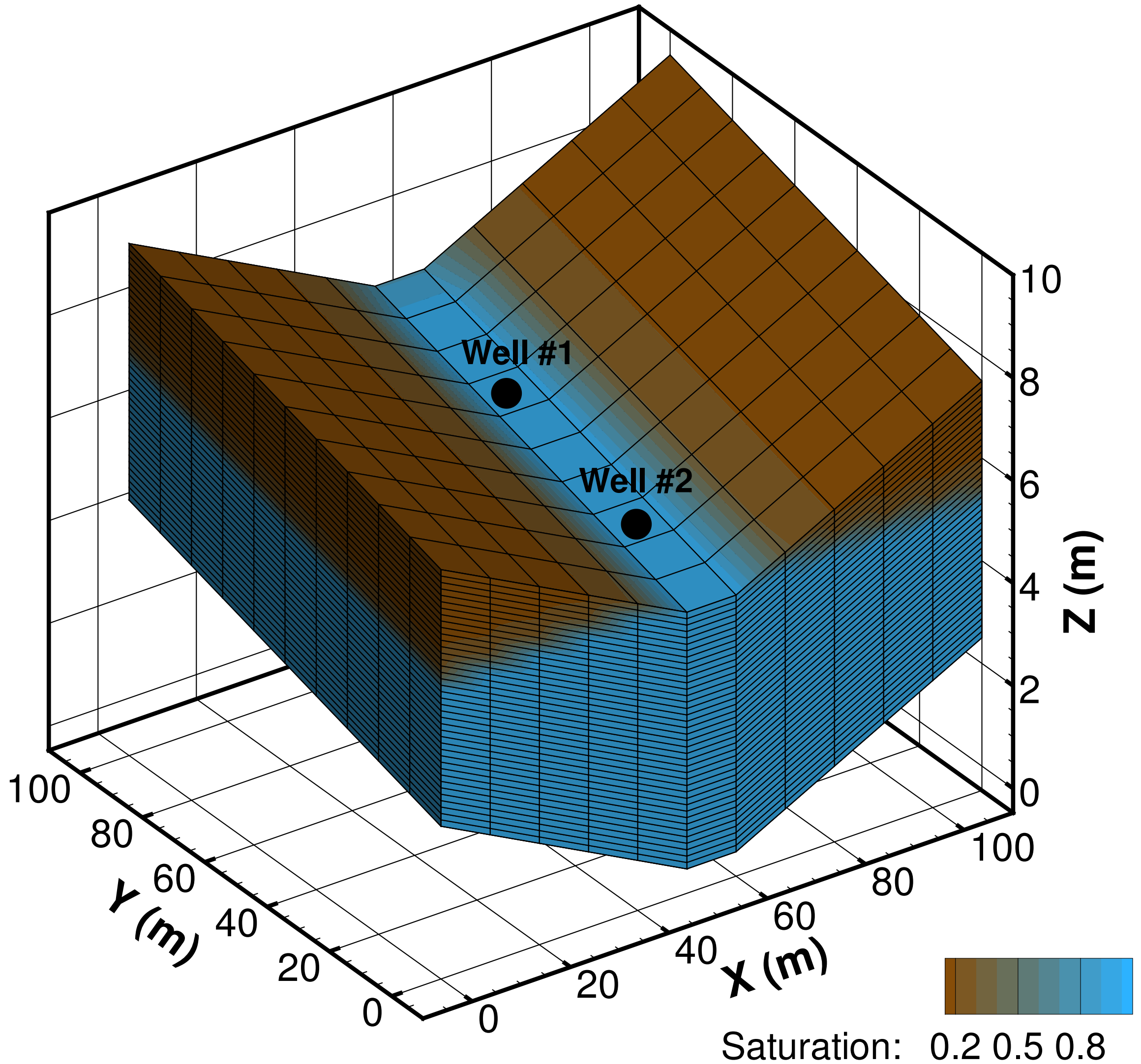

Figure 2.12: Effect of Root-Zone Depth: Initial subsurface saturations in the model domain.

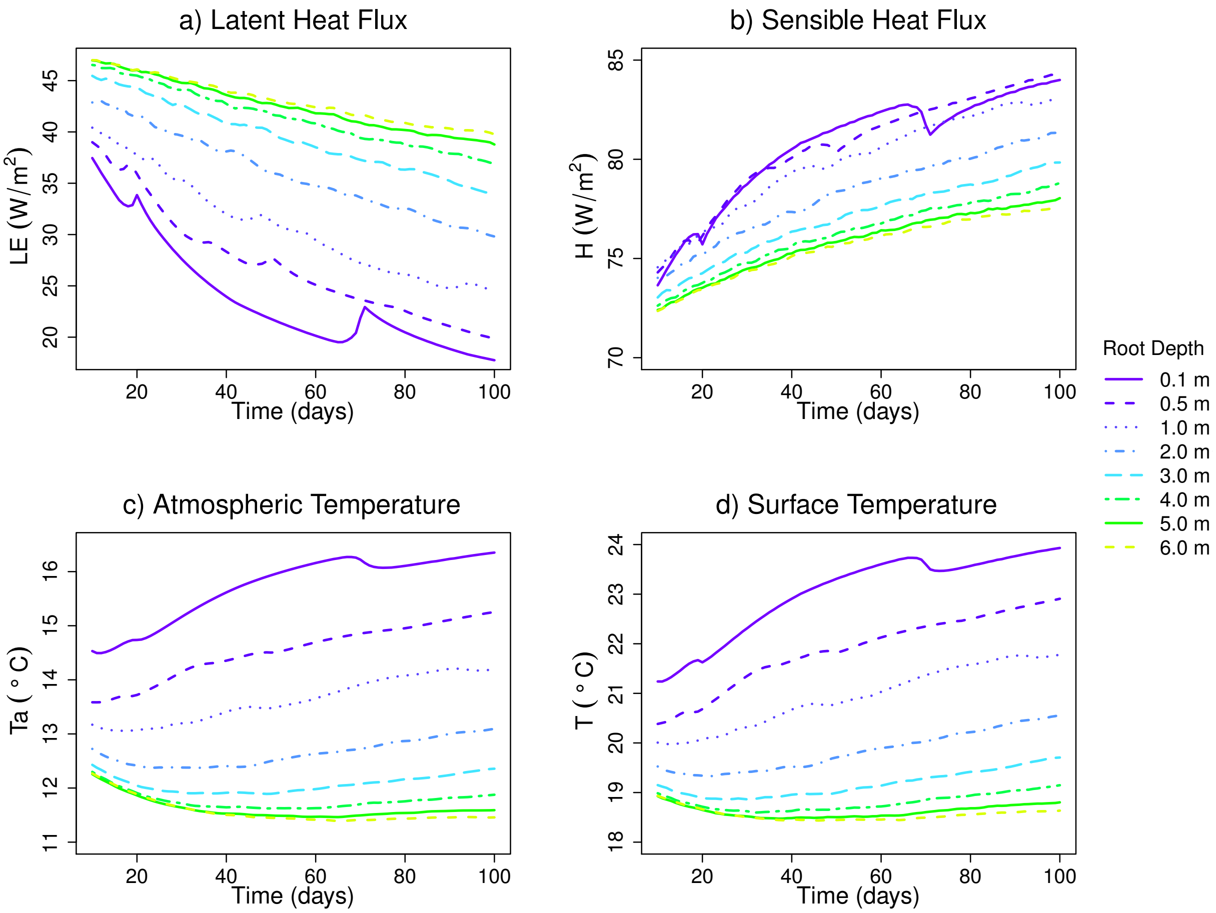

Figure 2.13: Effect of Root-Zone Depth on latent and sensible heat fluxes, atmospheric temperature, and land surface temperature.

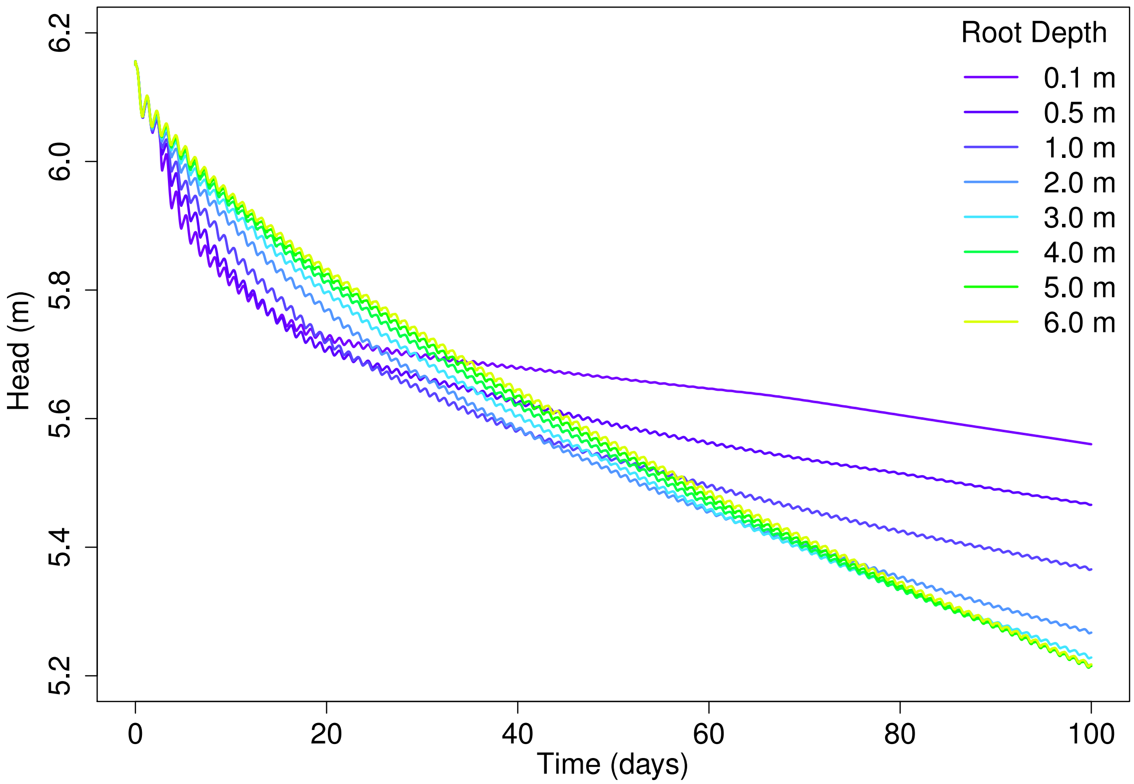

Figure 2.14: Effect of Root-Zone Depth on hydraulic head for well #1.

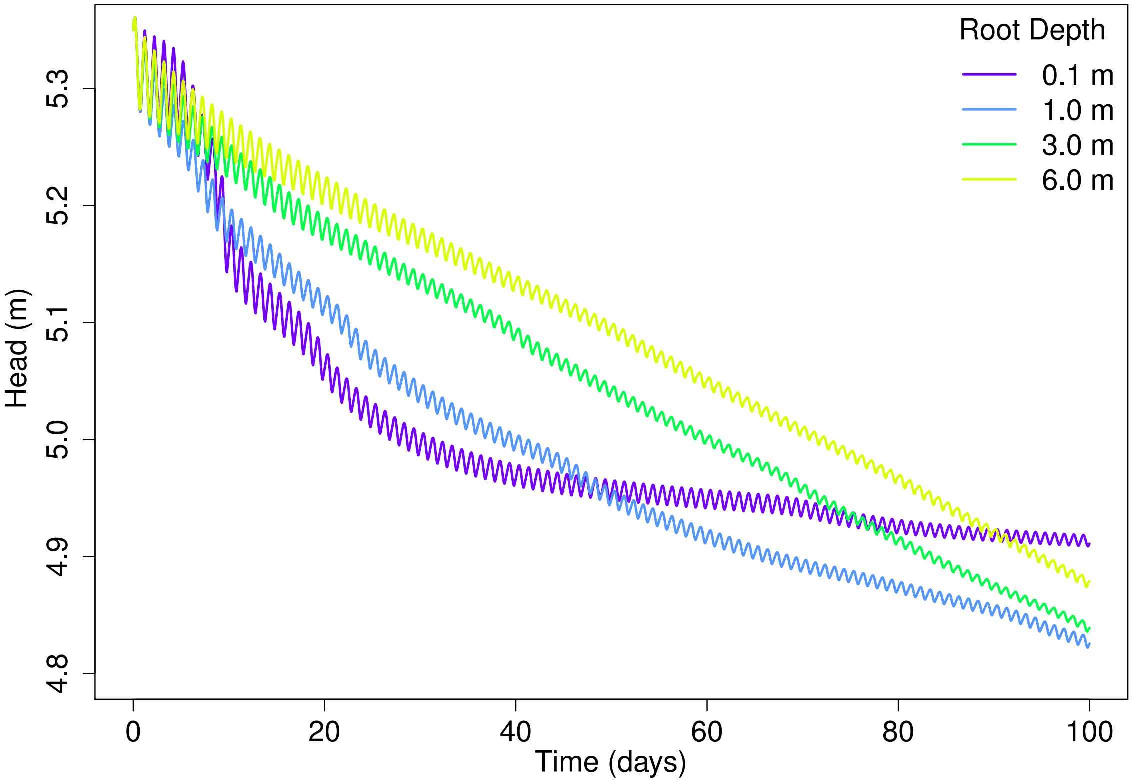

Figure 2.15: Effect of Root-Zone Depth on hydraulic head for well #2.

ior is exhibited in well #2, where the rate of decline of head starts to decrease at day 35. The head in well #1 ceases to decline earlier than well #2 because well #2 is down gradient and is supplied with regional groundwater flow.

The deeper root zone models continue to transpire water from the subsurface resulting in a larger decrease of the water table with time. The deeper roots act as a buffer to the environment and are able to keep the atmosphere and land surface at a nearly constant daily average temperature. The marginal buffering capacity of a deeper root zone declines once the roots exceed 3.0 m.

2.6.1 Water-Level Fluctuation

Water-level oscillations, shown in Figures 2.14 and 2.15, are a common phenomena observed in environments with phreatophytic vegetation. When the sun rises each day, plants open their stomata and transpire groundwater taken up by the roots, resulting in a lowered groundwater table. At night the plants close their stomata, which stops transpiration and the groundwater table recovers from regional flow. These fluctuating behaviors are only noticeable when the groundwater table is close to the surface, the vegetation root zone is below the water table, transpiration is more dominant than evaporation, and no additional water is added to the surface. *White* (1932) hypothesized that daily water-level oscillations, observed in wells, could be used to approximate evapotranspiration rates, ET:

$$ET = S_y \left(\frac{\Delta s}{\Delta t} + R \right) \tag{2.13}$$

where S_y is the effective specific yield and Δs is the average water level response over one day, Δt. The net groundwater flux, R, is the rate of hydraulic response during the night, because transpiration is approximately equal to zero and the only process is the regional groundwater flow recharging the aquifer. Recent work by *Runyan and Welty* (2010); *Carlson Mazur et al.* (2014) provide a more detailed explanation of the White method.

Applying White's method to the water level data from Wells #1 and #2, Tables 2.1 and 2.2, we see a strong correlation between the calculated evapotranspiration and the distance along the y direction (the y-axis is parallel to the primary flow direction). Well #2 located in the lowlands, generally over predicted the average evapotranspiration directly calculated by HGS-ABL, while Well #1 located in the highlands, under-predicted the average evapotranspiration. Additional work beyond the scope of this thesis is required to explore possible ways to better interpret actual evapotranspiration rates from water level data.

Table 2.1: White analysis of fluctuating head data for Well #1, at 20 days.

Root Depth (m)	S_y	$\frac{\Delta s}{\Delta t}$ (m/s)	R (m/s)	Calculated ET (m/s) (White 1932)	Actual ET (m/s) (HGS model)
1.0	0.28	$8.1 \cdot 10^{-8}$	$2.1 \cdot 10^{-7}$	$8.1 \cdot 10^{-8}$	$6.2 \cdot 10^{-8}$
2.0	0.28	$1.2 \cdot 10^{-7}$	$8.5 \cdot 10^{-8}$	$5.9 \cdot 10^{-8}$	$6.8 \cdot 10^{-8}$
3.0	0.28	$1.2 \cdot 10^{-7}$	$6.5 \cdot 10^{-7}$	$5.2 \cdot 10^{-8}$	$7.3 \cdot 10^{-8}$
4.0	0.28	$1.2 \cdot 10^{-7}$	$5.7 \cdot 10^{-8}$	$5.0 \cdot 10^{-8}$	$7.5 \cdot 10^{-8}$
5.0	0.28	$1.2 \cdot 10^{-7}$	$5.3 \cdot 10^{-8}$	$4.8 \cdot 10^{-8}$	$7.6 \cdot 10^{-8}$
6.0	0.28	$1.1 \cdot 10^{-7}$	$5.2 \cdot 10^{-8}$	$4.7 \cdot 10^{-8}$	$7.6 \cdot 10^{-8}$

Table 2.2: White analysis of fluctuating head data for Well #2, at 20 days.

Root Depth (m)	S_y	$\frac{\Delta s}{\Delta t}$ (m/s)	R (m/s)	Calculated ET (m/s) (White 1932)	Actual ET (m/s) (HGS model)
1.0	0.28	$5.4 \cdot 10^{-8}$	$4.8 \cdot 10^{-7}$	$9.5 \cdot 10^{-8}$	$6.2 \cdot 10^{-8}$
2.0	0.28	$4.7 \cdot 10^{-8}$	$4.9 \cdot 10^{-7}$	$1.5 \cdot 10^{-7}$	$6.8 \cdot 10^{-8}$
3.0	0.28	$4.7 \cdot 10^{-8}$	$5.4 \cdot 10^{-7}$	$1.6 \cdot 10^{-7}$	$7.3 \cdot 10^{-8}$
4.0	0.28	$4.9 \cdot 10^{-8}$	$5.5 \cdot 10^{-7}$	$1.7 \cdot 10^{-7}$	$7.5 \cdot 10^{-8}$
5.0	0.28	$4.6 \cdot 10^{-8}$	$5.7 \cdot 10^{-7}$	$1.7 \cdot 10^{-7}$	$7.6 \cdot 10^{-8}$
6.0	0.28	$3.9 \cdot 10^{-8}$	$5.9 \cdot 10^{-8}$	$1.7 \cdot 10^{-7}$	$7.6 \cdot 10^{-8}$

Chapter 3

HydroGeoSphere Weather Research and Forecasting Model

Water cycle modelers typically subdivide the environment into multiple parts and independently simulate each region. The most common approach is to first run the atmospheric model, and then apply its output to a hydrologic simulation. Although sequential modeling may be seen as the best practice, current climate models do not correctly handle the near surface water balance, which may produce large simulation bias once forecasts exit their calibration envelope. A fully-coupled framework should have more skill than serial methods because the hydrologic model would replace the climate model's shallow earth assumption, producing a dynamically linked atmosphere, surface, and subsurface system. For this reason, it is believed that a fully-coupled water cycle model follows the famous phrase *the whole is greater than the sum of its parts.* In this chapter we explore the fundamentals of coupling an advanced hydrologic model, HydroGeoSphere, to a mesoscale meteorological model, Weather Research and Forecasting (WRF Model Version 3.7.1, August 14, 2015).

3.1 HydroGeoSphere

HydroGeoSphere is a fully-integrated, globally implicit, finite difference or control-volume finite element, surface and variably-saturated subsurface flow model with evapotranspiration processes, solved by a Newton-Raphson parallelized solver and an adaptive time-stepping scheme (*Therrien and Sudicky*, 1996; *Hwang et al.*, 2014; *Park et al.*, 2009). HGS has been implemented over a large range of scales including small-scale test catchments (*Jones et al.*, 2008; *Abdul*, 1985; *Aquanty, Inc.*, 2015), regional flow problems (*Sudicky et al.*, 2008), drainage basins (*Bolger et al.*, 2011), and continental scale problems (*Chen*, 2015). Furthermore, HGS was adapted to include heat transport processes and was used as a LSM coupled to an atmospheric boundary layer model (*Brookfield et al.*, 2009; *Davison et al.*, 2015).

HGS implements the non-linear three-dimensional variably-saturated Richards' equation for subsurface flow:

$$S_w S_s \frac{\partial \psi}{\partial t} + \theta_s \frac{\partial S_w}{\partial t} = \nabla \cdot (\mathbf{K} \cdot k_r \nabla(\psi + z)) + \sum \Gamma_{ex} + Q \tag{3.1}$$

where Γ_{ex} is the internal fluid exchanges between domains (surface, subsurface, fractures, macropores, and tile drains) and Q is the external fluid exchanges (pumping, evapotranspiration). The known constants S_s, z, θ_s, and $\mathbf{K}$ are the specific storage, elevation head, saturated water content, and hydraulic conductivity, respectively. The water saturation, S_w, and the relative degree of permeability, k_r, are functions of the pressure head, ψ, which is approximated by lookup tables or numerical parametizations (e.g., Brooks and Corey, van Genuchten).

The two-dimensional surface domain is draped over the subsurface domain, and the two domains are directly linked by applying either the common node or dual node techniques. The common node method enforces the exact same head values for each shared node, while the dual node approach estimates a flux between the two domains. Overland flow in the surface domain applies the diffusion-wave equation:

$$\frac{\partial (d_o + z)}{\partial t} = \nabla \cdot (\mathbf{K_o} \cdot \nabla(d_o + z)) - d_o \Gamma + Q \tag{3.2}$$

which assumes mild slopes, depth integrated velocities, hydrostatic pressure, and neglects inertial effects. The surface hydraulic conductivity $\mathbf{K_o}$ is approximated as a function of depth, d_o, by the Manning, Chezy, or Darcy-Weisbach equations.

HGS implements a process-based framework to calculate evapotranspiration (ET) based on the soil saturation, potential evapotranspiration (PET), soil type and vegetation parameters. ET processes are an implicit component of HGS' flow simulation and are simultaneously solved within the flow solution. Actual evapotranspiration (AET) in HGS is comprised of three components (canopy evaporation E_{can}, transpiration T_p, and evaporation E_s):

$$AET = E_{can} + T_p + E_s \tag{3.3}$$

where each component is always greater than or equal to zero and the sum of the components can never exceed the PET. The transpiration and evaporation functions are implemented as:

$$T_p = f_1(LAI)f_2(S)RDF[PET - E_{can}] \tag{3.4}$$

$$E_s = \alpha^*(PET - E_{can} - T_p)EDF \tag{3.5}$$

where LAI is the leaf area index, S is the soil moisture content, RDF is the root density function, EDF is the energy density function, and f_1, f_2, and α^* are fitting functions.

3.2 Weather Research and Forecasting

The Weather Research and Forecasting (WRF) Model is a non-hydrostatic mesoscale finite difference atmospheric model. The WRF modeling suite hosts two separate dynamical cores (for the purpose of this study we used only the Advanced Research WRF (ARW) core), data assimilation, advanced physics based parameterization, numerous radiative schemes, and multiple land surface models. The WRF model implements the terrain following flux-based Euler equations solved by the third-order Runge-Kutta temporal discretization with a second-order split-time acoustic wave. A detailed description of WRF's development can be found in the NCAR Technical Note, *A Description of the Advanced Research WRF Version 3* (*Skamarock et al.*, 2008).

The Noah LSM is one of the most popular land surface schemes in the WRF model. It simplifies the near surface as a shallow 2 m thick one-dimensional column and incorporates vadose zone hydrology and heat transport. The subsurface domain is modeled with four vertical layers that range between 10 to 100 cm thick. The benefits of using the Noah LSM coupled to WRF are that it includes vadose zone hydrology, subsurface heat transport, plant physics, and it is computationally efficient and easy to use. However, the Noah LSM fails to include three-dimensional subsurface flow, surface water flow, and saturated groundwater flow.

3.3 Coupling Method

3.3.1 Spatial Coupling

Atmospheric and hydrologic models are inherently different because of their drastically contrasting fluid properties, physical equations, time-scales, and geometrical arrangement. HydroGeoSphere a temporally implicit model, implements three types of meshing algorithms: a finite difference hexahedra (8-point elements), finite element triangular prisms

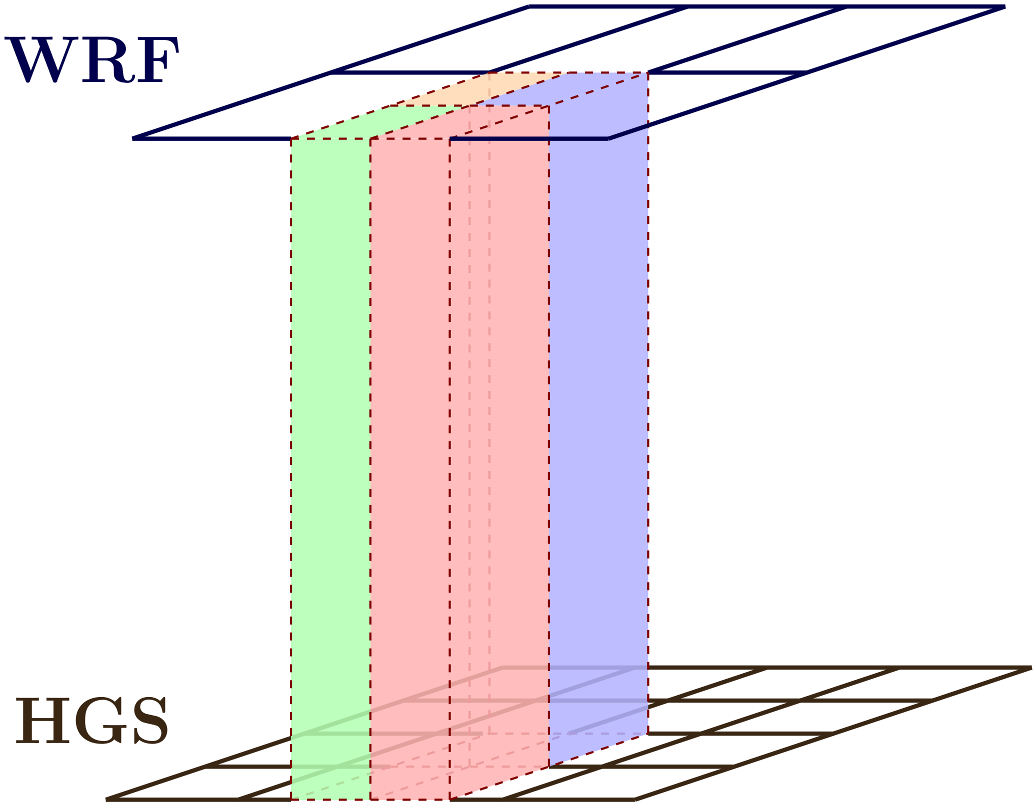

Figure 3.1: Coupled linking between the HGS and WRF models.

(6-point elements), or finite element tetrahedra (4-point elements). However WRF, a temporally explicit model, only employs a regular finite difference hexahedral elemental mesh. Linking HGS to WRF required the development of a custom coupling framework that independently correlates the communication of information between the two model's unique meshes.

The HGS-WRF coupling framework allows for independent model meshing and projection characteristics by comparing the geographic coordinates (i.e., latitude and longitude) between the two domains. Our coupling method, shown in Figure 3.1, handles overlapping grid cells by computing the spatially-weighted area-based arithmetic mean, which maintains energy and mass conservation. For instance, the HGS model may implement an Albers projection with a horizontal discretization of 4 km, while the WRF simulation will use the Lambert conformal projection with a 10 km discretization.

Initially, the WRF model internally calculates the potential evapotranspiration (PET) and precipitation (I) rates and passes them to HGS:

$$PET_{hgs_j} = \frac{\sum_i^n A_i \cdot PET_{wrf_i}}{\sum_i^n A_i} \tag{3.6}$$

$$I_{hgs_j} = \frac{\sum_i^n A_i \cdot I_{wrf_i}}{\sum_i^n A_i} \tag{3.7}$$

where A is the overlapping elemental or cell area, and the subscripts wrf_i and hgs_j are the indices for Weather Research and Forecasting and HydroGeoSphere, respectively. After calculating the fluxes from WRF to HGS, our modeling framework passes HGS' actual evapotranspiration and soil saturation back to the WRF model:

$$
\begin{aligned}
S_{wrf_i} &= \frac{\sum_j^n A_j \cdot S_{hgs_j}}{\sum_j^n A_j} && (3.8)\\
AET_{wrf_i} &= \frac{\sum_j^n A_j \cdot AET_{hgs_j}}{\sum_j^n A_j} && (3.9)
\end{aligned}
$$

where S is the soil water saturation and AET is the actual evapotranspiration. The current numerical implementation of HGS-WRF is for finite difference meshes, as shown in Figure 3.1. However, since HGS can also use unstructured element meshes (e.g. prisms or tetrahedra), Equations 3.6-3.9 can be readily adapted for the finite element method.

Hydrogeologic models typically use basin divide boundaries, which eliminates interflow from upstream catchments. The only water fluxes left are flows out of the basin and exchanges between the atmosphere via precipitation and evapotranspiration. Atmospheric models, on the other hand, implement rectangular domains that overlap multiple basins, water bodies, and political boundaries. Combining the two models together, required a domain splitting algorithm that allows for separate boundaries for each individual model. The smaller HGS domain is a subset of the larger WRF simulation. Inside of the WRF model, the HGS portion overrides the internal LSM with HGS' soil saturation and evapotranspiration. However, outside of the HGS portion, the WRF model uses its own land surface scheme (Noah LSM).

Furthermore, to aid with the linkage between models, HGS implements the same near surface layering used in the Noah LSM. In both models the first, second, third, and fourth layers are 10, 30, 60, and 100 cm thick, respectively. The fourth layer in the Noah model is the last layer, while the HGS model further discretizes the subsurface deeper than these four layers. As described earlier, HGS passes its soil saturation values to Noah and overwrites the values per layer.

3.3.2 Temporal Coupling

Integrated hydrology traditionally has slow long-term problems, with time scales ranging from hourly (surface water) to millennial processes (groundwater flow). In contrast atmospheric physics have much faster time scales and require small time steps (seconds to minutes) to capture acoustic waves, radiative energy, and convective flow; for example WRF recommends 6 second global time steps per kilometer of horizontal resolution (e.g. a WRF simulation with a grid spacing of 10 km would use a 60 second time step). Combining atmospheric and hydrologic models together creates a major time scale problem that must be resolved.

The simplest temporal coupling method is to run both models at the same time step and directly exchange boundary information between the models at every time step. However, running both models at the same time step results in wasted computational resources, because the hydrological model's moisture balance does not rapidly change over the course of seconds. For this reason, we implemented a sub-time stepping routine such that the atmospheric model can run at a much smaller time step, while the hydrological model runs a coarser temporal resolution. This assumption is acceptable because WRF's radiative energy balance routine does not run every time step; the recommended WRF radiative time step is 10 times the global time step. This means that the potential evapotranspiration, a component of the radiative energy balance, is only updated during the larger time steps.

Our explicit temporal method, shown in Figure 3.2, remains first-order accurate which requires small time steps to resolve the diurnal PET forcing. HGS passes saturation and actual evapotranspiration fluxes to WRF. Meanwhile WRF transfers its potential evapotranspiration and precipitation fluxes to HGS.

Modified Coupling

The HGS-WRF coupling package can also run in a modified coupling case, such that the WRF model internally calculates the actual evapotranspiration, shown in Figure 3.3. WRF then provides the net precipitation rate, which is defined as the precipitation minus actual evapotranspiration, to HGS. The HGS model now can calculate its internal water balance, using the Newton-Raphson solver, and send its saturation values back to WRF.

This method drastically speeds up the simulation times for the HGS-WRF model, because the requirement to pass information between the two models can be delayed to several hours. The net precipitation rate (precipitation - ET) outputted from the WRF simulation, will often have negative values, since ET fluxes diurnally cycle throughout the day and precipitation is only an intermittent process. This net precipitation rate is then inputed into HGS as a top boundary condition. However, this method imposes several real limitations, especially in regions with low precipitation, high ET, and low soil moisture.

For instance, if the WRF simulation internally calculates large evapotranspiration fluxes over a dry soil region within HGS, then the HGS model will not be able to supply this flux; creating large mass balance errors. Eventually, the HGS near surface soils will reach residual saturation (during drought periods), which creates zones with extremely low hydraulic conductivity (hydraulic conductivity is a function of soil saturation). Correspondingly,

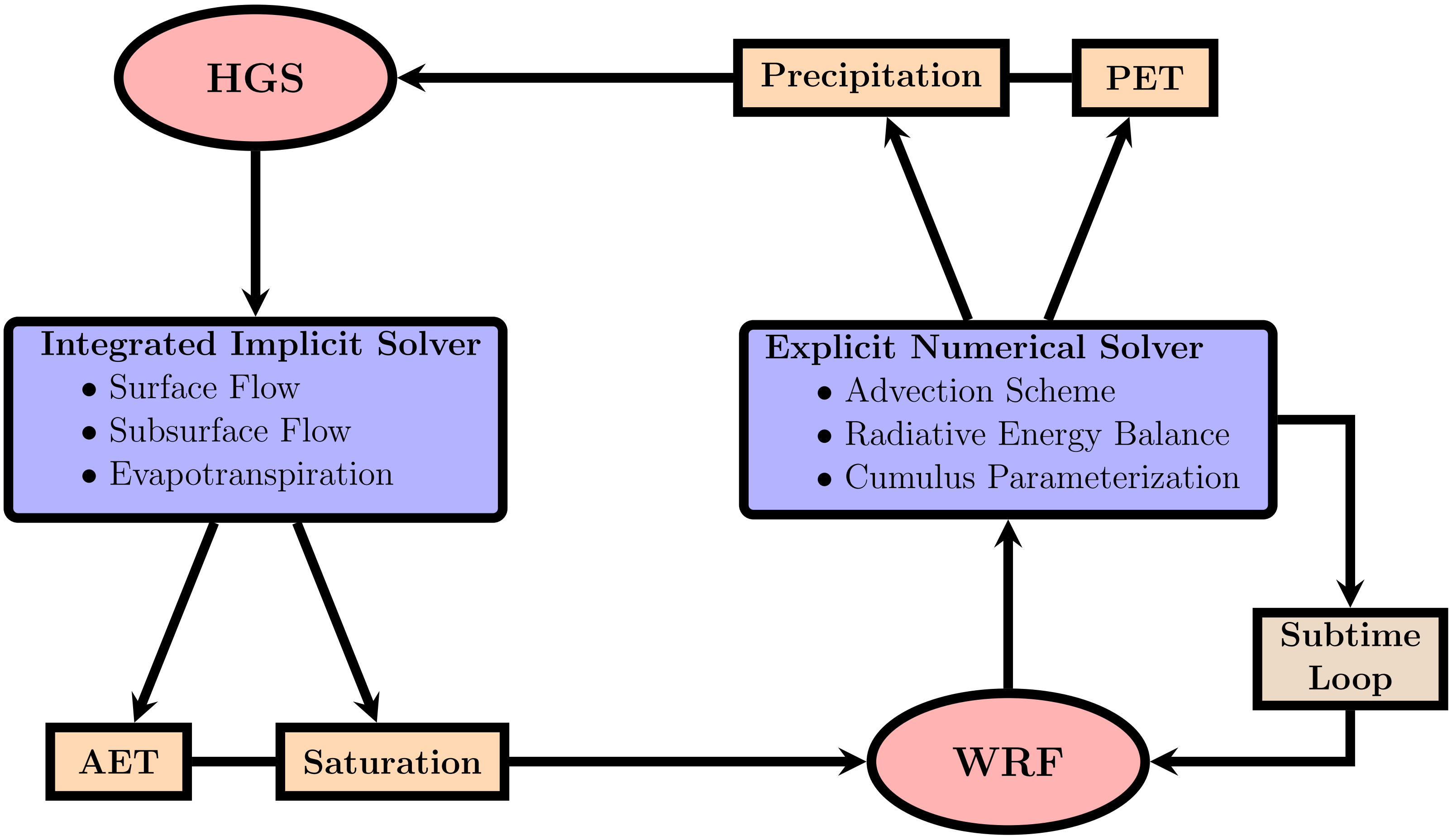

Figure 3.2: HGS-WRF coupling schematic. HGS passes the saturation and actual evapotranspiration to WRF. WRF passes the precipitation and potential evapotranspiration fluxes to HGS.

WRF's internal ET calculator will continue to maintain high ET fluxes, even when the soil saturations are at residual values for HGS.

The modified HGS-WRF coupling scheme is not the most accurate method available and will artificially remove water from the domain. For this reason, the traditional HGS-WRF scheme is the best method for coupled simulation because it minimize error within the mass balance and thus is used herein.

3.4 Parallelization

Both the HGS and WRF models are extremely complex software packages that are implemented with advanced numerical solvers. HydroGeoSphere implements a shared memory OpenMP approach, and is optimized for multi-core workstations (*Hwang et al.*, 2014). The HGS parallelization efforts were focused on optimizing the matrix construction and solver, while minimizing error between serial and parallel solutions (difference in head between solution is less than 10^{-3} m). In contrast, WRF has multiple parallel choices including OpenMP, MPI (a distributed memory algorithm better suited for multi-processor cluster computing), and a hybrid OpenMP + MPI option (for shared and distributed memory).

Ensuring parallelization in HGS-WRF is not a luxury, but rather a requirement to efficiently solve complicated problems. Our method, which passes data between the two models, implements a quasi-parallel scheme. Each model is running as a standalone parallel process, that alternate compute cycles. Initially, the WRF model will compute the PET and precipitation fluxes and pass them to HGS. Once WRF outputs these fluxes, the WRF simulation is placed on pause until HGS computes the AET and saturation values.

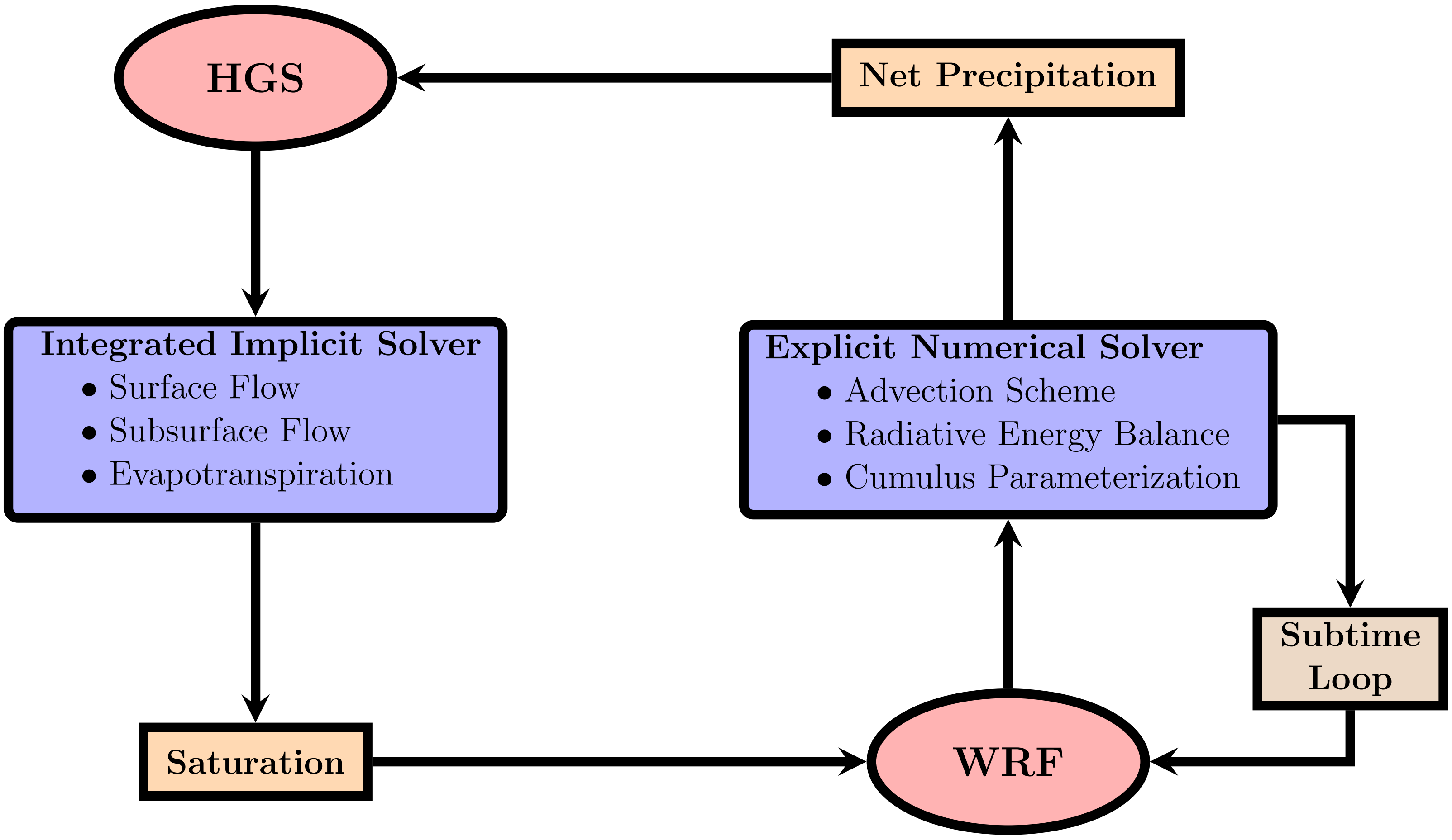

Figure 3.3: Modified HGS-WRF model coupling. WRF outputs net precipitation to HGS and HGS outputs saturation to WRF.

After HGS outputs its values to WRF, the HGS simulation is placed on pause. This cycle continues till the end of the numerical simulation. Currently the parallelization is written for both models to only run OpenMP, but several simple additions to the parallelization routine could allow the HGS-WRF model to be extended to a hybrid scheme, where HGS uses OpenMP and WRF implements OpenMP + MPI.

3.5 Advantages over previous models

There have been several studies that have successfully coupled groundwater flow to atmospheric models, and each of these previous coupling methods have had serious limitations. Currently, all coupled models require that the groundwater flow component be included over the entire land surface domain of the atmospheric model. The required atmospheric domain is much larger than the domain of interest of the hydrological model, due to the obligation of having the atmospheric boundaries much farther away than the domain of interest (to eliminate influence from the model boundary). In some cases, as with the 2-D Noah Distributed groundwater model (*Gochis and Chen*, 2003), including the coupled groundwater flow simulation over the entire atmospheric domain is acceptable because the addition of groundwater flow is such a small component of the simulation. Nonetheless, more comprehensive 3-D surface/subsurface models such as ParFlow still require the surface/subsurface domains to cover the complete atmospheric domain, which may cost additional computational resources and requires significantly more effort to construct the large-scale basin model.

The next main limitation that other coupling methods have is their reliance on the land surface model for calculating actual evapotranspiration. The previous methods export the near surface soil moisture values (typically the first 2 meters) to the atmospheric model, then the atmospheric model's land surface routine internally calculates the evapotranspiration. Here lies the problem. Root zones often extend past the shallow subsurface of just 2 meters, and well draining sandy-soils with shallow water tables may have dry near-surface conditions limiting actual evapotranspiration, in zones where high ET legitimately occurs.

The simplest method to couple atmospheric and hydrological models is to directly overlay the meshing so that each model's node overlaps. In this method, no mass/energy interpolation is calculated between domains, thus simplifying continuity conditions. However, this assumption forces the atmospheric model to run at the same grid spacing as the hydrological model. Depending on the system, either the atmospheric model will require an excessively tight model mesh (extra computational expense) or the hydrological model will be overly coarse (not properly resolving the physical problem). In our coupling method, we implemented a custom domain splitting framework such that each model utilizes it's own separate model mesh. This allows the hydrological and atmospheric models to use separate projection methods, different mesh resolutions, and independent numerical methods (i.e. finite difference or finite element).

An additional benefit of using independent model meshes is that our method can take existing HGS and WRF models that have been calibrated and tuned, and then they can be quickly coupled by running the HGS-WRF code. Integrated basin-scale modeling is an extremely time intensive process, which can require months to develop a well tuned model.

3.6 Example Simulation

In the following chapter, we simulate HGS-WRF over the entire state of California. Chapter 4 includes the development of the HGS and WRF models for the California Basin. After spinning up the hydrological model from predevelopment to current day conditions, the HGS-WRF model was implemented for the year 2011. The California Basin model simulations demonstrate the capabilities of the HGS-WRF simulator. The model results capture both the weather and climate trends within the state. However, the model lacks several key features like winter processes, hydraulic control structures, and crop irrigation.

Chapter 4

California Model

4.1 Introduction

Water resources are fundamentally a transboundary issue; groundwater and surface water continuously flow between neighboring states regardless of international treaties or interstate compacts. Adjoining nations and regions regularly negotiate fair water use agreements based on population, agriculture, and industrial demands. However, governments often fail to establish minimal base flow guidelines, resulting in decreased ecosystem health (*Gleick*, 1998). Furthermore, water agreements often disregard the fundamental connection between groundwater and surface water, ignore the significant temporal variability in precipitation fluxes, and avoid the non-stationarity of climate change. Quantifiable analysis of water resources is critically important when considering domestic policies and agreements regarding agricultural, industry, and the environment. For instance, California has allowed farmers unrestricted access to groundwater resources. This lack of regulation has resulted in dire environmental impacts, including extreme land subsidence (2 inches per month), decreased surface water storage (8.1 km^3), and diminished agricultural yields ($2.2 billion) (*Mann and Gleick*, 2015; *Farr et al.*, 2015; *Howitt et al.*, 2014) and has significant impact on interstate and US-Mexico transboundary water agreements.

Current climate models coupled to land surface models (LSM) are often utilized to predict the risks to water resources. Typically, LSMs are one-dimensional vertical columns that include shallow vertical subsurface flow, biogeophysics, heat transport, and snow processes. However, LSMs lack physics-based lateral surface/subsurface water flow, groundwater storage, and the critical feedbacks between surface and subsurface hydrology (*Davison et al.*, 2015).

To overcome these limitations, land-surface scheme modelers have replaced their simple one-dimensional hydrological models with more advanced water balance approaches, although even these remain constrained by limitations. For example, the Weather Research and Forecasting (WRF) Model, a 3-D mesoscale nonhydrostatic atmospheric model, has been coupled to several groundwater flow models, including Noah Disturbed, a 2-D Boussinesq groundwater flow model (*Gochis and Chen*, 2003), which fails when groundwater tables are steep (e.g. near pumping wells or around mountainous topography). In a separate study, WRF was coupled to Parflow, a 3-D finite difference surface/subsurface flow model (*Maxwell et al.*, 2011). However, Parflow relies on the Noah LSM for evapotranspiration process, which limits root-zones to a maximum depth of two meters.

4.1.1 Previous California Models

California's water resource system relies on a vastly interconnected network of groundwater, surface water, snow melt, and interbasin transfers. The California state government has conventionally viewed each hydrologic component as an independent element, ignoring the vital fluxes between domains. Furthermore, this confined view of water resources has resulted in a proliferation of new models that only analyze a single part or region of the water cycle.

Currently, the only model that simulates the entire California basin is the California Basin Characterization Model (CA-BCM) (*Flint et al.*, 2013). The Basin Characterization Model is a distributed-parameter water-balance model that accounts for evapotranspiration, runoff, groundwater recharge and several other processes, as shown in Figure 4.1. The

CA-BCM model is discretized on a 270 m grid and runs a monthly time step. However, the CA-BCM does not implement physics-based equations (e.g. Richards' equation, diffusive wave equation, and heat transport equation) and relies on a simplified mass balance, shown as:

$$AW = P + S_w - PET - S_a + S_s \tag{4.1}$$

where AW is the available water, P is the precipitation, S_w is snow melt, PET is potential evapotranspiration, S_a is snow accumulation, and S_s is stored surface water.

Additional large-scale research studies modeling California have focused on simulating particular regions within the basin. These attempts include: the Central Valley Hydrologic Model (CVHM) with MODFLOW Farm Processes; San Joaquin Valley (SJV) model with HydroGeoSphere; and San Joaquin Basin Model (SJBM) with ParFlow (*Faunt*, 2009; *Bolger et al.*, 2011; *Gilbert and Maxwell*, 2014). These three domains are shown in Figure 4.2. The CVHM implements the Farm Processes package, which adds transpiration and infiltration processes to the traditional finite difference MODFLOW-2000 groundwater-only flow model. The model simulates the entire Central Valley (52,000 km^2) at a 1.6 km horizontal resolution, with 10 vertical layers ranging from 15 to 550 m thick. The groundwater system was initialized with historical water table elevations, and was simulated from 1961 to 2003 (42.5 years) (*Faunt*, 2009).

The San Joaquin Valley (SJV) model was designed as a pre-development hydrological simulation. The SJV was implemented with the control-volume finite element HGS model and covers a 17,232 km^2 area, with 11 vertical layers and a horizontal discretization ranging between 60 and 3,000 m. The model was run to steady-state conditions, and it implements

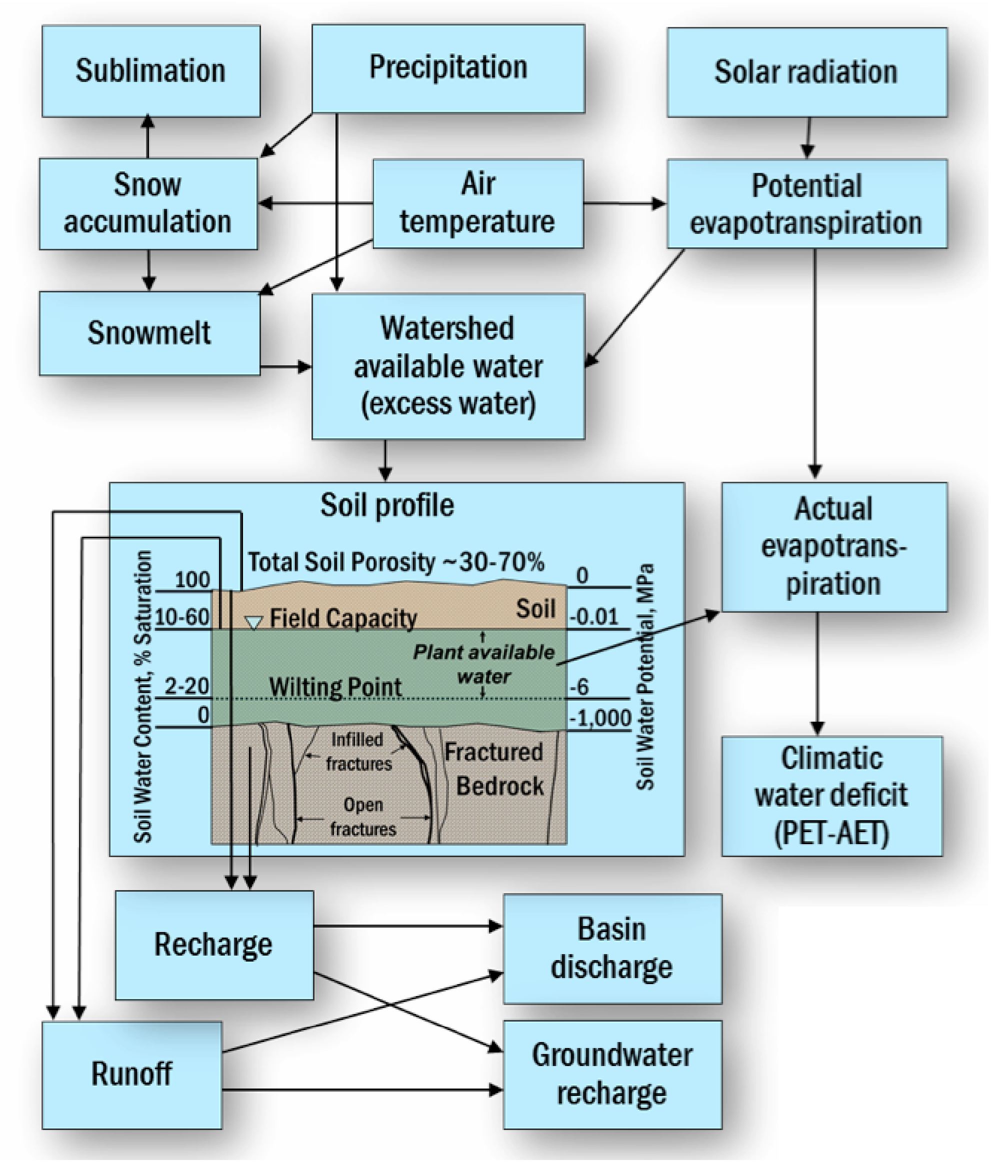

Figure 4.1: The California Basin Characterization Model (CA-BCM) schematic of water processes (*Flint et al.*, 2013).

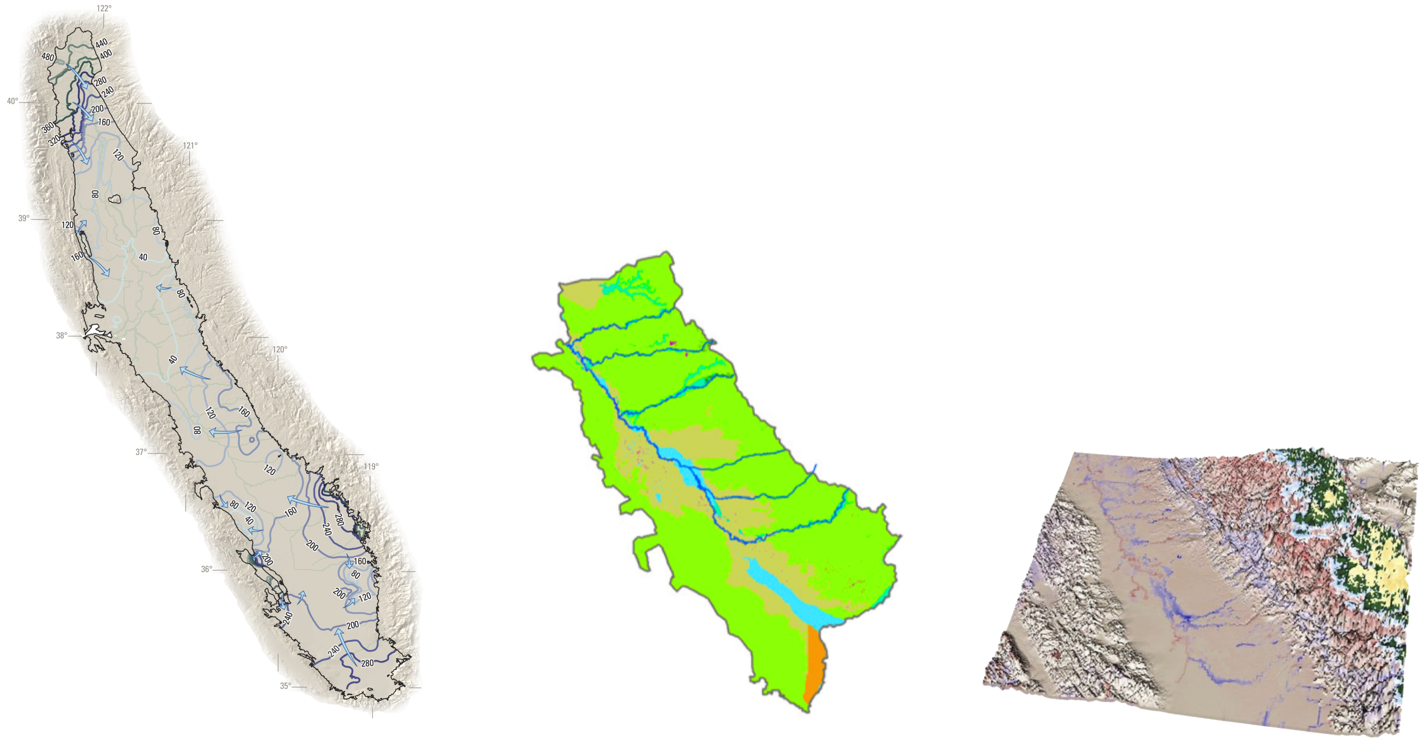

(a) CVHM with MODFLOW (b) SJV model with HGS (c) SJBM with ParFlow

Figure 4.2: Previous physics-based California models (*Faunt*, 2009; *Bolger et al.*, 2011; *Gilbert and Maxwell*, 2014).

historically averaged (1870-1884 AD) streamflow, precipitation, and evapotranspiration rates for its surface boundary conditions. Also, the subsurface portion of the domain has a zero-flux boundary condition along the bottom and sides (*Bolger et al.*, 2011).

The latest large-scale hydrological model simulating a substantial region of California is the San Joaquin Basin Model (SJBM) performed with ParFlow. The rectangular domain covers 59,400 km^2 area at a 1 km horizontal resolution and includes a portion of the Southern Coastal Range, San Joaquin Valley, and Sierra Nevada mountains. Initially the model was spun-up with the coupled ParFlow-Community Land Model (CLM) code which adds near-surface moisture and energy balance calculations to the standalone ParFlow mode (*Gilbert and Maxwell*, 2014). Additionally, the SJBM model was simulated with the ParFlow-WRF model at a high resolution of 1 km (*Gilbert et al.*, 2015).

Although these three models cover vast regions of California (17,232 - 59,400 km^2), they only account for a small portion of the entire 410,000 km^2 California Basin domain (4-15%). The only model that captures the entire basin is the highly parameterized CA-BCM simulations.

4.2 California Basin Model

4.2.1 Geological Model

In an effort to improve upon previous water resource simulations of California and to demonstrate the utility of HGS-WRF, the California Basin Model was created, which incorporates large-scale geologic datasets (e.g. topography, soil stratigraphy, land use and geologic formation), consumptive water use, precipitation, and potential evapotranspiration into one modeling platform. When creating a hydrological model, the first important task is to define the exterior region of the watershed by selecting the hydrologic divides that serve as the perimeter of the watershed. Conveniently, the USGS created a system of hydrological units that delineates each watershed as a Hydrologic Unit Code (HUC), shown in Figure 4.3. The California Basin is the 18th regional watershed, extends over a 410,000 km^2 area, and covers the majority of the state of California, southern Oregon, western Nevada, and a small region of north western Mexico (*Seaber et al.*, 1987).

After establishing the domain boundary, the USGS HYDRO1k topographic dataset, a hydrologically corrected digital elevation model (DEM) at a one kilometer resolution, was applied to the model creating the top surface elevations (*U.S. Geological Survey*, 2015b). Because HYDRO1k is provided in the Lambert Azimuthal Equal Area coordinate system, the DEM was converted and reprojected to the hydrological model's Albers projection coordinate system (coordinate system values Table 4.1). Next, the DEM files were upscaled from the native 1 km resolution to the more coarse 4 km model mesh. In the last step, the major rivers were burned into the surface topography. This step is critical because it maintains a monotonic flow path along riverbeds and prevents undesirable surface water ponding. The completed DEM for the California Basin Model is shown in Figure 4.4.

After defining the topography and model boundary, the three-dimensional hydrogeological model was then constructed. The bottom of the domain consists of a flat continuous surface at a constant 6,000 m below sea level. This deep hydrologic system is necessary to capture the thick sediments found in the Central Valley. The next layer defined was the bedrock unit; this layer was approximated by subtracting the sediment thickness layer

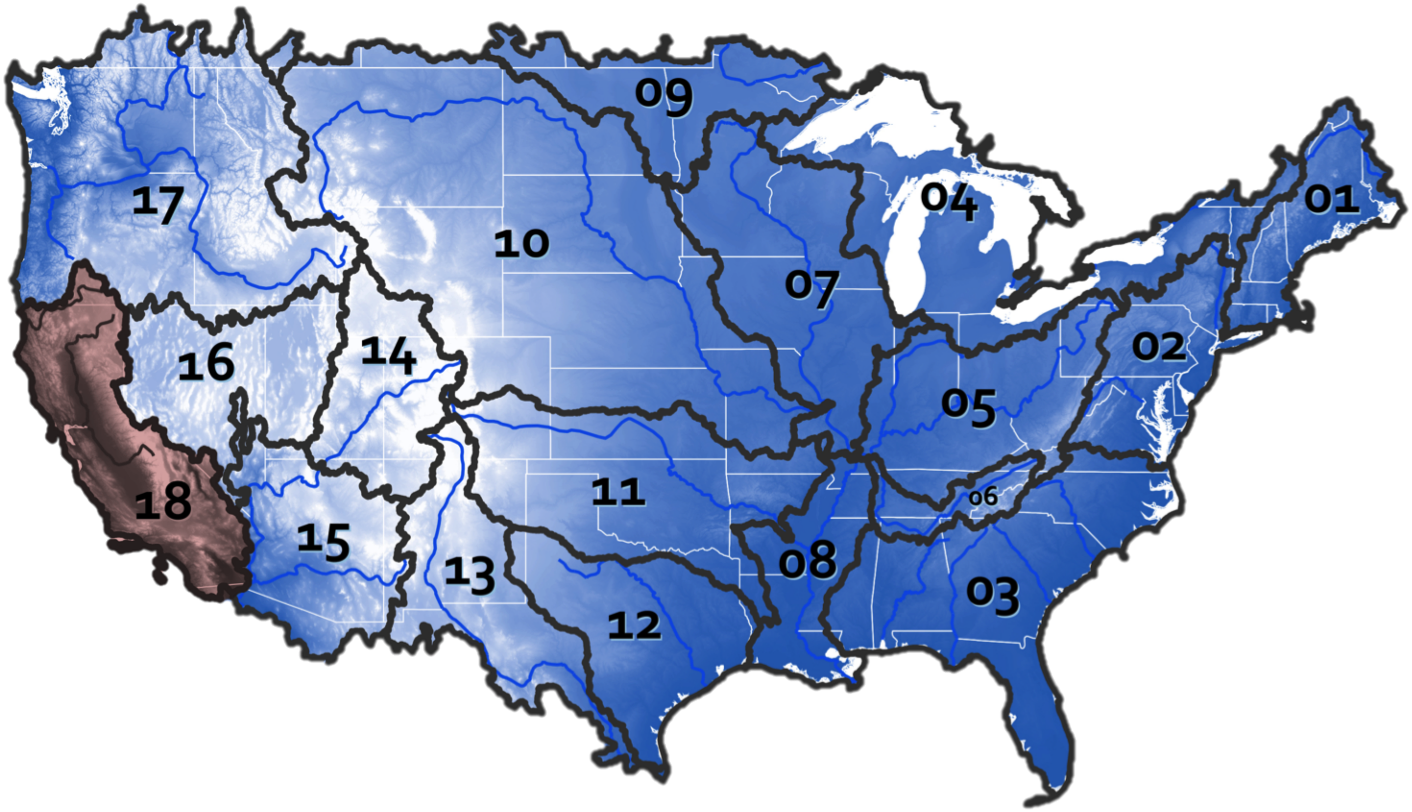

Figure 4.3: USGS Hydrologic Unit Code (HUC) map for the United States. The California Basin region 18 is shown in red. Figure modified from *Long* (2016).

from the topographic elevations (*Laske and Masters*, 1997). The bedrock system was approximated as a homogenous unit with a low hydraulic conductivity and subdivided into three discrete layers. Each sediment layer was then characterized by soil texture, Table 4.2 from the Digital General Soil Map of the United States STATSGO2 dataset, shown in Figure 4.5 (*Soil Survey Staff*, 2015).

The HGS simulation was discretized at a 4km horizontal resolution using a finite difference mesh, an option within HGS, as shown in Figure 4.6. The first four near-surface layers are the thinnest layers and are set at 0.1, 0.3, 0.6, and 1.0 m thickness (for layers 1-4), which is the same discretization used in the Noah LSM. The next ten layers are significantly coarser, with the 5th layer at 3.0 m thick, layers 6-8 are 65 m thick each, and layers 9-11 vary in thickness based on the soil sediment depths. The last three layers (12-14) equally span across the bedrock unit.

4.2.2 Boundary Conditions

Our geological model correctly delineates the California Basin along its groundwater divides. Therefore, the zero-flow boundary condition is the most appropriate boundary for the horizontal sides of the model. Additionally, the bottom of the model utilizes a no flow boundary because vertical flow in the deep subsurface is assumed to be negligible. Meanwhile, the top of the subsurface domain directly interacts with the surface domain by implementing HGS' dual node coupling approach.

The tight coupling of HGS' surface and subsurface domains supports precipitation and surface water infiltrating in the uplands, which recharges the aquifer and creates ground-

Figure 4.4: Topographic relief map for the California Basin Model.

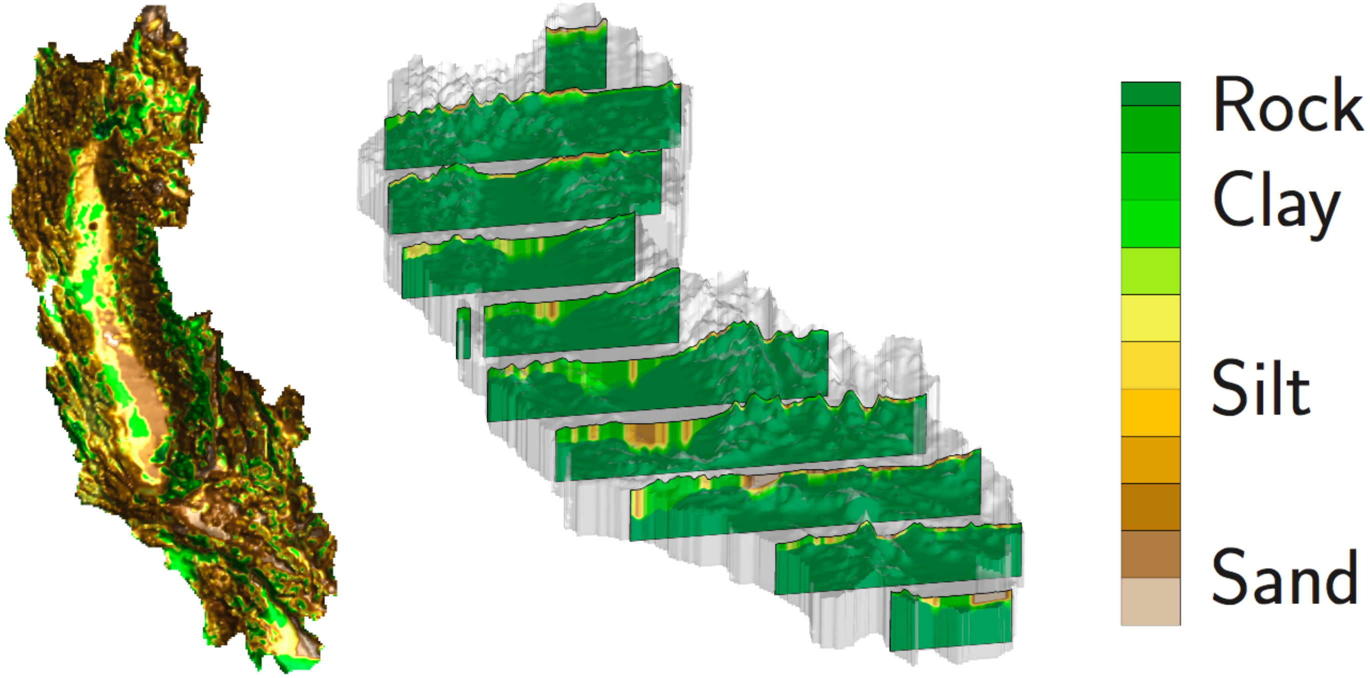

Figure 4.5: Three-dimensional California geological model.

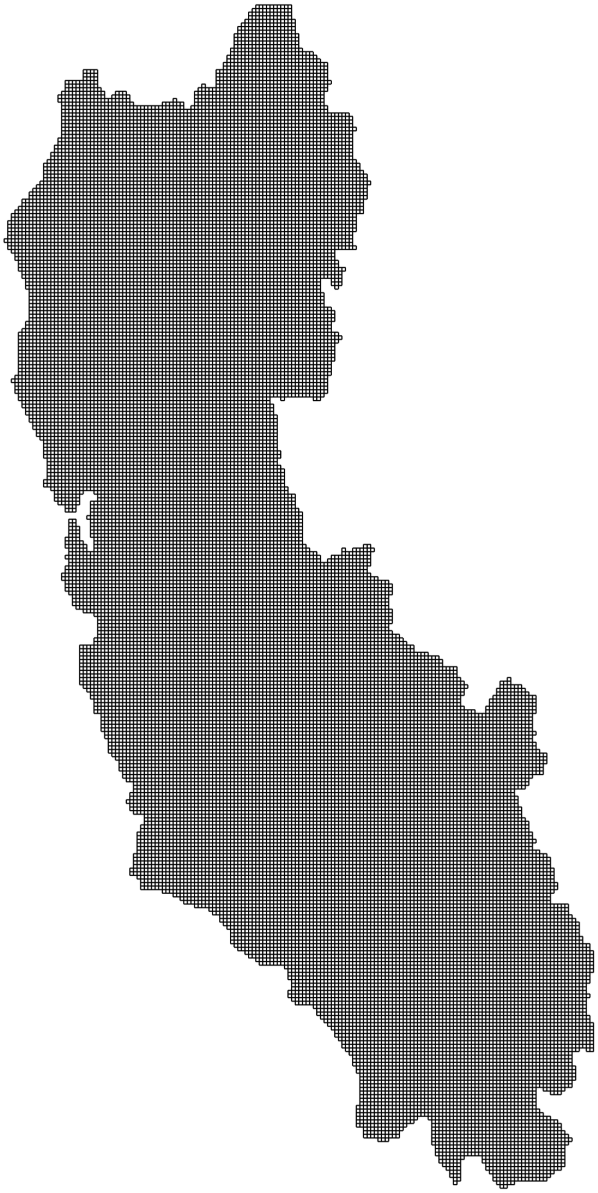

Figure 4.6: California Basin Model 4 km resolution discretization.

water flow towards the lowlands. This groundwater exfiltrates from the subsurface and creates low lying lakes and provides baseflow for the regional rivers. Once surface water reaches the lateral boundary of the domain, the surface domain implements the critical depth boundary condition, which allows water to freely exit the domain and into the Pacific Ocean.

Precipitation and potential evapotranspiration patterns are the predominant control for water distribution throughout the domain. Northern California receives drastically more precipitation and has lower PET fluxes than southern California. For this reason, the northern region of California has more water—higher soil saturations, shallower groundwater tables, and more powerful rivers—than southern California. To spin-up the model, we used CMIP5 30-year (1980-2010) ensemble average precipitation and PET data provided by Climate Commons California Landscape Conservation Cooperative (*Climate Commons*, 2015), shown in Figure 4.7 and 4.8.

Once the model reached steady-state, current groundwater and surface water extractions were turned on, and the HGS model was run from pre-development to present-day conditions. No transient water use data is presently available for the California Basin. For this reason, the 2010 water use data was used for the entire simulation, which is provided by the USGS and is defined by each county (*U.S. Geological Survey*, 2015a). In order to avoid any local cones of depression, we implemented a high-resolution network of pumping centers (nearly 20,000 wells), shown in Table 4.3-4.5.

Table 4.1: Albers Projection for HGS model.

ϕ_1	Standard Parallel 1	29.5
ϕ_2	Standard Parallel 2	45.5
ϕ_o	Reference Latitude	23.0
λ_o	Reference Longitude	-96.0

Table 4.2: Soil texture hydraulic properties with van Genuchten parameters.

Soil Type	K_x (m/s)	η	S_s (1/m)	α	γ
Sand	2.92E-3	0.437	1.0E-4	0.74	0.66
Loamy Sand	8.50E-4	0.350	1.0E-4	0.80	0.42
Sandy Loam	3.60E-4	0.453	1.0E-4	2.85	0.42
Loam	1.84E-4	0.464	1.0E-4	1.03	0.21
Silt Loam	9.45E-5	0.501	1.0E-4	0.565	0.16
Silt	9.45E-5	0.501	1.0E-4	0.565	0.16
Sandy Clay Loam	1.19E-5	0.397	1.0E-3	0.275	0.26
Clay Loam	3.20E-5	0.464	1.0E-3	0.29	0.22
Silty Clay Loam	2.09E-5	0.471	1.0E-3	0.50	0.21
Sandy Clay	1.67E-5	0.43	1.0E-3	0.34	0.21
Silty Clay	1.25E-5	0.479	1.0E-3	0.34	0.21
Clay	8.35E-6	0.475	1.0E-3	0.34	0.09
Unconsolidated Rock	1.0E-5	0.10	1.0E-5	0.74	0.66
Consolidated Rock	2.5E-6	0.05	1.0E-5	0.74	0.66

Table 4.3: California 2010 water use by county (*U.S. Geological Survey*, 2015a).

County	Fresh Water Use (m^3/s)	# of Wells	Area (km^2)
Alameda	11.02	125	1,911
Alpine	0.20	5	1,914
Amador	1.42	219	1,570
Butte	31.33	175	4,248
Calaveras	1.02	150	2,642
Colusa	36.58	200	2,981
Contra Costa	11.07	153	1,865
Del Norte	0.60	61	2,611
El Dorado	2.44	159	4,434
Fresno	122.95	925	15,444
Glenn	27.57	225	3,406
Humboldt	2.53	386	9,254
Imperial	4.47	289	10,813
Inyo	51.23	984	26,397
Kern	90.76	1125	21,088
Kings	56.91	125	3,600
Lake	1.92	325	3,258
Lassen	8.87	556	11,805
Los Angeles	70.42	505	10,515

Table 4.4: California 2010 water use by county (*U.S. Geological Survey*, 2015a).

County	Fresh Water Use (m^3/s)	# of Wells	Area (km^2)
Madera	32.80	350	5,537
Marin	1.88	57	1,347
Mariposa	0.23	321	3,758
Mendocino	3.57	248	9,088
Merced	65.47	325	4,996
Modoc	11.46	526	10,215
Mono	10.06	167	7,884
Monterey	23.39	387	8,604
Napa	4.24	150	1,953
Nevada	2.12	100	2,481
Orange	23.80	100	2,046
Placer	8.38	257	3,893
Plumas	5.29	300	6,615
Riverside	46.40	1144	18,669
Sacramento	29.83	150	2,502
San Benito	3.73	200	3,597
San Bernardino	28.01	1719	51,960
San Diego	29.27	302	10,888
San Joaquin	76.76	225	3,623

Table 4.5: California 2010 water use by county (*U.S. Geological Survey*, 2015a).

County	Fresh Water Use (m^3/s)	# of Wells	Area (km^2)
San Luis Obispo	9.25	544	8,557
San Mateo	4.07	54	1,163
Santa Barbara	11.33	384	7,091
Santa Clara	13.05	175	3,344
Santa Cruz	2.91	55	1,155
Shasta	10.46	550	9,806
Sierra	1.71	295	2,468
Siskiyou	18.01	894	16,283
Solano	19.83	125	2,145
Sonoma	9.97	291	4,082
Stanislaus	71.96	225	3,872
Sutter	31.62	125	1,562
Tehama	36.16	475	7,643
Trinity	0.98	550	8,234
Tulare	113.93	600	12,494
Tuolumne	1.57	244	5,791
Ventura	18.00	277	4,781
Yolo	34.18	125	2,621
Yuba	11.28	150	1,632

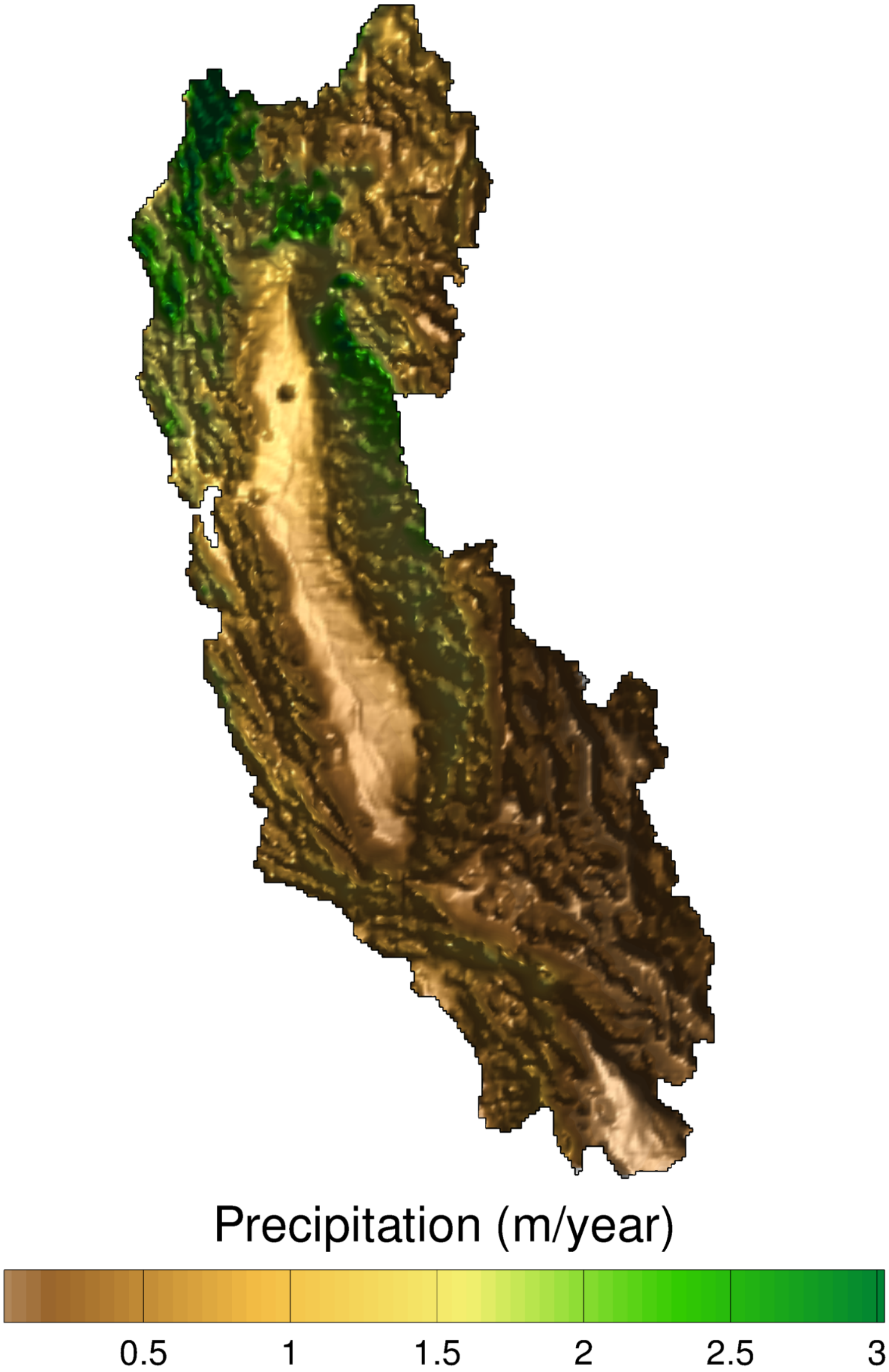

Figure 4.7: California 30 year average (1980-2010) precipitation data shown in meters per year.

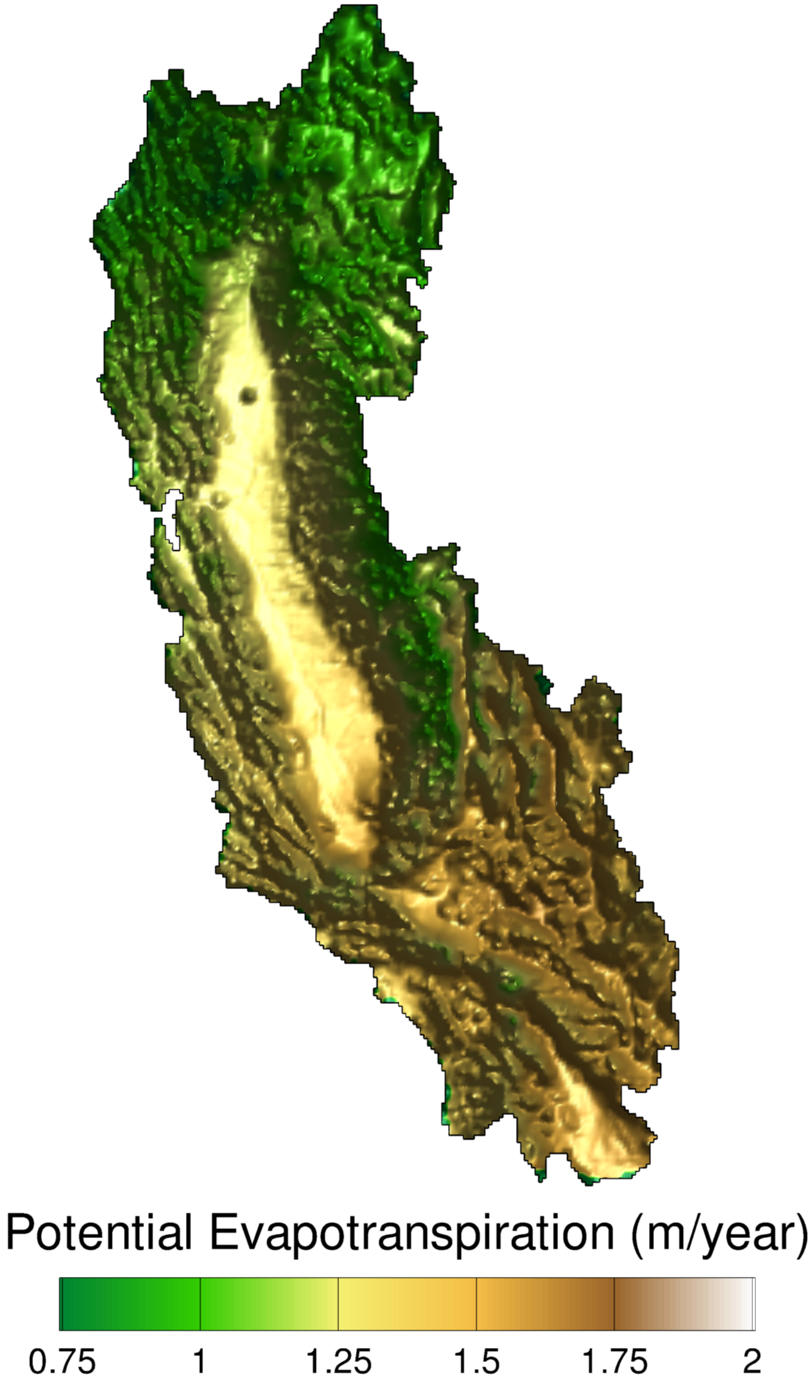

Figure 4.8: California 30 year average (1980-2010) potential evapotranspiration data shown in meters per year.

4.3 Atmospheric Model

The WRF model requires extensive input, parametrization, and data. Inside of the WRF model, each physical component (e.g. radiative, cumulus, land surface, planetary boundary layer) has several to tens of options to optimize the simulation based on domain location, discretization, and the research questions. One of the first of many steps is to select the simulation domain for the atmospheric model. In the case of our coupled simulation, the WRF domain was centered around the HGS California Basin model, shown in Figure 4.9. The WRF model was discretized to a horizontal resolution of 12 km and 42 vertical layers (2.8 million nodes). Temporally, the WRF simulation runs at a 50 second time step and the radiative scheme runs every 10 minutes.

Once the domain and discretization is selected, the next phase is to download GCM data sets that cover the entire simulation domain. For lateral boundary conditions, we implemented the ERA-Interim six-hour global reanalysis data set provided by the European Centre for Medium-Range Weather Forecasts (ECMWF) (*Berrisford et al.*, 2011). The global data sets were then processed for all of 2011 using the WPS (WRF Preprocessing System). Lastly, the WRF model physics parameterization were selected as the following:

Radiation – Community Atmosphere Model (CAM 3.0)
Planetary Boundary Layer – Mellor-Yamada-Janjic (MYJ)
Cumulus Parameterization – Kain-Fritsch
Microphysics – New Thompson
Land Surface Model – Noah LSM
Hydrological Model – HydroGeoSphere

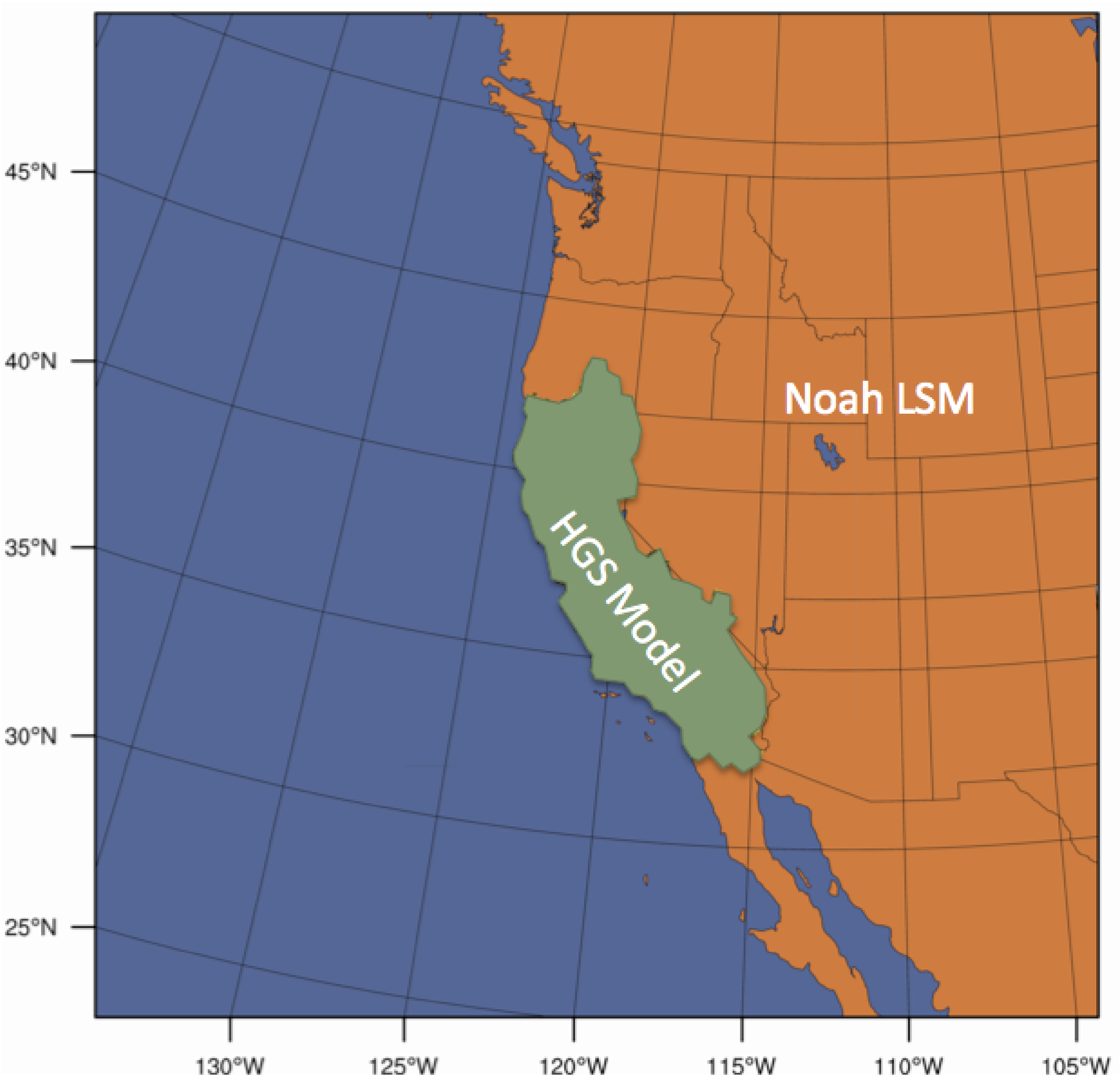

Figure 4.9: The WRF domain is the entire rectangular box, inside of the atmospheric model the land surface is prescribed by HGS for the California Basin and the Noah LSM for the rest of the domain.

4.4 Results

4.4.1 Model Spin-up

The California Basin is in a continuously transient state, as a result of dramatic ground subsidence in the Central Valley due to groundwater mining across the entire domain. In short, California's aquifers and aquitards are consistently changing (*Farr et al.*, 2015; *Mann and Gleick*, 2015). In order to run HGS, the model requires initial state values (hydraulic head) for the surface and subsurface domain. In most scenarios, the initial condition can be approximated with a steady-state model that incorporates average climate and pumping data. However, because California's groundwater levels continue to decrease year upon year, the steady-state solution (with groundwater extractions) would be an inappropriate initial condition, because the water table would be at a much lower elevation than the current measured values.

In order to properly create the correct initial condition, we spun-up the HGS model (with no groundwater and surface water extractions) in its offline mode with historical CMIP5 precipitation and PET data. Once the model reached steady state (year 1915), groundwater and surface water extractions were turned on for 100 years, and the HGS model was run to present-day conditions (year 2015). The uncalibrated depth to groundwater table results are shown in Figures 4.10 - 4.12. Due to the relatively coarse discretization of HGS, the use of simplified geology and the inclusion of groundwater extraction by lumping individual wells into pumping centers, no attempt was made to compare HGS-calculated groundwater levels to available, albeit sparse, observation. A rapid drop in groundwater head occurred across the domain especially in the southern regions of California. This result is expected because the southern region has low precipitation, high potential evapotranspiration, and high water use.

Furthermore, HGS (≈12 km^3/year) and the Gravity Recovery and Climate Experiment (GRACE) satellite (≈4–15 km^3/year) estimated similar drawdown rates in the California Basin in the 21st century, shown in Figure 4.13. Although the GRACE estimations provided by *Chen et al.* (2016) are based on a relatively coarse spatial resolution of 200,000 km^2, the close agreement lends credence to both the GRACE and uncalibrated HGS calculations. The HGS drawdown behavior illustrates that the California Basin is still in a transient condition and water storage continues to decline. If pumping rates remain the same, the California Basin will experience continuous water level declines over the next decade, which will have a severe impact on agricultural production and water supplies for human and industrial consumption.

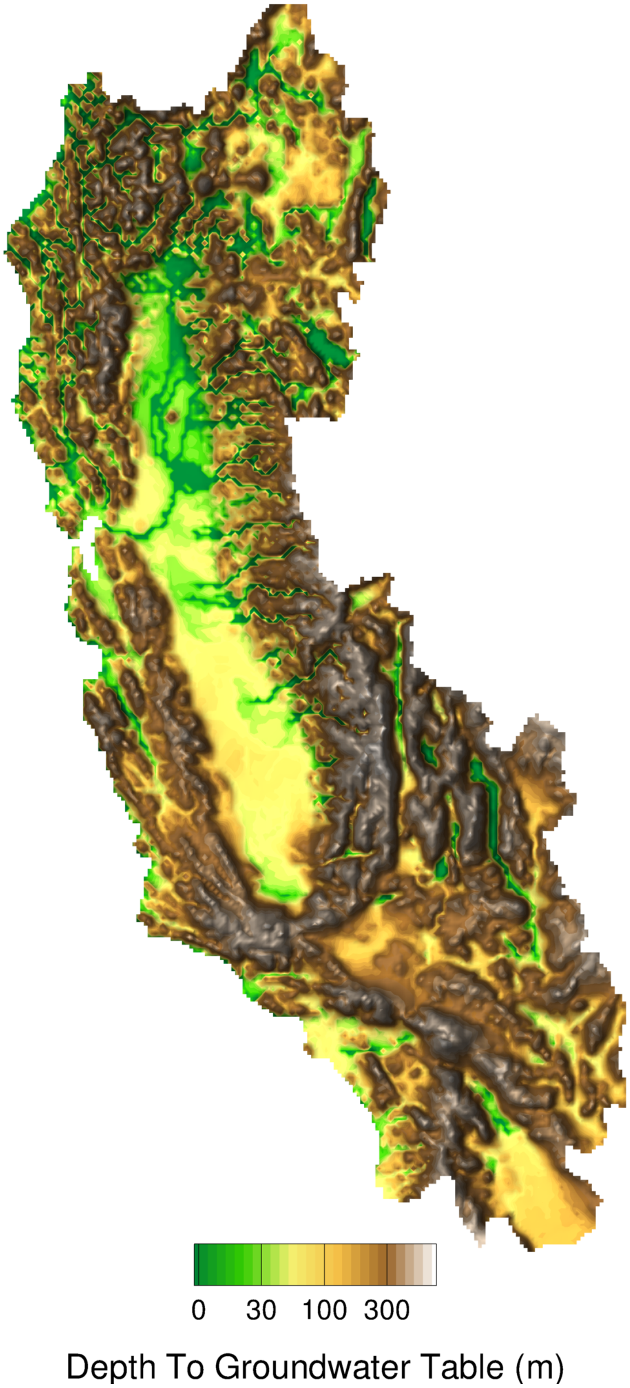

Figure 4.10: The California Basin offline simulation plotting depth to groundwater table for 1915.

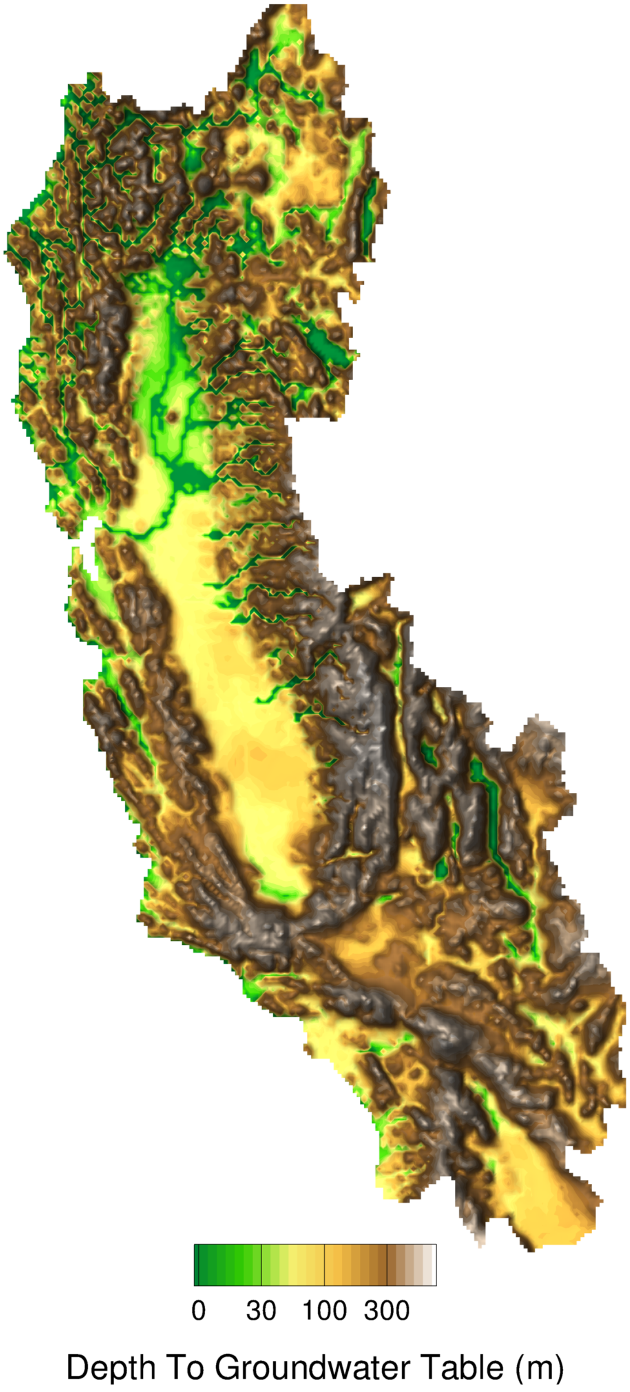

Figure 4.11: The California Basin offline simulation plotting depth to groundwater table for 1965.

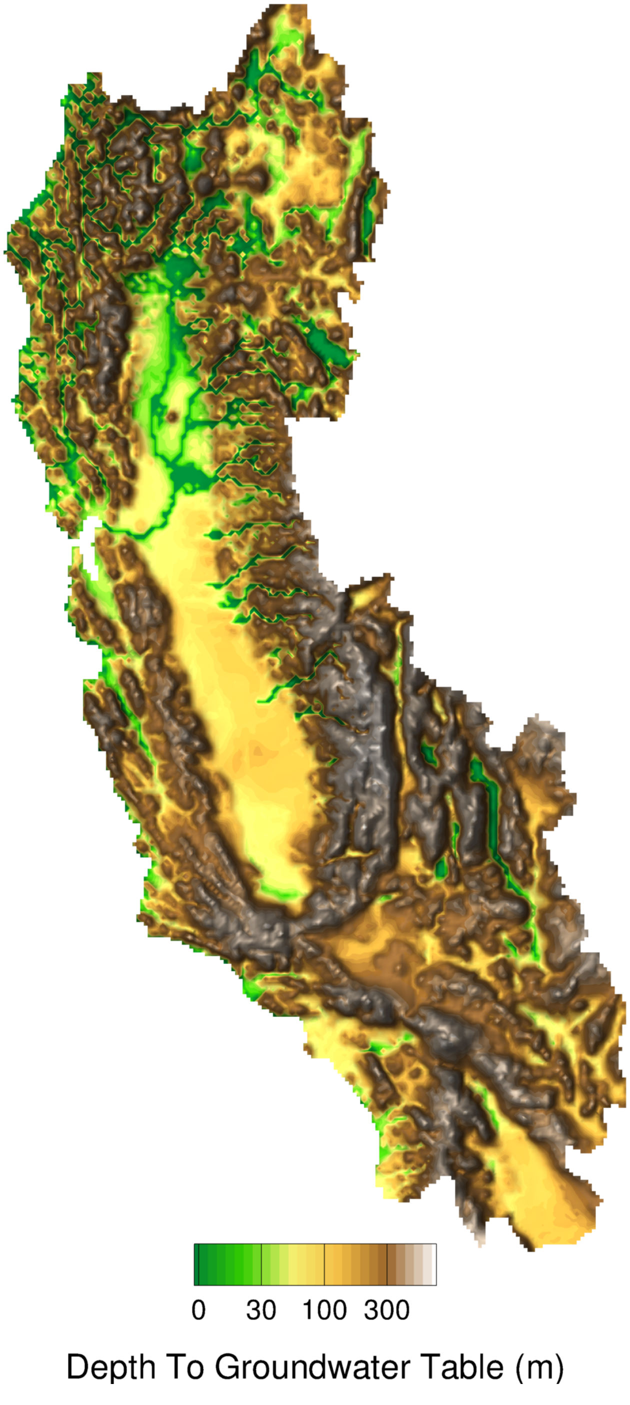

Figure 4.12: The California Basin offline simulation plotting depth to groundwater table for 2015.

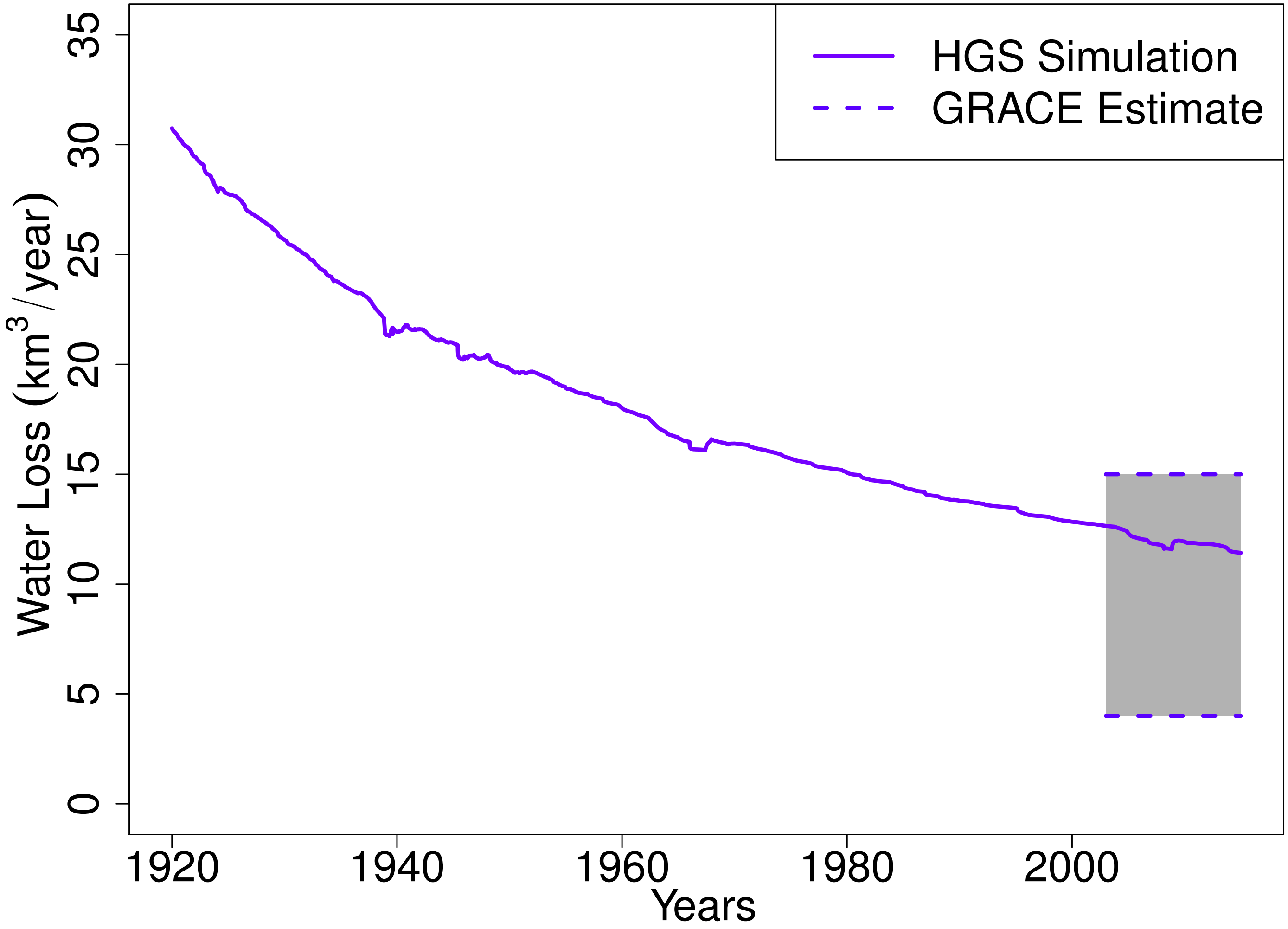

Figure 4.13: A comparison of simulated groundwater loss per year with estimated GRACE groundwater loss over the entire California Basin.

4.4.2 Coupled Simulation

Diurnal Cycle

After successfully running the model to current day conditions, the coupled HGS-WRF model was executed. The coupled model time frame was 200 days (January 1st to July 20th 2011), and the results for the first day and half are shown in Figure 4.14 and Figure 4.15. The plots include surface water in log meter depth, precipitation, evapotranspiration, and change in soil saturation over 6 time intervals. Naturally, the ET undergoes a diurnal cycle from the sun rising and setting during the day. As the ET increases it removes water from the land surface and shallow subsurface, and moves the water into the atmospheric domain—increasing the atmospheric humidity. Once water is removed from the surface and subsurface, the ET rates decline because it takes more energy to move deeper subsurface water into the atmosphere.

Conversely, as more water enters the atmosphere, the PET values decline due to a build up of humidity. Once the atmospheric humidity exceeds saturation, the water leaves the atmosphere and re-enters the surface and subsurface domains as precipitation. During heavy precipitation events, water quickly moves over the surface, collects into larger rivers, and discharges into the Pacific Ocean. Additionally, groundwater discharge replenishes the ET water loss and can continue supplying surface water flows and ET during low precipitation conditions.

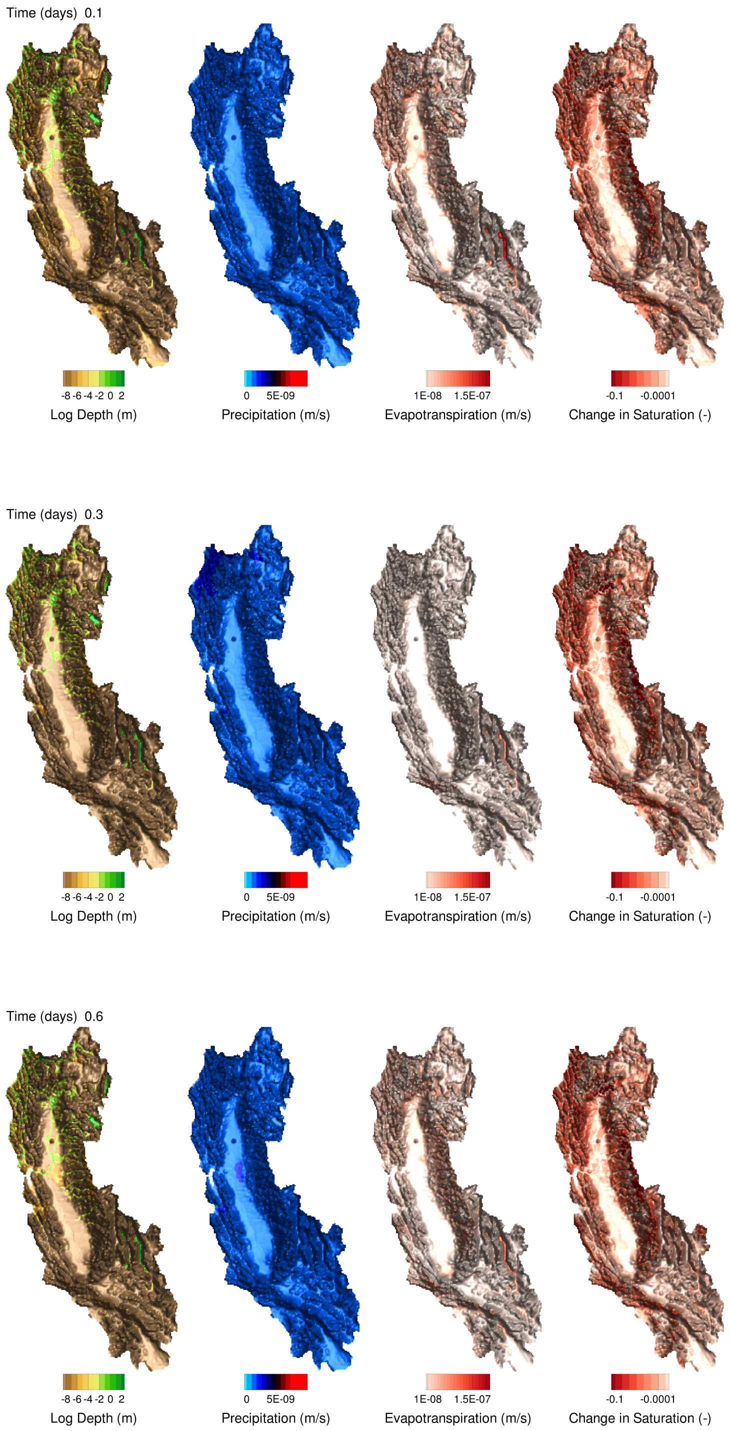

Figure 4.14: HGS-WRF simulation for the first 0.6 days.

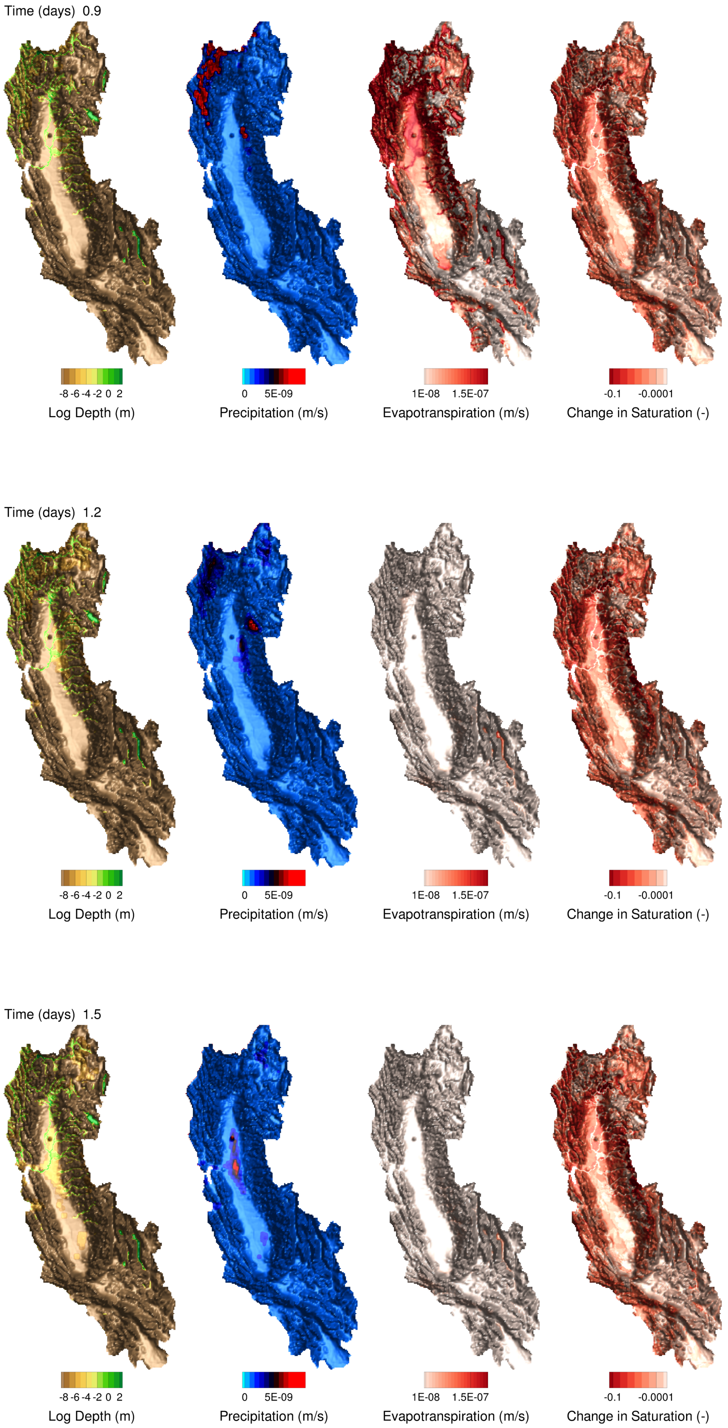

Figure 4.15: HGS-WRF simulation for day 0.9 to 1.5.

Mass Balance

The HGS-WRF mass balance for the California Basin, shown in Figure 4.16 and 4.17, summarizes the results of the simulation. The diurnal cycle of the evapotranspiration is evident in not only the AET, but also appears in the river outflow. During the large precipitation events from 40 days to 90 days, the model showed lower evapotranspiration rates due to cloud cover, colder temperatures, and high relative humidity. Moreover, the large rain events caused a sharp increase in river discharge and masked the diurnal outflow pattern. After the large precipitation events, the river outflow returns to base flow conditions.

The strong diurnal nature in the overland flow is a product of the high PET levels during the day, which removes water from the surface and subsurface. At night, PET levels drop to a fraction of the daily fluxes, and subsurface water exfiltrates into the surface domain, thus replenishing the local streams and rivers. The surface water in the rivers, with an increased stage height, produce higher river flows and more water leaves the surface domain at the outflow (via the critical depth boundary condition).

Furthermore, the cumulative mass balance for the simulation, shown in Figure 4.18, and for the 10-day averaged volumetric fluxes, shown in Table 4.6, clearly illustrates the changes in precipitation, evapotranspiration, and river flows for the simulation. Over the course of the first 40 days, evapotranspiration was the most dominant flux; however, after this period, precipitation fluxes become more influential in the overall water balance. The increased precipitation produces higher peak river flows, and overall greater overland flow discharge. Ultimately, the increase in precipitation rates for the 40 to 90 day interval correlates with a sudden decrease in actual evapotranspiration.

After 90 days, the evapotranspiration fluxes dominate the simulation. The precipitation fluxes are much lower with short periods of intense rainfall. Additionally, the 10-day averaged outflow boundary fluxes monotonically decline from 90 days untill the end of the simulation. The low precipitation rates and large evapotranspiration rates cause this decline in the surface water storage.

There is a noticeable correlation between increased precipitation and a decrease in evapotranspiration rates. For example, days 30 to 40 exhibited a mean ET of 6,600 m^3/s and precipitation rate of 300 m^3/s. The following 10-day period (days 40-50), should have higher evapotranspiration rates, due to higher solar radiation. However, the large precipitation event, 26,000 m^3/s, reduces the ET fluxes to just 5,400 m^3/s; 1,200 m^3/s lower than the previous 10-day period. Precipitation events reduce the ET fluxes by increasing the relative humidity, decreasing the surface temperature, and reducing solar radiation (from cloud cover).

Table 4.6: California Basin 10 day averaged volumetric fluxes.

Days	Evapotranspiration (m^3/s)	Precipitation (m^3/s)	River Outflow (m^3/s)
0 – 10	3,600	2,100	1,400
10 – 20	4,400	1,000	1,400
20 – 30	5,100	2,300	1,300
30 – 40	6,600	300	1,200
40 – 50	5,400	26,000	1,500
50 – 60	5,600	12,700	1,400
60 – 70	6,300	17,300	1,800
70 – 80	6,500	39,100	2,700
80 – 90	8,700	24,000	3,000
90 – 100	11,800	5,000	2,700
100 – 110	10,700	7,000	2,500
110 – 120	12,000	6,400	1,900
120 – 130	13,500	2,000	1,400
130 – 140	10,600	12,000	1,300
140 – 150	12,600	6,000	1,100
150 – 160	11,300	9,600	1,100
160 – 170	14,300	700	800
170 – 180	13,500	3,200	700
180 – 190	14,500	800	600
190 – 200	10,900	1,300	500
Mean	9,400	8,900	1,500

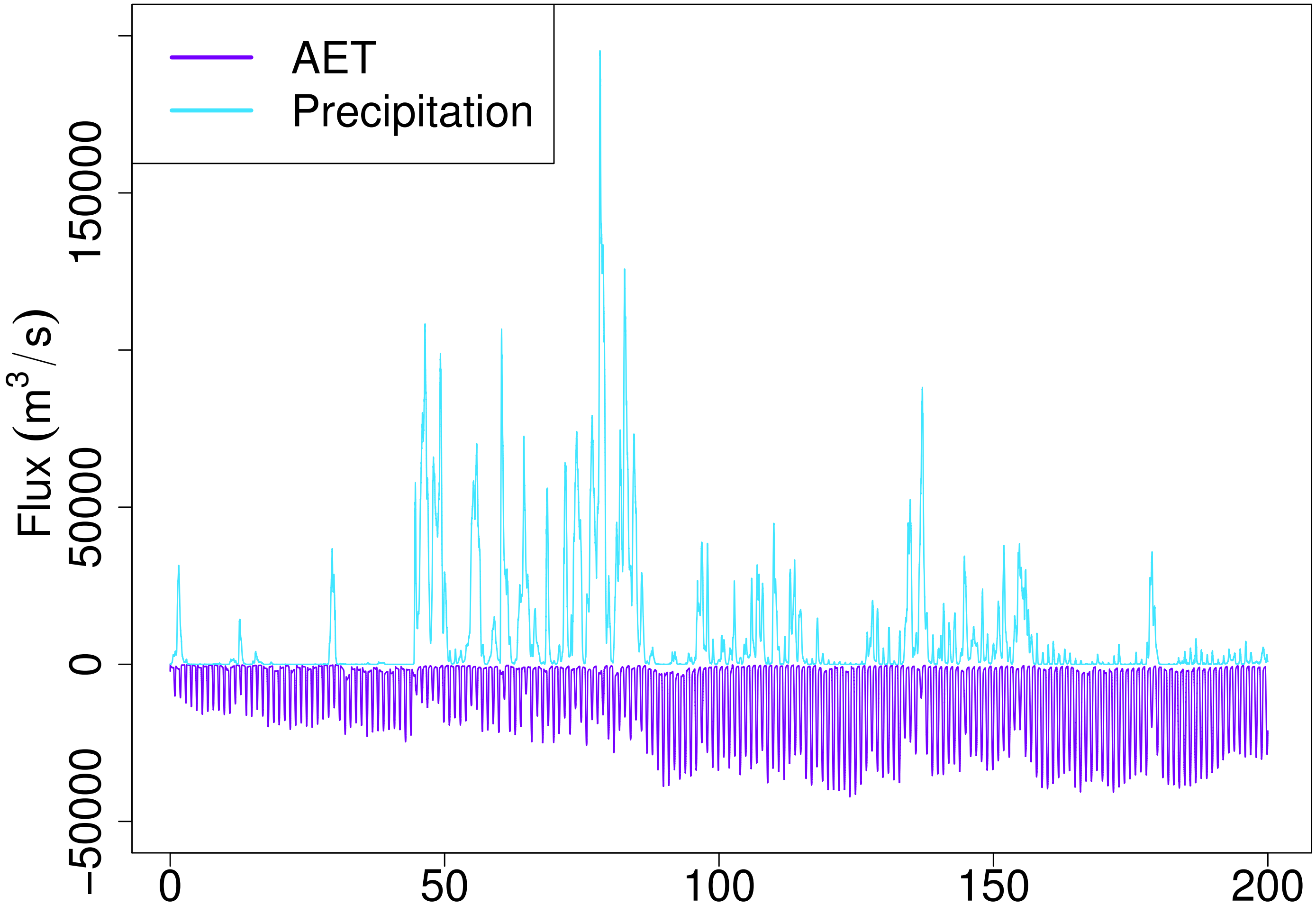

Figure 4.16: HGS-WRF California Basin mass balance for the 200-day simulation

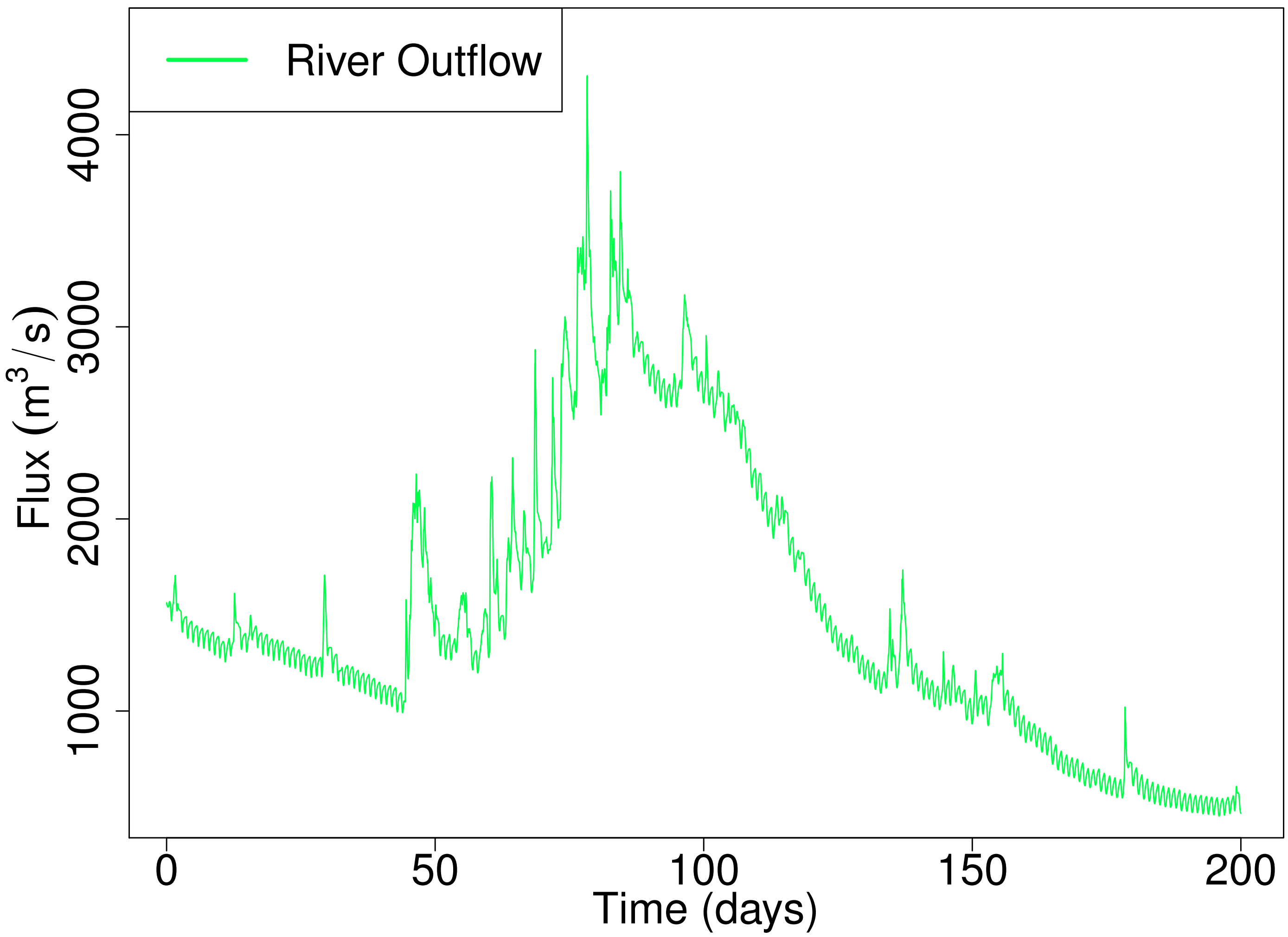

Figure 4.17: HGS-WRF California Basin mass balance for the 200-day simulation

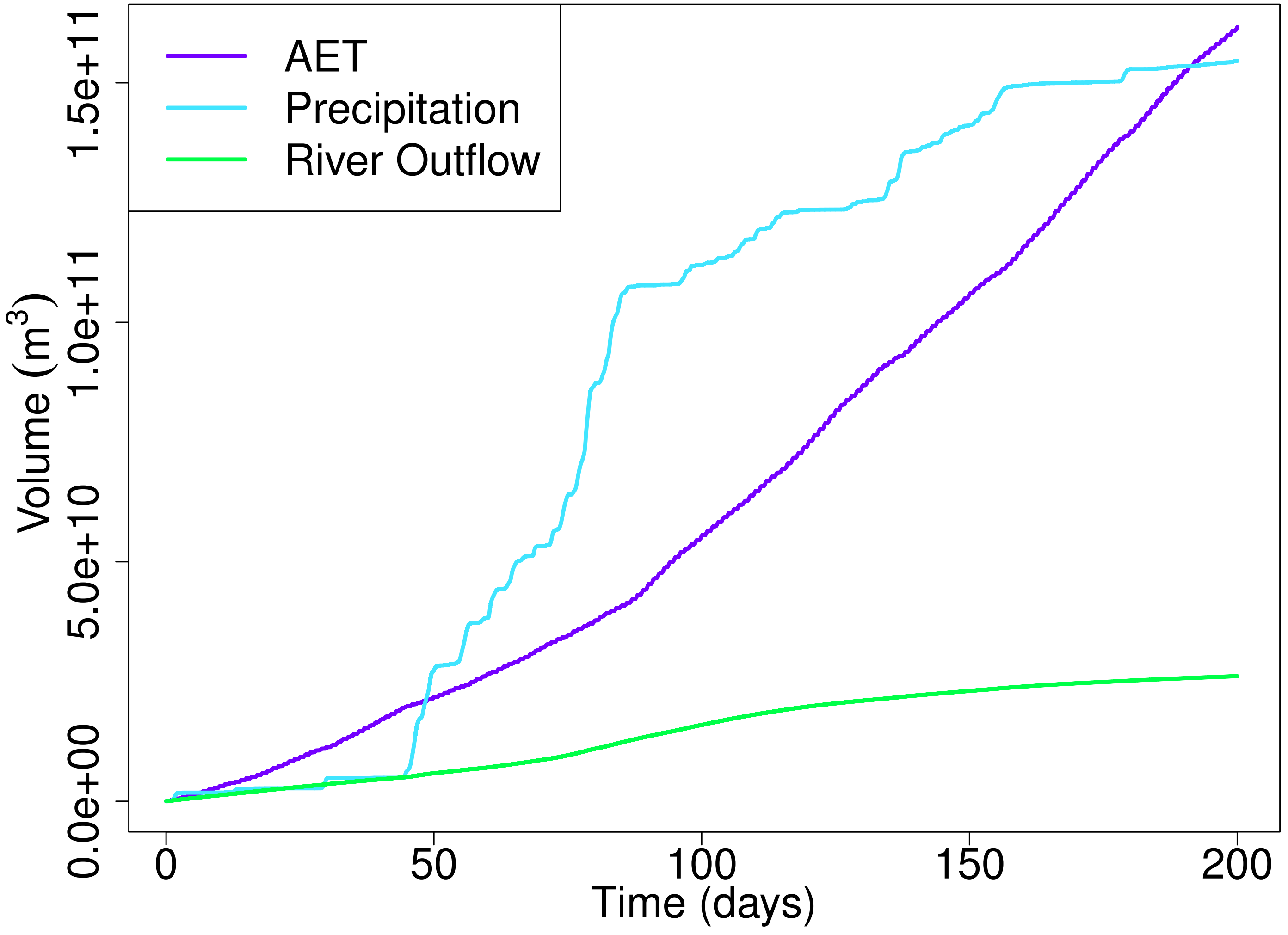

Figure 4.18: HGS-WRF California Basin cumulative mass balance for the 200-day simulation

Mean Results

The simulation results are shown in Figures 4.19 to 4.28 and include the 20-day averaged log river depths (m), precipitation (mm/day), evapotranspiration (mm/day), and changes in near surface soil saturation (-). The saturation change in the simulation initially starts at time zero; as the simulation creates precipitation, the saturation increases as shown by the blue colors. Alternatively, as more evapotranspiration removes water from the subsurface domain, the change in saturation becomes negative and trends towards the red colors.

The first forty day (January 1 to February 9), shown in Figures 4.19 and 4.20, produced low amounts of precipitation and moderate levels of evapotranspiration, producing little to no change in the surface and subsurface water storage. The trend in the precipitation patterns caused water to increase in the lowlands (e.g. Central Valley) and decrease in the highlands.

The next 60 days, from day 40 to day 100 (February 10 to April 10), shown in Figures 4.21 to 4.23, show a drastic increase in precipitation, predominately along the northern regions and the windward side of the Sierra Nevada Mountains. This water quickly increases the subsurface water quantity and replenishes the local streams and rivers. The strong increase in precipitation and cloud cover decreases the evapotranspiration fluxes which helps retain water in the surface and subsurface domains.

The last 100 days of the simulation (April 11 to July 20), shown in Figures 4.24 to 4.28 have a much lower rate of precipitation and almost no simulated precipitation in the southern portion of the state. The low levels of precipitation account for the decreasing surface and subsurface water levels. The change in saturation becomes predominately red for the entire domain, with the exception of several small regions in northern California and the Sierra Nevadas. The southern California desert regions did not show significant change in soil moisture because the soil from the initial condition was already dry, reducing the amount of available water for evapotranspiration.

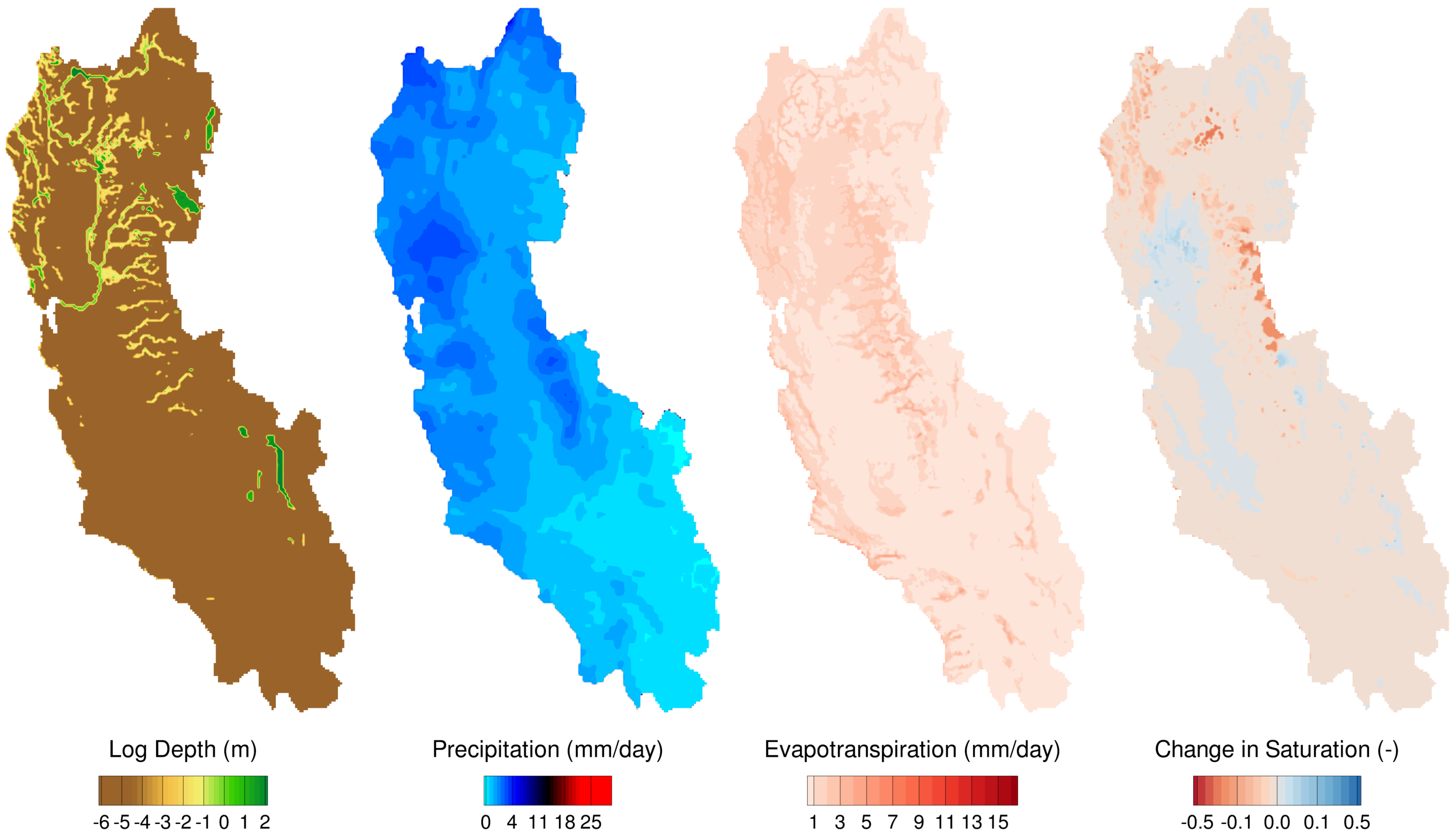

Figure 4.19: Coupled HGS-WRF simulation displaying averaged log depth, precipitation, evapotranspiration, and change in saturation for 1 to 20 days (January 1 to January 20).

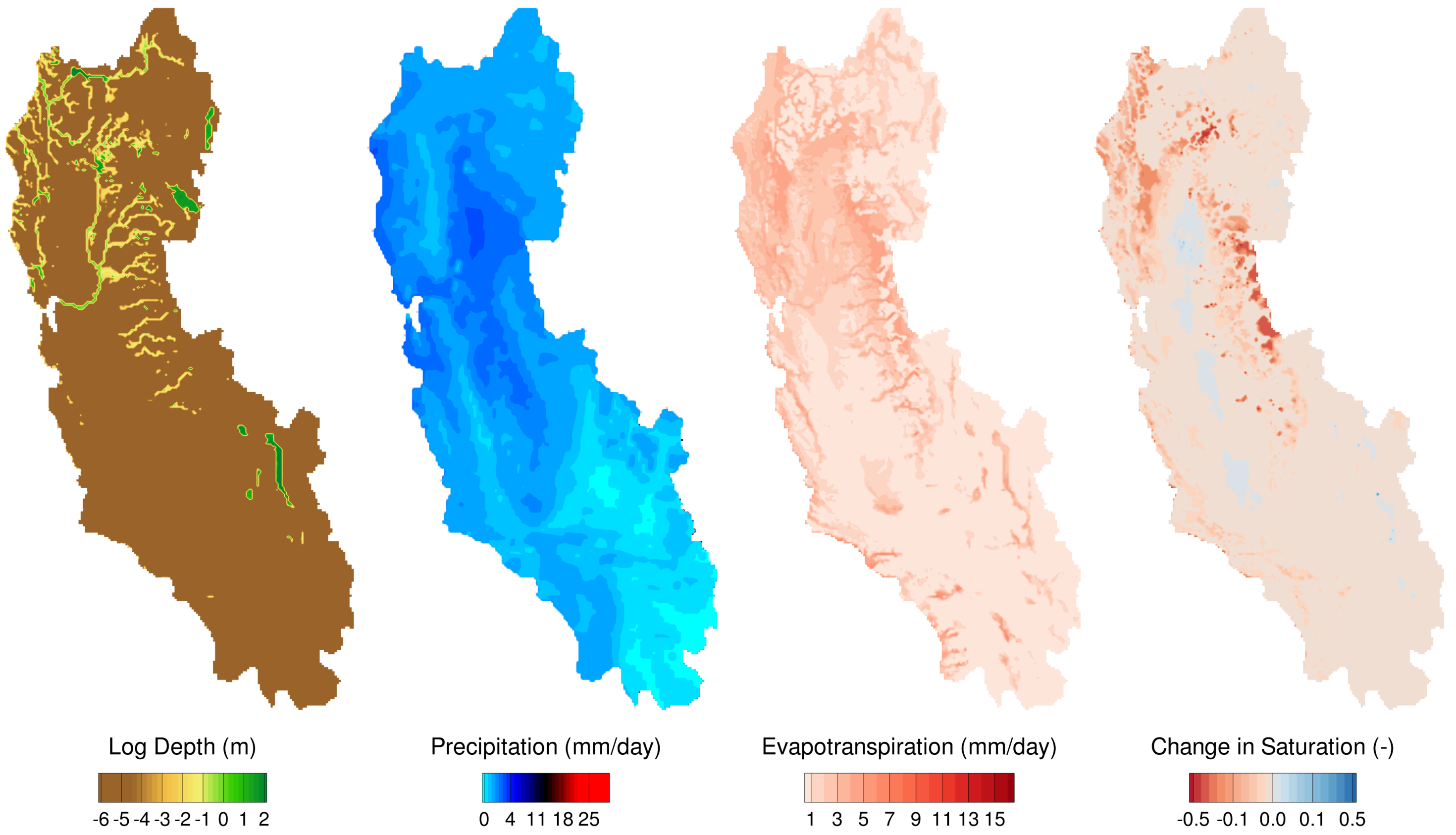

Figure 4.20: Coupled HGS-WRF simulation displaying averaged log depth, precipitation, evapotranspiration, and change in saturation for 21 to 40 days (January 21 to February 9).

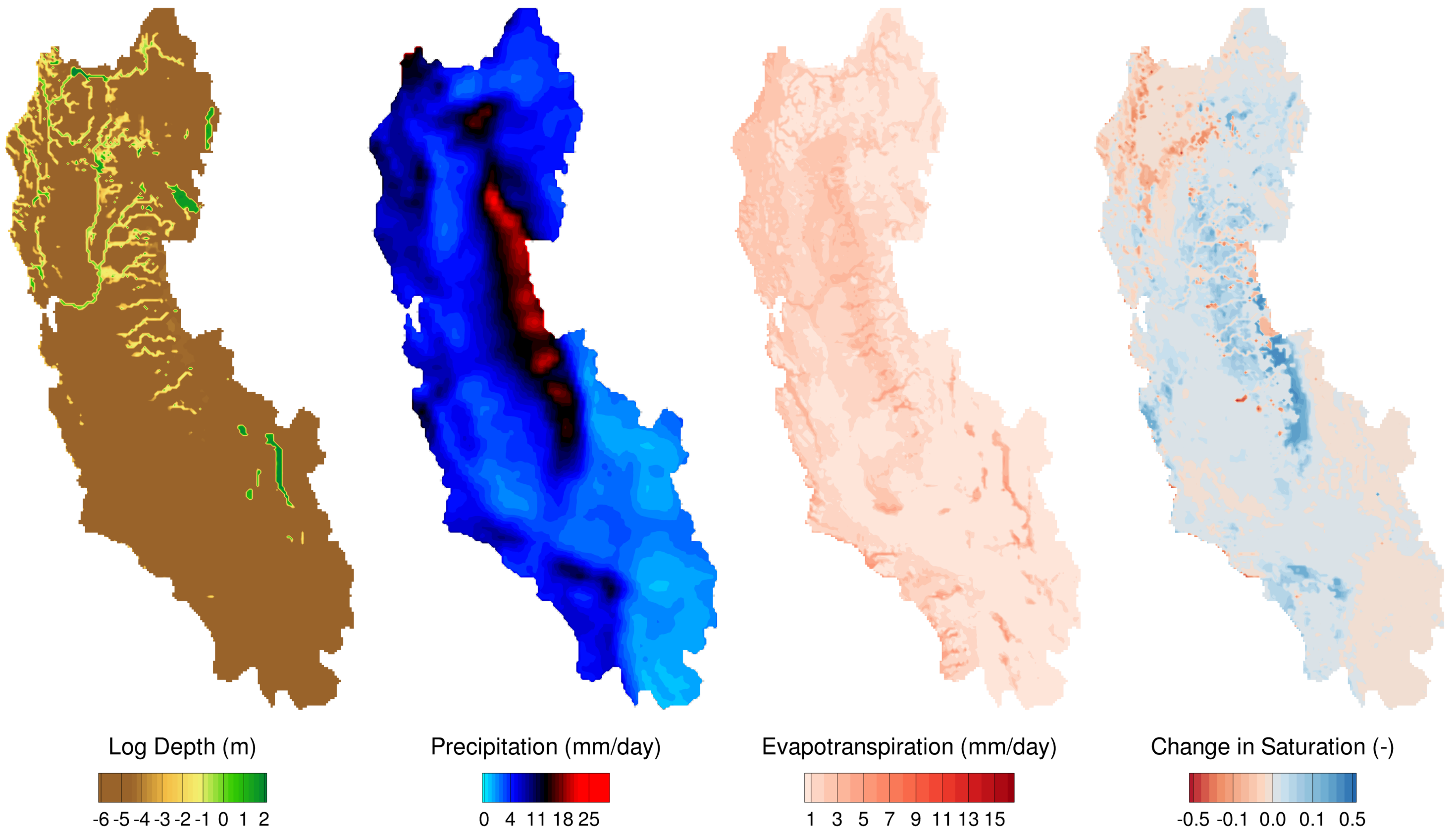

Figure 4.21: Coupled HGS-WRF simulation displaying averaged log depth, precipitation, evapotranspiration, and change in saturation for 41 to 60 days (February 10 to March 1).

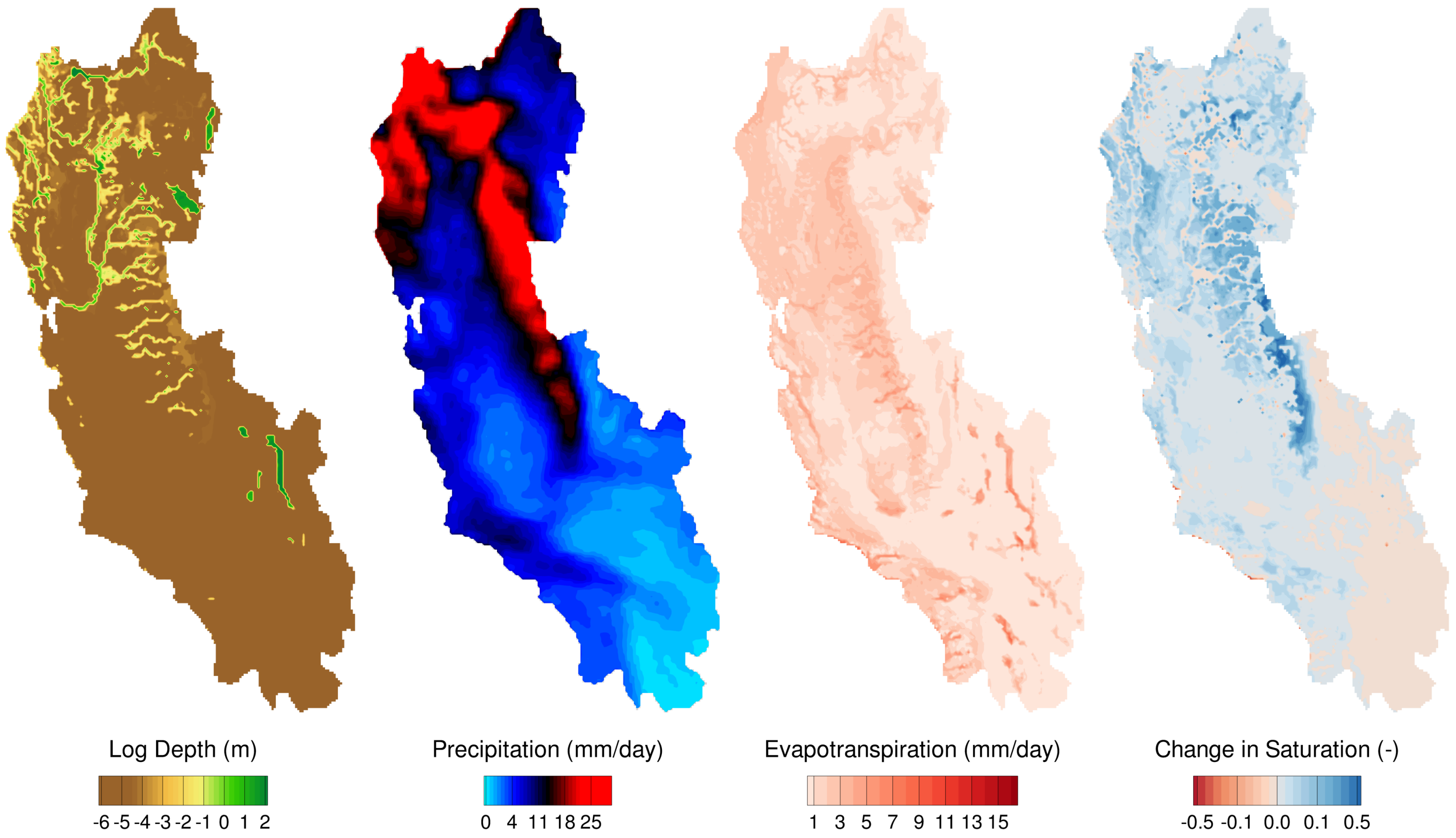

Figure 4.22: Coupled HGS-WRF simulation displaying averaged log depth, precipitation, evapotranspiration, and change in saturation for 61 to 80 days (March 2 to March 21).

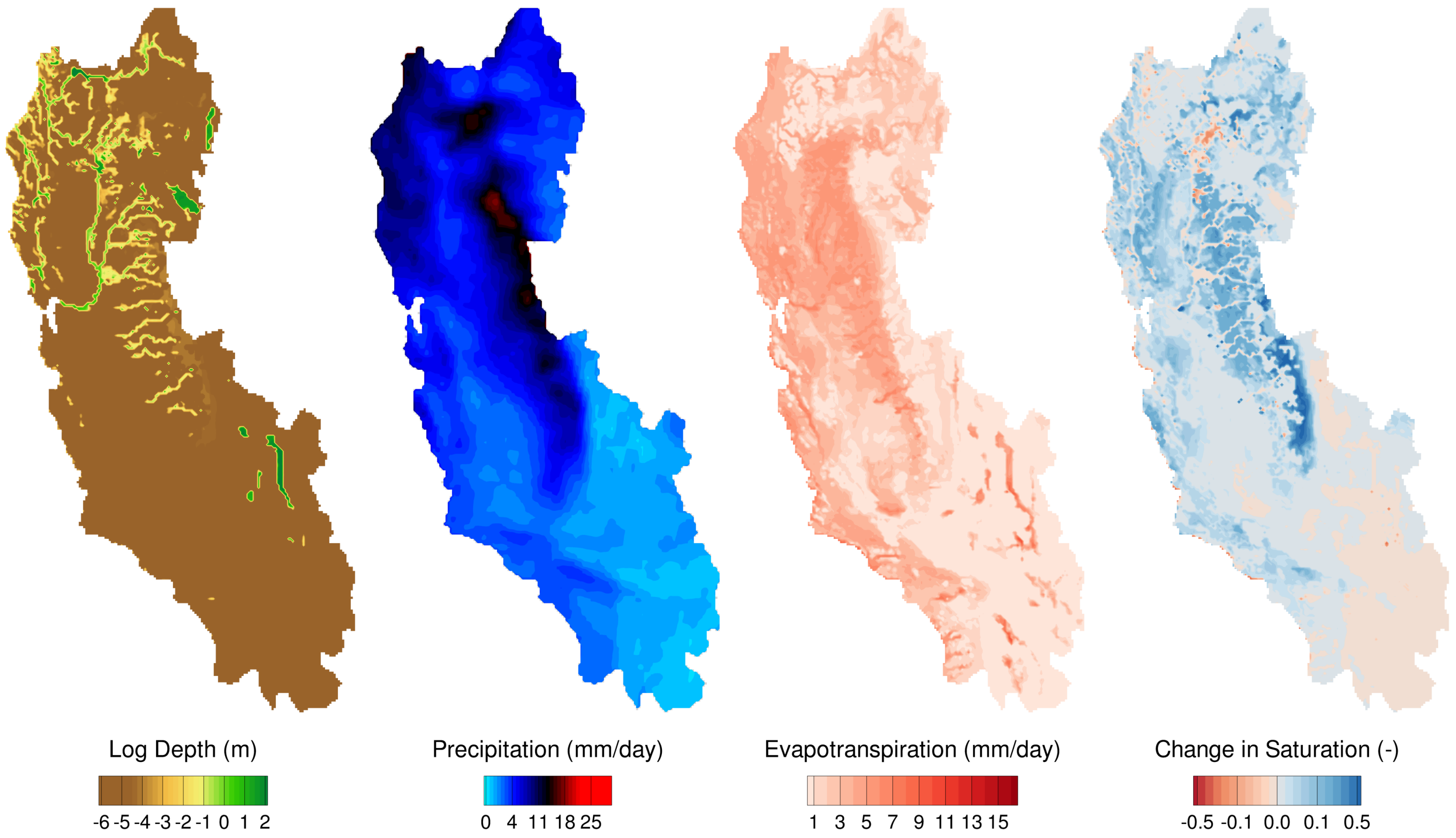

Figure 4.23: Coupled HGS-WRF simulation displaying averaged log depth, precipitation, evapotranspiration, and change in saturation for 81 to 100 days (March 22 to April 10).

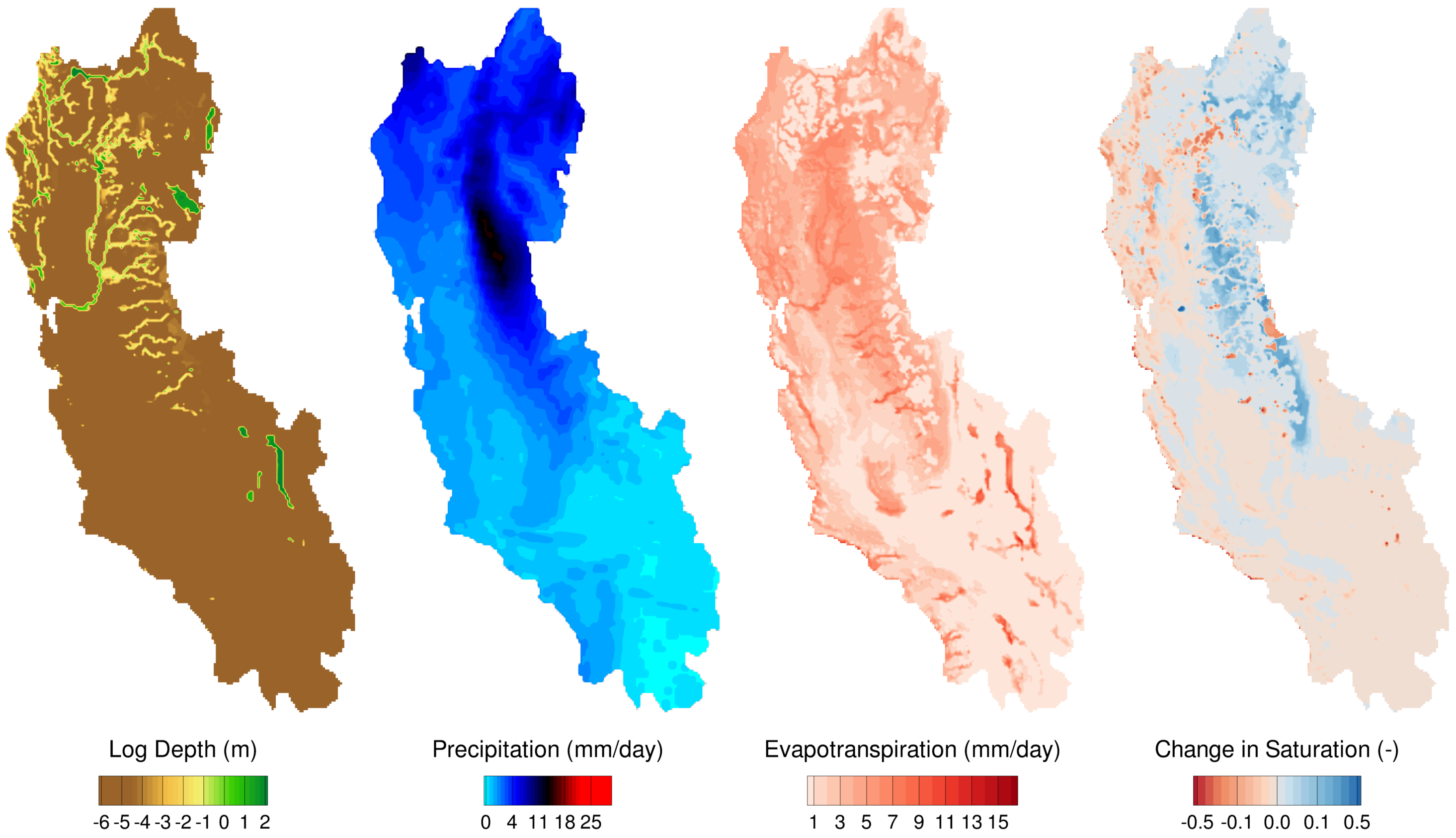

Figure 4.24: Coupled HGS-WRF simulation displaying averaged log depth, precipitation, evapotranspiration, and change in saturation for 101 to 120 days (April 11 to April 30).

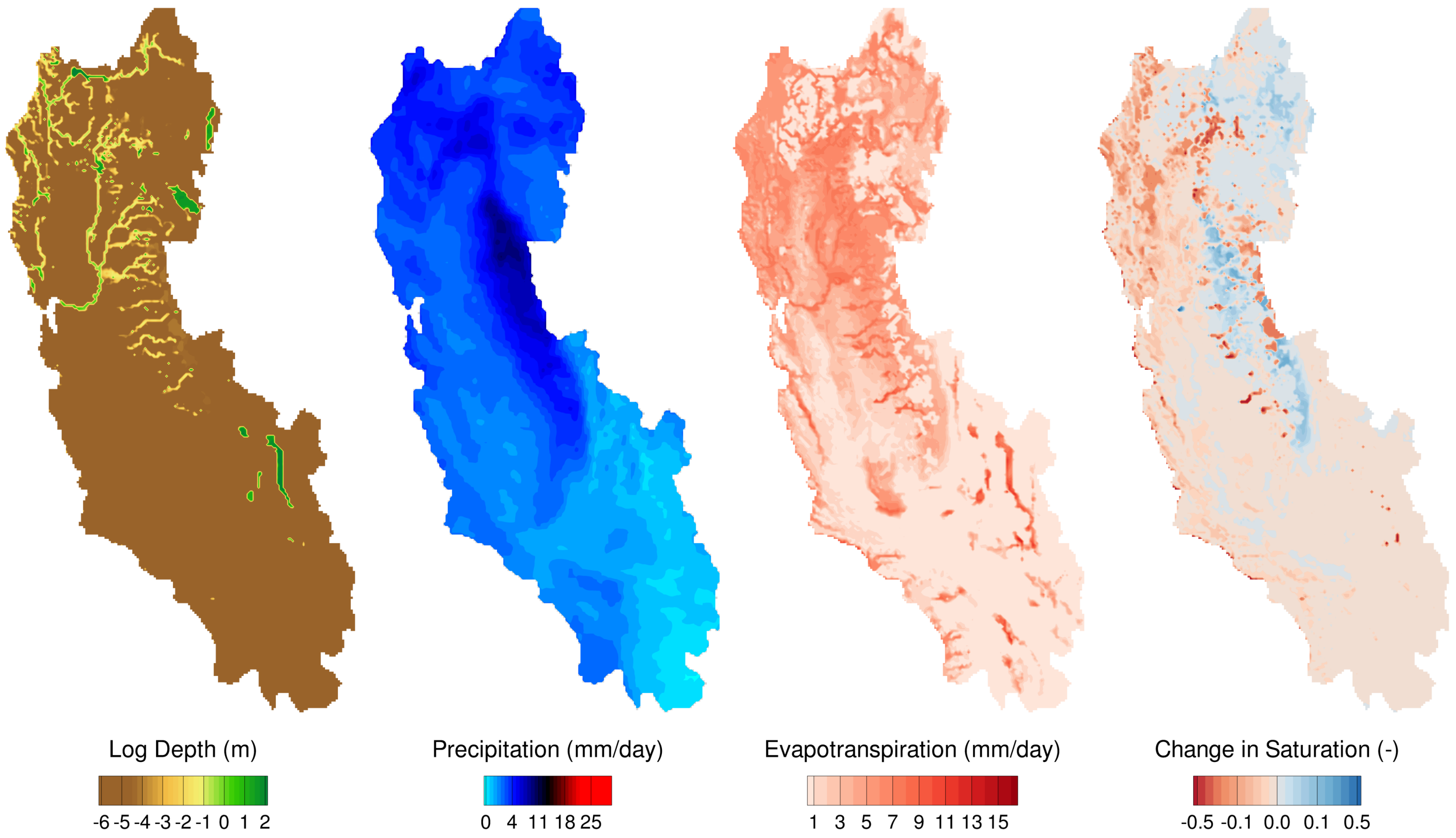

Figure 4.25: Coupled HGS-WRF simulation displaying averaged log depth, precipitation, evapotranspiration, and change in saturation for 121 to 141 days (May 1 to May 20).

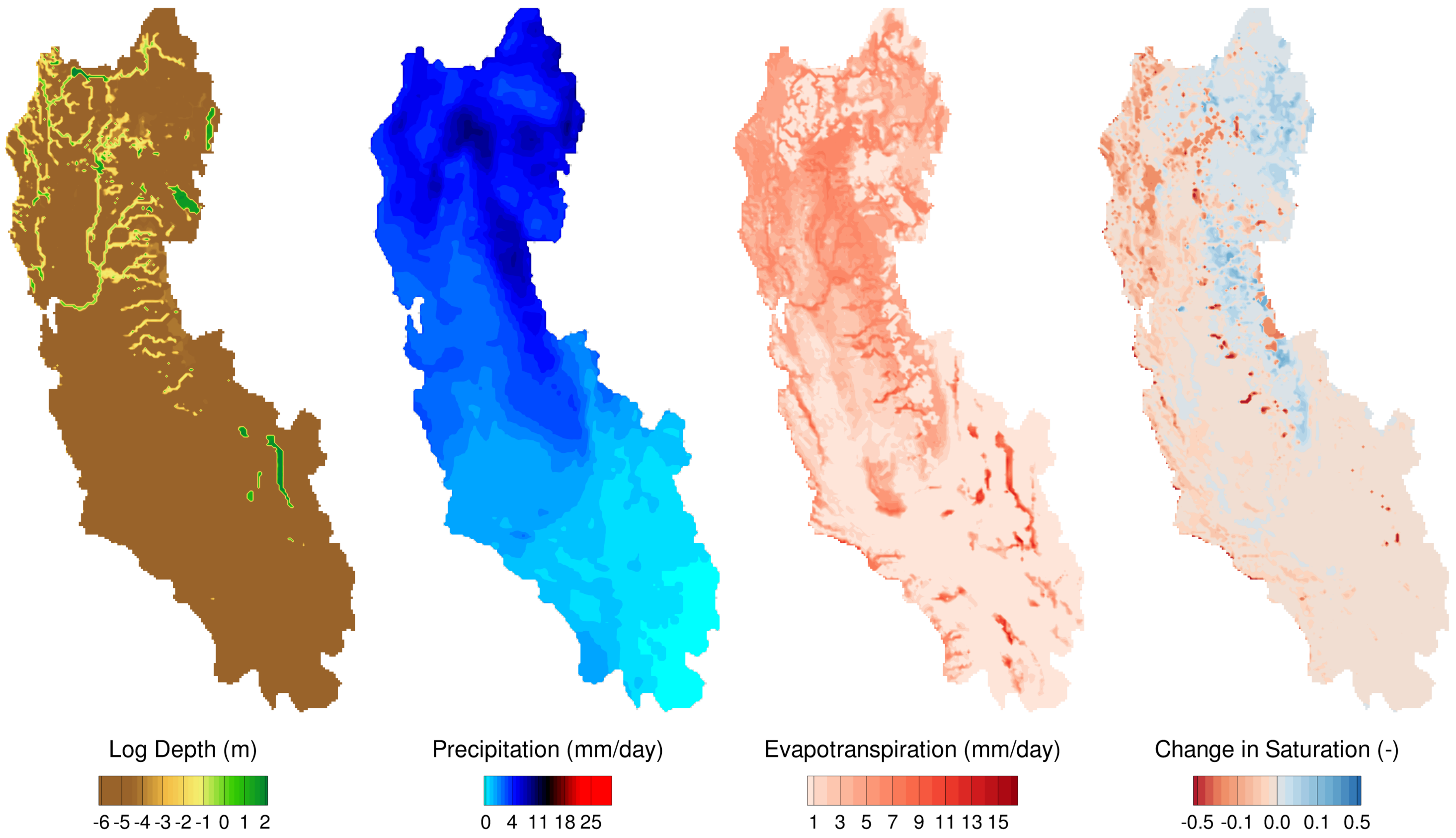

Figure 4.26: Coupled HGS-WRF simulation displaying averaged log depth, precipitation, evapotranspiration, and change in saturation for 141 to 160 days (May 21 to June 9).

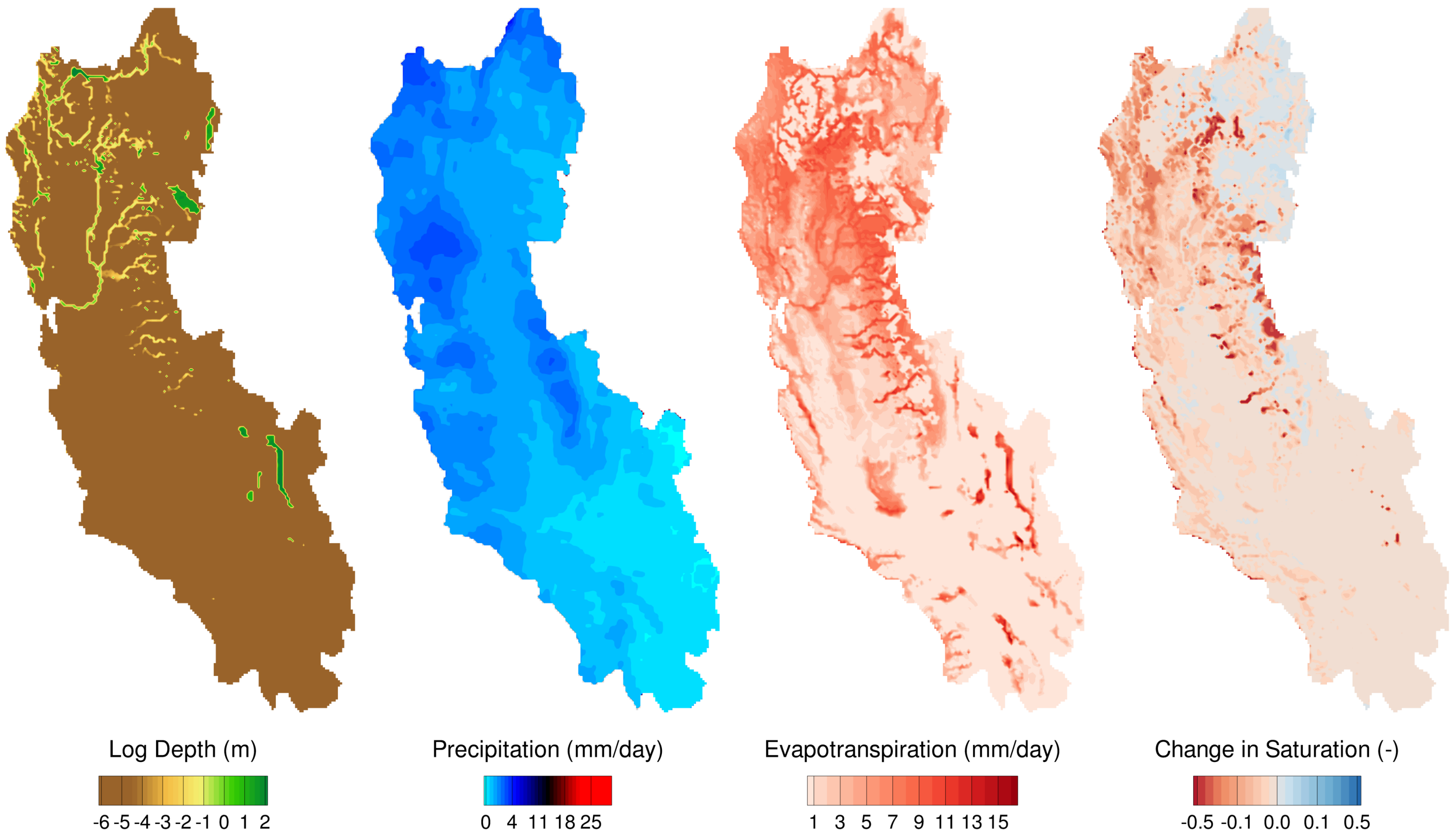

Figure 4.27: Coupled HGS-WRF simulation displaying averaged log depth, precipitation, evapotranspiration, and change in saturation for 161 to 180 days (June 10 to June 29).

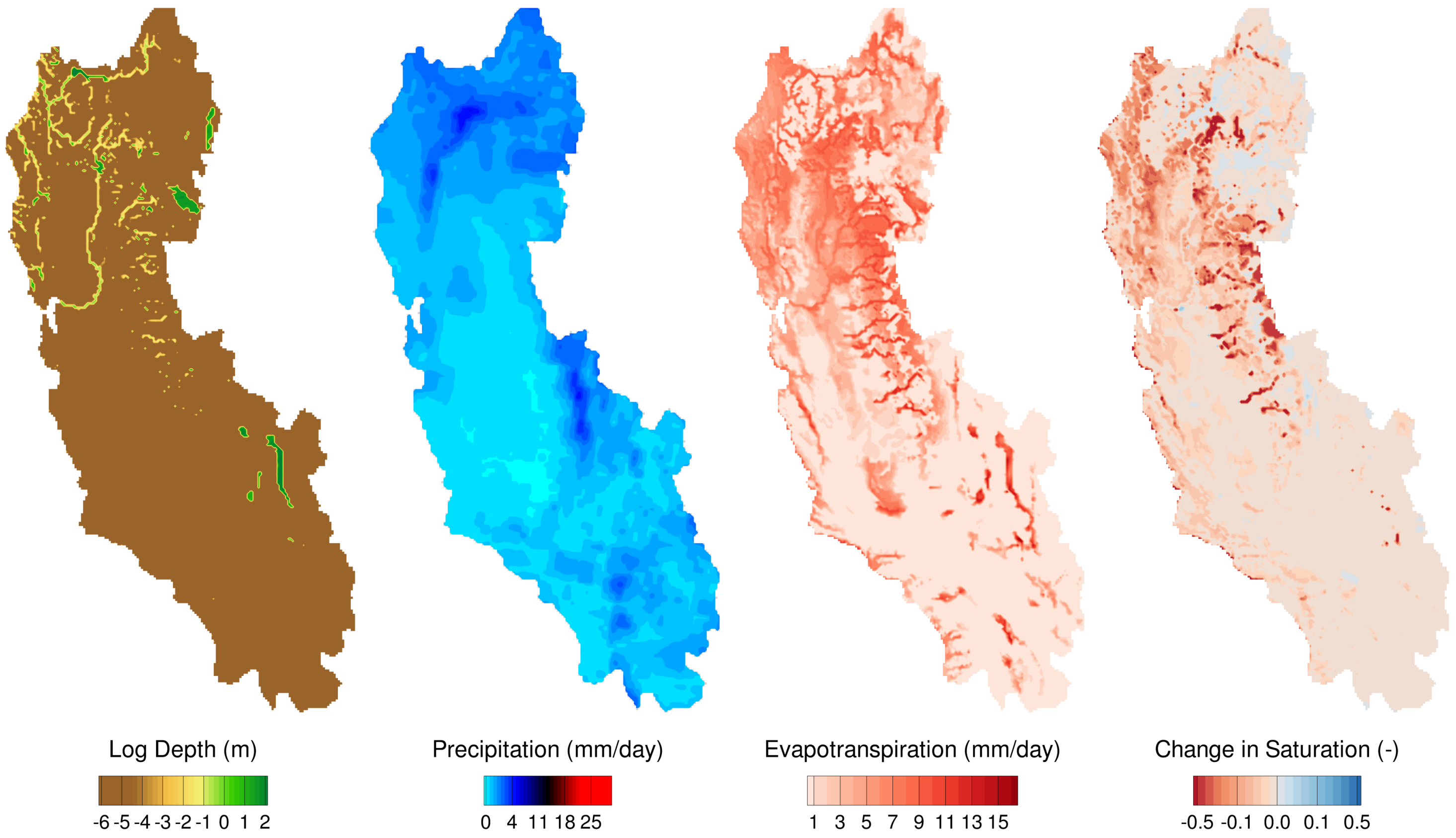

Figure 4.28: Coupled HGS-WRF simulation displaying averaged log depth, precipitation, evapotranspiration, and change in saturation for 181 to 200 days (June 30 to July 20).

Model Comparison: Precipitation and Evapotranspiration

The HGS-WRF simulation results were compared to three data observation stations that are part of California Department of Water Resources' California Irrigation Management Information System (*California Department of Water Resources*, 2016). The three stations are the Fair Oaks (Sacramento County in the Sacramento Valley), Arvin (Kern County in the Central Valley), and Hopland2 (Mendocino County in the North Coast Valleys). The 20-day mean precipitation and evapotranspiration are shown in Figures 4.29 and 4.30. In both figures, the HGS-WRF simulation produces an overall higher precipitation and higher evapotranspiration rates.

Furthermore, the simulated vs. the observed data for precipitation and evapotranspiration are shown in Figures 4.31 and 4.32, and the mean absolute error for the three stations is shown in Table 4.7. These biases may be tied together; the extra available water (from precipitation) will produce more evapotranspiration, and the stronger evapotranspiration fluxes will produce more precipitation.

Table 4.7: California Basin Mean Absolute Error.

	Precipitation (mm/day)	Evapotranspiration (mm/day)
Fair Oaks	0.7	1.7
Arvin	0.2	0.4
Hopland2	0.9	1.9

Overall the precipitation and evapotranspiration fluxes show a moderate bias. However, the general behavior of the simulation follows the observed data: during the weeks of high observed precipitation, the HGS-WRF model simulated higher precipitation rates; during the weeks of lower precipitation rates, the model displayed lower simulated rates. This behavior is encouraging; it indicates that the modeling physics are correct but the parametrization of the surface and subsurface domains need improvement. Tuning several parameters (e.g. hydraulic conductivity, leaf area index, root zone depth, and transpiration coefficients) would improve the skill of the simulation.

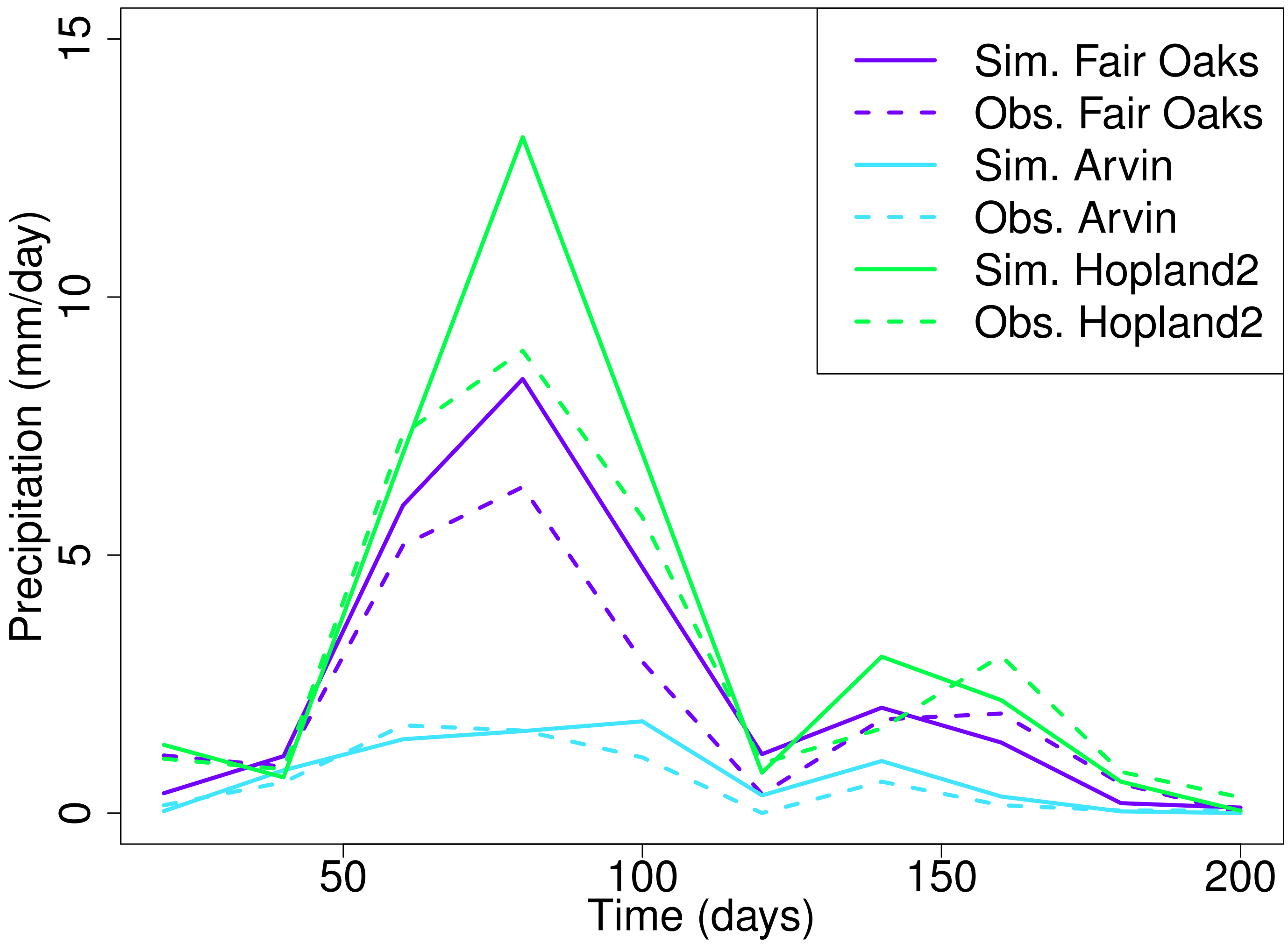

Figure 4.29: 20-day mean precipitation for three MET stations in the California Basin.

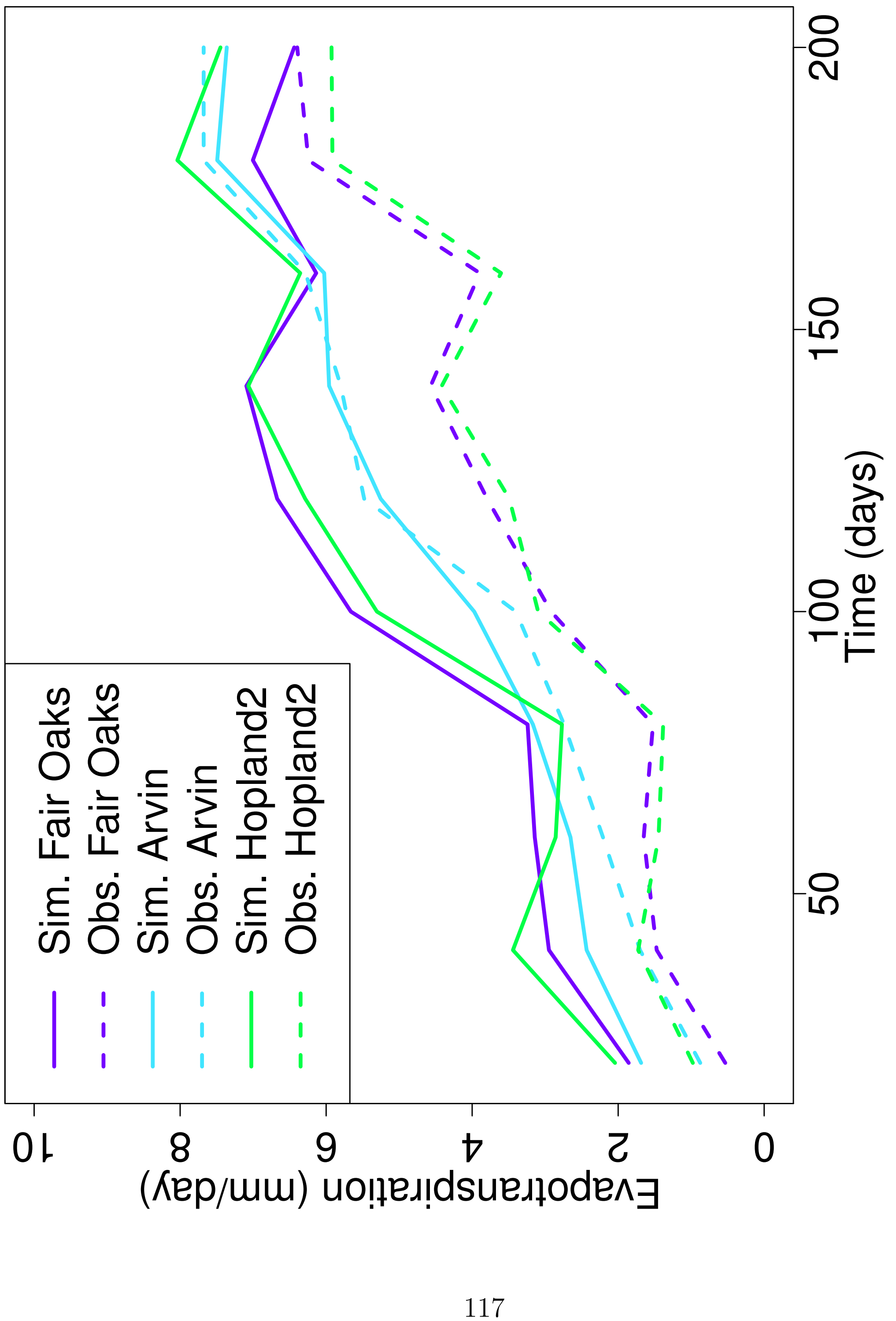

Figure 4.30: 20-day mean evapotranspiration for three MET stations in the California Basin.

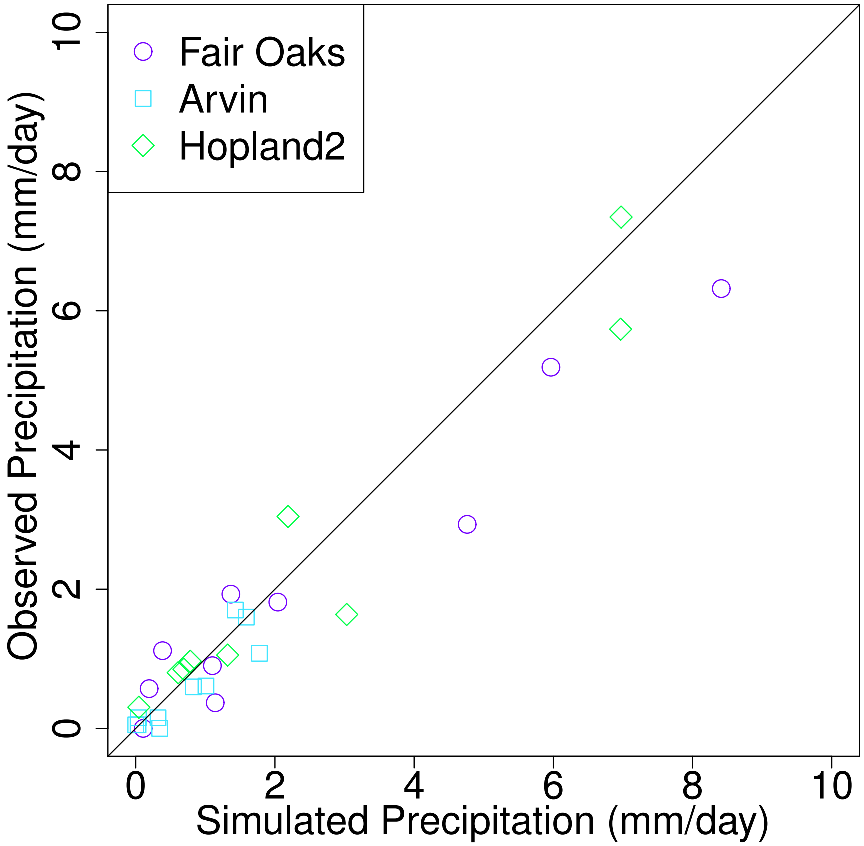

Figure 4.31: Simulated vs. Observed precipitation for three MET stations in the California Basin.

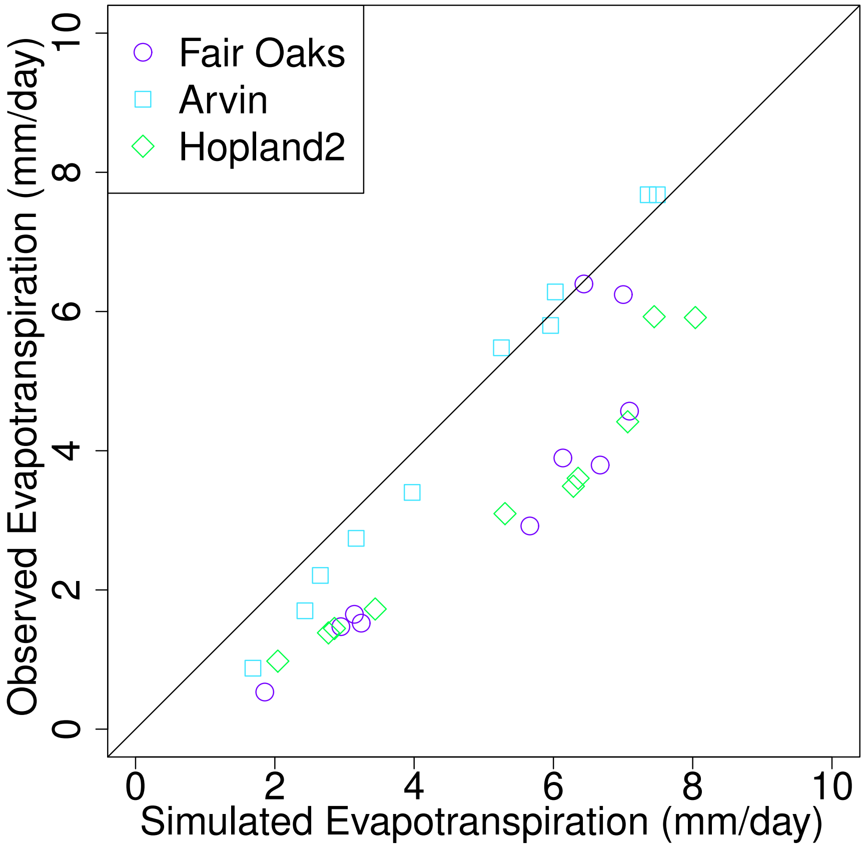

Figure 4.32: Simulated vs. Observed evapotranspiration for three MET stations in the California Basin.

Model Comparison: Overland Flow

California's water resources are altered with manmade infrastructure (e.g. dams, canals, channels, culverts, weirs, and pumping) distributed throughout the region. For example, California has 1,594 dams, and each one has its own lengthy operating guideline manuals to optimize for flood protection, hydropower, consumptive use, and environmental impact (*United States Army Corps of Engineers*, 2016). The public often misunderstands the drainage of reservoirs to maintain minimum base flows, believing that water stored in a reservoir should be primarily set aside for agriculture and human use.

Farmers, implementing their riparian rights, directly irrigate their crops from local rivers and aquifers. Additionally, these same farmers divert their excessive soil moisture (using tile drains and drainage ditches) back into the river. Including each individual stakeholder and infrastructural detail is extremely difficult, especially at the 4km horizontal resolution. With these limitations in mind, a comparison of river fluxes to measured flow for the Freeport, CA (Sacramento river) and Klamath, CA (Klamath river) gauging stations are shown in Figures 4.33 and 4.34, respectively (*United States Geological Survey*, 2016). The Freeport and Klamath gauging stations are the most downstream locations for both of the rivers, before they discharge into the San Francisco Bay and Pacific Ocean. The Sacramento river is the largest river in California and the Klamath is the second largest.

The coupled HGS-WRF simulation captures the general trend of the observed hydrograph for both the Freeport and Klamath stations. Starting from initial conditions, the simulated surface water flow is underpredicted for both rivers. Once the larger precipitation events start (40 to 90 days), the flow increases for the Freeport station and the peak flow matches the measured levels. After the peak event, the Sacramento river continues to flow at a higher rate than the simulated results. This behavior may be explained by the lack of dams and reservoirs being incorporated in the simulation. Additionally, the observed Sacramento river data shows a strong tidal influence, and the HGS-WRF simulation did not include tidal physics.

Overall, the HGS-WRF simulation better matches the peak flow behavior for the Sacramento river than it does for the Klamath river. The HGS-WRF simulation maintained baseflow for the Klamath river but was not able to match the flashy peak response of the northern watershed. Decreasing the subsurface hydraulic conductivity for the Klamath basin would increase the rainfall response and could potentially increase the simulation skill during peak flows. However, this modification could potentially cause a decrease in overall base flows and may drastically alter groundwater infiltration. Without the inclusion of dams and reservoirs, matching baseflow and peak behavior is problematic. Furthermore, the 4 km grid spacing dissipates and averages the surface water flow over a large wetted perimeter, which decreases the depth of surface water and decreases the peakiness of flow. Nevertheless, the results presented here are encouraging for an uncalibrated model that excludes important engineered structures within the California Basin.

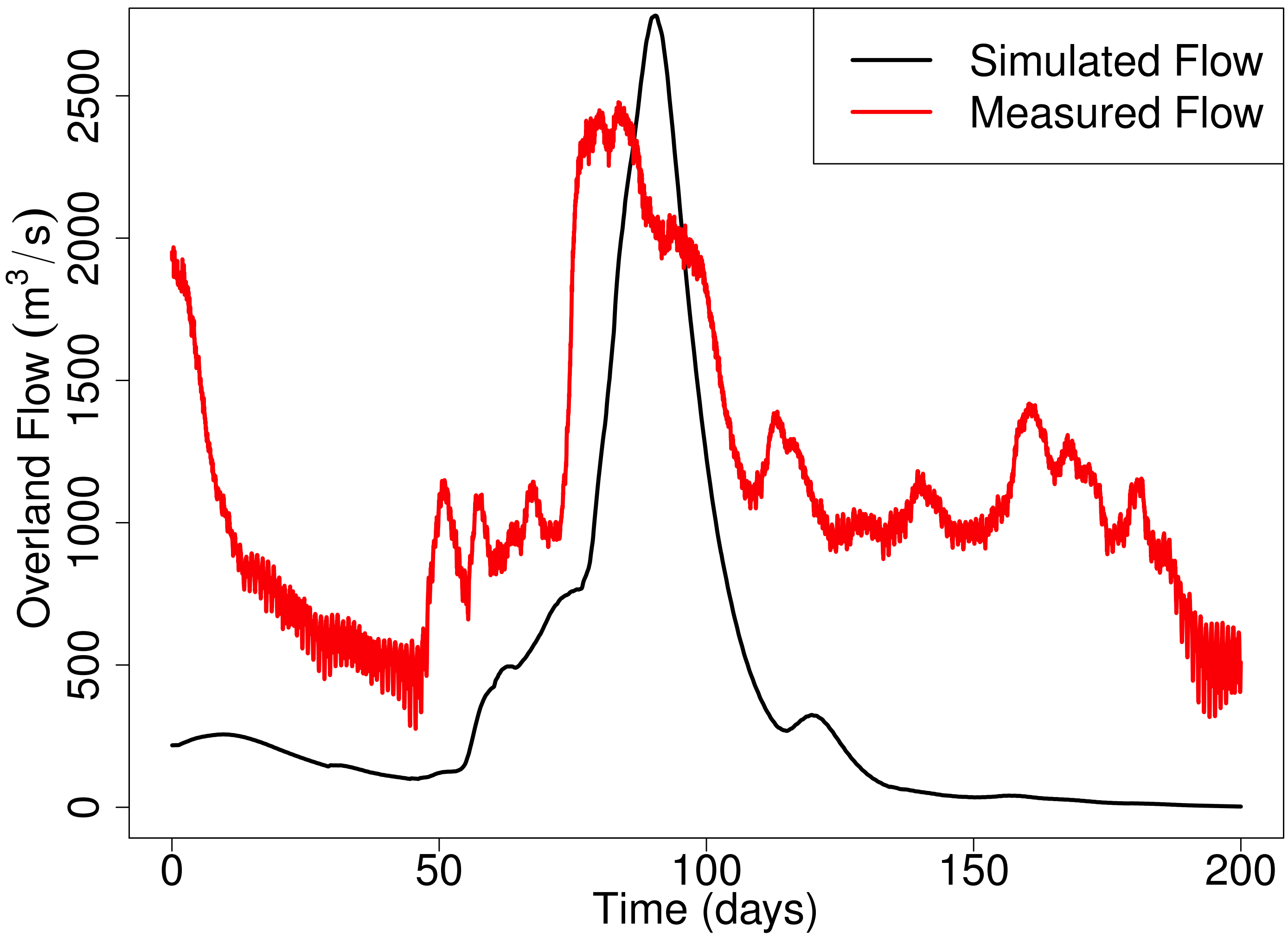

Figure 4.33: Sacrameto river gauging station comparison between observed and simulated data for USGS 11447650 SACRAMENTO R A FREEPORT CA

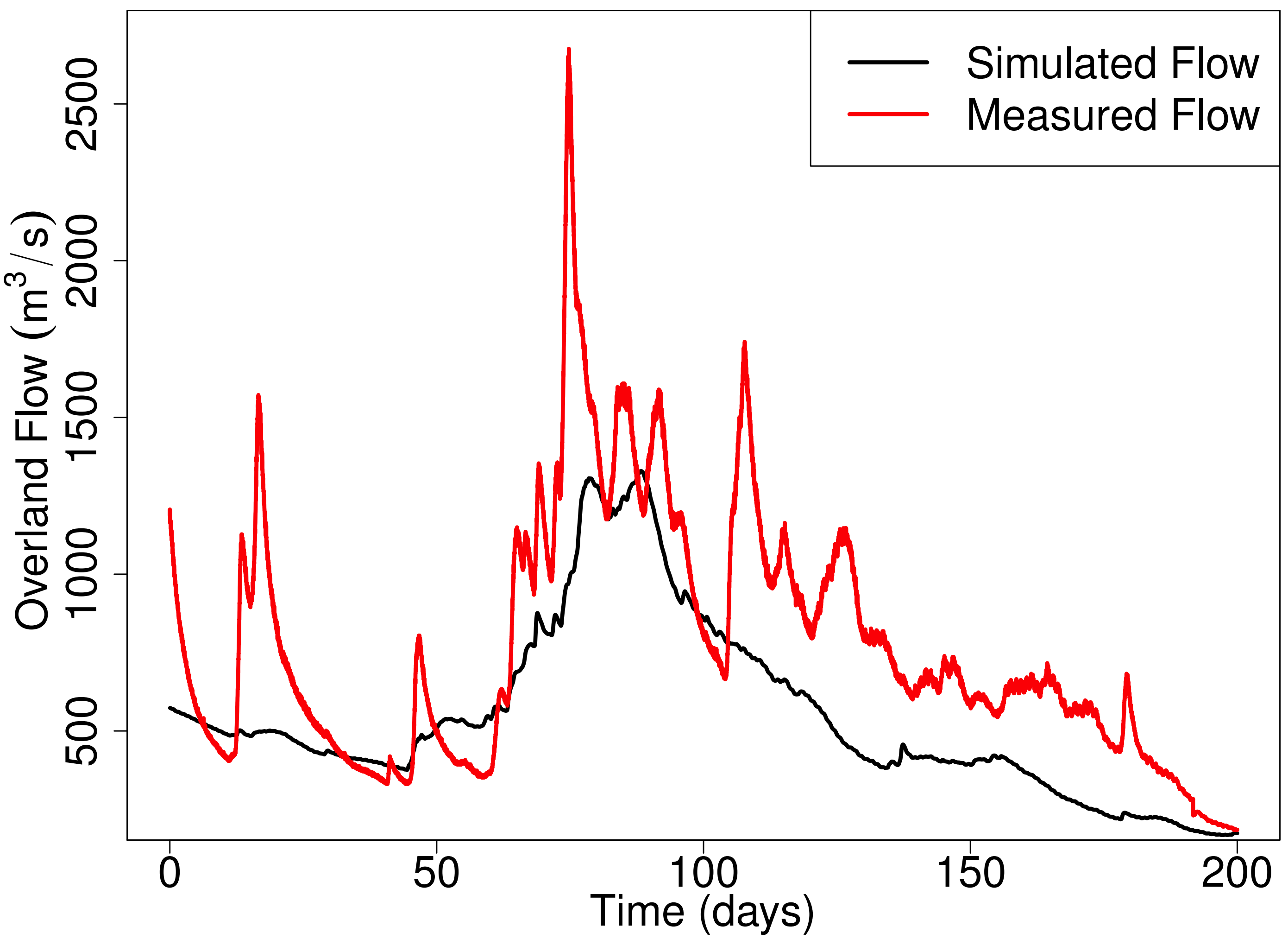

Figure 4.34: Klamath river gauging station comparison between observed and simulated data for USGS 11530500 KLAMATH R NR KLAMATH CA.

Chapter 5

Conclusion

Coupled atmospheric, surface and subsurface models have advanced significantly in recent years. Previous modeling attempts have limited the connection between the atmosphere and the subsurface to, at best, the first 2-meters of the soil column using a 1-D conceptualization, and, at worst, an uncoupled model forcing. By coupling HydroGeoSphere, an advanced 3-D surface/subsurface flow and transport model, to two separate atmospheric models, we have demonstrated the path forward to employ fully-coupled models that can be used to assess the relative importance of various interactions between the atmosphere, the land surface, and the subsurface.

In this study, the HGS model is first coupled to a simplified zero-dimensional Atmospheric Boundary Layer model. The HGS-ABL modeling platform is then compared with the Noah LSM and found a reasonably good fit between the two methods. The HGS-ABL simulations show that current LSMs are too shallow for handling deep root-zone interactions and do not provide an adequate representation for subsurface heat storage. The HGS-ABL simulation results also found that a positive correlation exists between the soil moisture and the energy feedbacks similar to the results of *Quinn et al.* (1995), *Maxwell et al.* (2007), and *Maxwell and Kollet* (2008). The principal advantage of implementing HGS as a land surface model over the previous generation of LSMs is that our approach integrates heat transport, water flow, and evapotranspiration processes, for both the surface and subsurface domains, into one complete modeling framework.

The coupling of HGS with the simplified ABL model was the first step in the development of the coupled atmospheric, lands surface, and subsurface models. The lessons learned coupling HGS to the ABL model directly guided the the framework to couple HGS to a three-dimensional atmospheric model.

The next step after the HGS-ABL model was to couple HGS to the Weather Research and Forecasting (WRF) Model, a three-dimensional nonhydrostatic mesoscale atmospheric model. HGS replaces the land surface components of WRF by providing the actual evapotranspiration (AET) and soil water saturation from the porous media to the atmosphere. In exchange, WRF provides HGS with the potential evapotranspiration (PET) and precipitation fluxes. The two-way coupling technique uniquely accepts independent model meshing and projections and links domains based on their geographic coordinates (i.e., latitude and longitude).

This study then demonstrates the HGS-WRF model over the California Basin to investigate the interactions of the subsurface, surface, and atmosphere in a fully three-dimensional environment. Furthermore, this work is the first of its kind to:

- Develop the first three-dimensional geological model for California.
- Implement the first fully-integrated three-dimensional model of the California Basin.
- Incorporate the subsurface, surface, and atmosphere into one complete framework over a large scale basin model.
- Include deep groundwater flow within a coupled atmospheric model.

The framework presented in this thesis is currently the most complete water resource model, because the deep subsurface, surface and atmosphere are included into one coupled platform. The implementation of HGS-WRF captures the dynamic patterns of weather and climate within the California Basin. Furthermore, the 200 day simulation results shown in this work are the beginning stages of the California Basin Model.

However, the California Basin Model does not include several important processes (e.g. hydraulic control structures, irrigation, and winter processes), which limits the skill of the numerical simulations. Even with these drawbacks, the California Basin Model successfully demonstrated the potential of HGS-WRF and further research is required to develop a more complete coupled model. As this research progresses, the simulation results will directly inform water managers about the sustainable yield of water resources and will help policymakers to develop science-based plans to better manage their resources. Moreover, this framework of research will help project the potential impact of water policy decisions on water resources, local economies, and communities.

5.1 Future Work

Heat transport was not included in the current version of the HGS-WRF coupling. The water balance was the primary focus for the first version of HGS-WRF, and it was desired to minimize the number of independent variables in the coupling scheme to reduce computational demand. In future releases, it is planned to incorporate heat transport processes as an option in the coupled HGS-WRF model. From experience with the HGS-ABL model, the depth of the subsurface may play a critical role for temperature regulations, especially during prolonged drought conditions.

The current HGS-WRF model does not include snow processes (a major water balance component in the Sierra Nevada Mountains), and the inclusion of sediment freeze-thaw processes would be the next logical advancement to the coupled model. Currently, HGS-WRF treats all water as liquid precipitation, which may artificially increase stream flow during the winter months and decrease streamflow during the summer. HydroGeoSphere already has snowmelt and soil freeze-thaw built into the model, and the WRF simulation would provide the correct fluxes to accurately simulate winter processes.

Ultimately, it is planned to continue the development of the California Basin model by incorporating a significantly more advanced geological model that includes detailed borehole data. The presented version of the California model uses averaged water use data. Other issues to explore include testing an unstructured HGS mesh that can better represent land cover and topographic details, refinement of the HGS-WRF time-stepping controls, inclusion of engineered hydraulic features, and model calibration to available field data.

References

Abdul, A. S. (1985), Experimental and Numerical studies of the effect of the capillary fringe on streamflow generation, *Ph.D. Thesis, University of Waterloo, Waterloo, Ontario, Canada*, p. 210.

Aquanty, Inc. (2015), HydroGeoSphere. A three-dimensional numerical model describing fully-integrated subsurface and surface flow and solute transport, User Guide, *Aquanty Inc.*, pp. 1–465.

Bartholomeus, R. P., J.-P. M. Witte, P. M. van Bodegom, J. C. van Dam, and R. Aerts (2011), Climate change threatens endangered plant species by stronger and interacting water-related stresses, *Journal of Geophysical Research*, *116*(G4), G04,023.

Berrisford, P., D. Dee, P. Poli, R. Brugge, K. Fielding, M. Fuentes, P. Kållberg, S. Kobayashi, S. Uppala, and A. Simmons (2011), The era-interim archive version 2.0.

Bolger, B. L., Y.-J. Park, A. J. Unger, and E. A. Sudicky (2011), Simulating the pre-development hydrologic conditions in the San Joaquin Valley, California, *Journal of Hydrology*, *411*(3), 322–330.

Brookfield, A. E., E. A. Sudicky, Y. J. Park, and B. Conant (2009), Thermal transport modelling in a fully integrated surface/subsurface framework, *Hydrological Processes*, *23*(15), 2150–2164.

Brooks, R. H., and A. T. Corey (1964), Hydraulic properties of porous media, *Hydrology Papers, Colorado State University, March*.

California Department of Water Resources (2016), California Irrigation management Information System.

Carlson Mazur, M. L., M. J. Wiley, and D. A. Wilcox (2014), Estimating evapotranspiration and groundwater flow from water-table fluctuations for a general wetland scenario, *Ecohydrology*, *7*(2), 378–390.

Chen, F., and J. Dudhia (2001), Coupling an Advanced Land Surface-Hydrology Model with the Penn State-NCAR MM5 Modeling System. Part I: Model Implementation and Sensitivity, *Monthly Weather Review*, *129*(4), 569–585.

Chen, J. (2015), Impact of Climate Change on Canadian Water Resources: A Continental-Scale Hydrologic Modelling Study Using Multiple RCM Projections, *Ph.D. Thesis, University of Waterloo, Waterloo, Ontario, Canada.*

Chen, J., J. S. Famiglietti, B. R. Scanlon, and M. Rodell (2016), Groundwater storage changes: present status from GRACE observations, in *Remote Sensing and Water Resources*, pp. 207–227, Springer.

Climate Commons (2015), California Landscape Conservation Cooperative.

Davison, J. H., H.-T. Hwang, E. A. Sudicky, and J. C. Lin (2015), Coupled atmospheric, land surface, and subsurface modeling: Exploring water and energy feedbacks in three-dimensions, *Advances in Water Resources*, *86*, 73–85.

Easterling, D. R., G. A. Meehl, C. Parmesan, S. A. Changnon, T. R. Karl, and L. O. Mearns (2000), Climate extremes: observations, modeling, and impacts, *Science*, *289*(5487), 2068–2074.

Famiglietti, J. S., M. Lo, S. L. Ho, J. Bethune, K. J. Anderson, T. H. Syed, S. C. Swenson, C. R. de Linage, and M. Rodell (2011), Satellites measure recent rates of groundwater depletion in California's Central Valley, *Geophysical Research Letters*, *38*(3).

Farr, T. G., C. Jones, and Z. Liu (2015), *Progress report: subsidence in the Central Valley, California.*

Faunt, C. (2009), Groundwater Availability of the Central Valley Aquifer, California: U.S. Geological Survey Professional Paper 1766, p. 225.

Flint, L. E., A. L. Flint, J. H. Thorne, and R. Boynton (2013), Fine-scale hydrologic modeling for regional landscape applications: the California Basin Characterization Model development and performance, *Ecological Processes*, *2*(1), 1–21.

Garratt, J. R. (1994), *The Atmospheric Boundary Layer*, Cambridge University Press.

Gilbert, J., and R. Maxwell (2014), Resolving Spatiotemporal Climate Change Impacts on San Joaquin Basin Hydrology, presented at 2014 Fall Meeting, AGU, San Francisco, Calif., 15-19 Dec.

Gilbert, J., R. Maxwell, D. Gochis, S. Maples, and K. Markovich (2015), Using Coupled Subsurface-Atmospheric Simulations to Investigate the Impact of Irrigation on Atmospheric Response in the San Joaquin River Basin, California, presented at 2015 Fall Meeting, AGU, San Francisco, Calif., 14-18 Dec.

Gleick, P. H. (1998), Water in crisis: paths to sustainable water use, *Ecological applications*, *8*(3), 571–579.

Gochis, D., and F. Chen (2003), Hydrological enhancements to the community Noah land surface model., *NCAR Technical Note NCAR/TN-454+STR*.

Gochis, D. J., W. Yu, and D. N. Yates (2013), The NCAR WRF-Hydro Technical Description and User's Guide, version 1.0., *NCAR Technical Document*, p. 120.

Graf, T., and R. Therrien (2007), Coupled thermohaline groundwater flow and single-species reactive solute transport in fractured porous media, *Advances in water resources*, *30*(4), 742–771.

Gusev, Y. M., and O. N. Nasonova (1998), The land surface parameterization scheme SWAP: Description and partial validation, *Global and Planetary Change*, *19*(1), 63–86.

Howitt, R., J. Medellín-Azuara, D. MacEwan, J. Lund, and D. Sumner (2014), Economic analysis of the 2014 drought for California agriculture, *Center for Watershed Sciences, University of California, Davis.*

Hwang, H.-T., Y.-J. Park, E. Sudicky, and P. Forsyth (2014), A parallel computational framework to solve flow and transport in integrated surface–subsurface hydrologic systems, *Environmental Modelling & Software*, *61*, 39–58.

Jarvis, P. G. (1976), The Interpretation of the Variations in Leaf Water Potential and Stomatal Conductance Found in Canopies in the Field, *Philosophical Transactions of the Royal Society of London. B, Biological Sciences*, *273*(927), 593–610.

Jones, J., E. Sudicky, and R. McLaren (2008), Application of a fully-integrated surface-subsurface flow model at the watershed-scale: A case study, *Water Resources Research*, *44*(3).

Karl, T. R., R. W. Knight, and N. Plummer (1995), Trends in high-frequency climate variability in the twentieth century, *Nature*, *377*, 217–220.

Kristensen, K. J., and S. E. Jensen (1975), A model for estimating actual evapotranspiration from potential evapotranspiration, *Nordic Hydrology*, *6*(3), 170–188.

Kundzewicz, Z. W., L. J. Mata, N. Arnell, P. Doll, P. Kabat, B. Jimenez, K. Miller, T. Oki, S. Zekai, I. Shiklomanov, et al. (2007), *Freshwater resources and their management. Climate Change 2007: Impacts, Adaptation and Vulnerability. Contribution of Working Group II to the Fourth Assessment Report of the Intergovernmental Panel on Climate Change*, Cambridge University Press.

Laske, G., and G. Masters (1997), A Global Digital Map of Sediment Thickness, *EOS Trans. AGU, 78, F483.*

Liu, S., L. Lu, D. Mao, and L. Jia (2007), Evaluating parameterizations of aerodynamic resistance to heat transfer using field measurements, *Hydrology and Earth System Sciences Discussions*, *11*(2), 769–783.

Long, M. T. (2016), Minnesota Watersheds.

Manabe, S., J. Smagorinsky, and R. F. Strickler (1965), Simulated climatology of a general circulation model with a hydrologic cycle 1, *Monthly Weather Review*, *93*(12), 769–798.

Mann, M. E., and P. H. Gleick (2015), Climate change and California drought in the 21st century, *Proceedings of the National Academy of Sciences*, *112*(13), 3858–3859.

Maxwell, R. M., and S. J. Kollet (2008), Interdependence of groundwater dynamics and land-energy feedbacks under climate change, *Nature Geoscience*, *1*(10), 665–669.

Maxwell, R. M., F. K. Chow, and S. J. Kollet (2007), The groundwater–land-surface–atmosphere connection: Soil moisture effects on the atmospheric boundary layer in fully-coupled simulations, *Advances in Water Resources*, *30*(12), 2447–2466.

Maxwell, R. M., J. K. Lundquist, J. D. Mirocha, S. G. Smith, C. S. Woodward, and A. F. B. Tompson (2011), Development of a Coupled Groundwater-Atmosphere Model, *Monthly Weather Review*, *139*(1), 96–116.

McCumber, M. C., and R. A. Pielke (1981), Simulation of the effects of surface fluxes of heat and moisture in a mesoscale numerical model 1. Soil layer, *J. Geophys. Res*, *86*(C10), 9929–9938.

Mengelkamp, H. T., K. Warrach, and E. Raschke (1999), SEWAB–a parameterization of the surface energy and water balance for atmospheric and hydrologic models, *Advances in water Resources*, *23*(2), 165–175.

Niu, G.-Y., C. Paniconi, P. A. Troch, R. L. Scott, M. Durcik, X. Zeng, T. Huxman, and D. C. Goodrich (2014), An integrated modelling framework of catchment-scale ecohydrological processes: 1. Model description and tests over an energy-limited watershed, *Ecohydrology*, *7*(2), 427–439.

Noilhan, J., and S. Planton (1989), A simple parameterization of land surface processes for meteorological models, *Monthly Weather Review*, *117*(3), 536–549.

Oki, T., and S. Kanae (2006), Global hydrological cycles and world water resources, *Science*, *313*(5790), 1068–1072.

Park, Y.-J., E. A. Sudicky, S. Panday, and G. Matanga (2009), Implicit subtime stepping for solving nonlinear flow equations in an integrated surface–subsurface system, *Vadose Zone Journal*, *8*(4), 825–836.

Quinn, P., K. Beven, and A. Culf (1995), The introduction of macroscale hydrological complexity into land surface-atmosphere transfer models and the effect on planetary boundary layer development, *Journal of Hydrology*, *166*(3), 421–444.

Runyan, C., and C. Welty (2010), *Use of the White Method to Estimate Evapotranspiration along an Urban Riparian Corridor, CUERE Technical Report 2010/001*, UMBC, Center for Urban Environmental Research and Education.

Scanlon, B. R., C. C. Faunt, L. Longuevergne, R. C. Reedy, W. M. Alley, V. L. McGuire, and P. B. McMahon (2012), Groundwater depletion and sustainability of irrigation in the US High Plains and Central Valley, *Proceedings of the National Academy of Sciences*, *109*(24), 9320–9325.

Seaber, P. R., F. P. Kapinos, and G. L. Knapp (1987), Hydrologic Unit Maps: U.S. Geological Survey Professional Paper 2294, p. 63.

Sebestyen, S. D., E. W. Boyer, and J. B. Shanley (2009), Responses of stream nitrate and DOC loadings to hydrological forcing and climate change in an upland forest of the northeastern United States, *Journal of Geophysical Research*, *114*(G2), G02,002.

Skamarock, W., J. Klemp, J. Dudhia, D. Gill, D. Barker, M. Duda, X. Huang, W. Wang, and J. Powers (2008), A Description of the Advanced Research WRF Version 3, *NCAR TECHNICAL NOTE*, *NCAR/TN475+STR*.

Skoulikaris, C., and J. Ganoulis (2011), Assessing Climate Change Impacts at River Basin Scale by Integrating Global Circulation Models with Regional Hydrological Simulations, *European Water*, *34*, 55–62.

Soil Survey Staff (2015), Natural Resources Conservation Service, United States Department of Agriculture. Web Soil Survey.

Stull, R. B. (1988), *An introduction to boundary layer meteorology*, vol. 13, Springer.

Sudicky, E. A., J. P. Jones, Y.-J. Park, A. E. Brookfield, and D. Colautti (2008), Simulating complex flow and transport dynamics in an integrated surface-subsurface modeling framework, *Geosciences Journal*, *12*(2), 107–122.

Therrien, R., and E. Sudicky (1996), Three-dimensional analysis of variably-saturated flow and solute transport in discretely-fractured porous media, *Journal of Contaminant Hydrology*, *23*(1), 1–44.

United States Army Corps of Engineers (2016), National Inventory of Dams.

United States Geological Survey (2016), USGS Current Conditions for the Nation.

U.S. Geological Survey (2015a), California Water Use, 2010s.

U.S. Geological Survey (2015b), HYDRO1k.

Van Genuchten, M. T. (1980), A closed-form equation for predicting the hydraulic conductivity of unsaturated soils, *Soil Science Society of America Journal*, *44*(5), 892–898.

Vano, J. A., B. Udall, D. R. Cayan, J. T. Overpeck, L. D. Brekke, T. Das, H. C. Hartmann, H. G. Hidalgo, M. Hoerling, G. J. McCabe, et al. (2014), Understanding uncertainties in future Colorado River streamflow, *Bulletin of the American Meteorological Society*, *95*(1), 59–78.

Verseghy, D. L. (2000), The Canadian land surface scheme (CLASS): Its history and future, *Atmosphere-Ocean*, *38*(1), 1–13.

Walcek, C. J. (1994), Cloud cover and its relationship to relative humidity during a springtime midlatitude cyclone, *Monthly weather review*, *122*(6), 1021–1035.

Wallace, J. M., and P. V. Hobbs (2006), *Atmospheric science: an introductory survey*, vol. 92, Academic press.

White, W. N. (1932), A method of estimating ground-water supplies based on discharge by plants and evaporation from soil: Results of investigation in Escalante Valley, Utah., *Water-Supply Paper*, *659-A*.